2007

Multiscale modeling of segregation in granular flows

Jin Sun
Iowa State University

Recommended Citation

Sun, Jin, "Multiscale modeling of segregation in granular flows" (2007). *Retrospective Theses and Dissertations*. 15499.
http://lib.dr.iastate.edu/rtd/15499

Multiscale modeling of segregation in granular flows

by

Jin Sun

A dissertation submitted to the graduate faculty

in partial fulfillment of the requirements for the degree of

DOCTOR OF PHILOSOPHY

Major: Mechanical Engineering

Program of Study Committee:
Francine Battaglia, Co-major Professor
Shankar Subramaniam, Co-major professor
Kenneth Bryden
Rodney O. Fox
Theodore J. Heindel
James C. Hill

Iowa State University
Ames, Iowa
2007

ProQuest Information and Learning Company
300 North Zeeb Road
P.O. Box 1346
Ann Arbor, MI 48106-1346

DEDICATION

To my parents and my sisters.

TABLE OF CONTENTS

LIST OF TABLES

LIST OF FIGURES

ACKNOWLEDGEMENTS

I would like to express my appreciations to my committee members and those who helped me with various aspects of conducting research and teaching during my Ph. D. study. It has been a pleasure and privilege working with people with high professionalism and integrity. I own my deepest gratitude to my advisors, Dr. Francine Battaglia and Dr. Shankar Subramaniam, for their guidance and support. They have been teaching me to investigate interesting engineering problems using rigorous scientific approaches. Their insights and encouragements have often inspired me to pursue higher goals in my career and life. I would like to thank Dr. Rodney O. Fox for his helpful discussion of research ideas and for his interest in my professional development. I am also grateful to Dr. James C. Hill for giving me a new perspective in transport phenomena and for mentoring me on preparing for a faculty career. I would also like to thank my officemates for an intellectually stimulating working environment.

My family has been a source of inspiration and support over these many years. I thank them for allowing and encouraging me to pursue my dreams.

ABSTRACT

Modeling and simulation of segregation phenomena in granular flows are investigated. Computational models at different scales ranging from particle level (microscale) to continuum level (macroscale) are employed in order to determine the important microscale physics relevant to macroscale modeling. The capability of a multi-fluid model to capture segregation caused by density difference is demonstrated by simulating grain-chaff biomass flows in a laboratory-scale air column and in a combine harvester. The multi-fluid model treats gas and solid phases as interpenetrating continua in an Eulerian frame. This model is further improved by incorporating particle rotation using kinetic theory for rapid granular flow of slightly frictional spheres. A simplified model is implemented without changing the current kinetic theory framework by introducing an effective coefficient of restitution to account for additional energy dissipation due to frictional collisions. The accuracy of predicting segregation rate in a gas-fluidized bed is improved by the implementation. This result indicates that particle rotation is important microscopic physics to be incorporated into the hydrodynamic model. Segregation of a large particle in a dense granular bed of small particles under vertical vibration is studied using molecular dynamics simulations. Wall friction is identified as a necessary condition for the segregation. Large-scale force networks bearing larger-than-average forces are found with the presence of wall friction. The role of force networks in assisting rising of the large particle is analyzed. Single-point force distribution and two-point spatial force correlation are computed. The results show the heterogeneity of forces and a short-range correlation. The short correlation length implies that even dense granular flows may admit local constitutive relations. A modified minimum spanning tree (MST) algorithm is developed to asymptotically recover the force statistics in the force networks. This algorithm provides a possible route to constructing a continuum model with microstructural information supplied from it. Microstructures in gas fluidized beds are also analyzed using a hybrid method, which couples the discrete element method (DEM) for particle dynamics with the averaged two-fluid (TF) equations for the gas phase. Multi-particle contacts are found in defluidized regions away from bubbles in fluidized beds. The multi-particle contacts invalidate the binary-collision assumption made in the kinetic theory of granular flows for the defluidized regions. Large ratios of contact forces to drag forces are found in the same regions, which confirms the relative importance of contact forces in determining particle dynamics in the defluidized regions.

CHAPTER 1. INTRODUCTION

1.1 Background

A granular material is a collection of discrete solid particles, which interact with dissipative collisions and for which the thermal energy is small compared to any energy scale in the problem. Granular flows are referred here as both dry granular flows and gas-solid flows investigated in this dissertation. Dry granular flow means that the interstitial fluid either does not exist or can be ignored in describing the flow behavior when particles alone will play the greatest role in momentum transport within the material (Campbell, 1990).

Granular flows are abundant in nature, such as snow and avalanches, and widely used in many operations in chemical, petroleum, pharmaceutical, agricultural, biochemical, food, electronic, mining and power-generation industries. For example, Chevron refinery in Pascagoula, MS uses a fluidized bed catalytic cracker operating around the clock, 365 days per year to process 325,000 barrels (13.6 million gallons) of crude oil per day (Chevron, 2005). At 60 dollars a barrel, that is about 7 billion dollars per year.

Granular flows are, however, poorly understood despite the widespread importance for industrial applications. A study indicates that the commercial and large-scale solids-processing plants have an operating reliability of 63 percent, compared to 84 percent for large-scale plants using only liquids and gases (Plasynski et al., 1992). One of the most puzzling phenomena in granular flows is segregation. Segregation is a process in which a homogeneous granular material composed of various constituents of different properties becomes spatially nonuniform as a result of relative movement within the material (Enstad, 2001; Rosato et al., 2002). Its occurrence is rather ubiquitous and of universal concern to the above-mentioned industries. For example, in a fluidized bed coal gasifier, segregation of coal and hot circulating solids should be avoided to prevent the occurrence of non-uniform volatile distribution, which leads to low gasification efficiency. Knowledge of the degree and rate of this kind of segregation phenomena is of tremendous practical importance (Rosato et al., 1991). In most industrial applications, segregation poses a formidable impediment to the general requisite of creating and maintaining a well-mixed mixture. Failure to achieve this homogeneous mixture throughout its processing history can lead to unfavorable economic consequences. In some industrial applications, the tendency for segregation is utilized, such as removing chaff from grain in a combine.

In addition to the practical importance, segregation in granular flows is also fundamentally challenging as an outstanding problem in granular physics. It has recently gained more attention in fundamental experimental (Möbius et al., 2001; Breu et al., 2003; Nahmad-Molinari et al., 2003; Huerta and Ruiz-Suárez, 2004b; Möbius et al., 2004) and theoretical studies (Rosato et al., 1987; Shishodia and Wassgren, 2001; Hong et al., 2001; Trujillo et al., 2003). Efforts have been made in these studies to explain segregation from the non-equilibrium, dissipative nature of granular material and to establish hydrodynamics models for segregation behavior. However, the mechanisms of segregation have not been fully understood through these extensive studies in both engineering and physics communities. Moreover, first-principle modeling of segregation is either unrealistic or impossible (Ottino and Khakhar, 2000). For example, Goldschmidt et al. (2001b) and Sun and Battaglia (2006) found that a multi-fluid continuum model predict much higher segregation rates than experimental results in a dense gas fluidized bed. Current engineering approaches attack segregation problems on an ad hoc basis and often result in unsatisfying predictions.

The importance of understanding segregation in granular flows and the inability to model the phenomena accurately motivate the current research to enhance the fundamental understanding of the mechanisms of segregation, and to improve and develop continuum models to predict segregation in a more accurate way. The continuum models can be then used in computational fluid dynamics (CFD) tools to better capture segregation characteristics and to assist in design and optimization of the processes involving segregation.

1.2 Research objectives and approaches

The research herein is generally aimed to address questions in the following aspects: "What are the fundamental segregation mechanisms? How can these mechanisms be incorporated into continuum models? How successful will these models address engineering problems?"

Segregation is often governed by a combination of mechanisms, which themselves depend on flow regimes and particle properties. For example, particle properties which influence segregation are particle sizes and size distribution, density, shape, morphology, contact friction, elasticity, brittleness, chemical affinities, ability to absorb moisture and magnetic properties (Enstad, 2001; Rosato et al., 2002). Segregation is further complicated by the means in which energy is imparted into the granular material causing it to flow. According to practical interests and scientific simplifications, this research focuses on segregation of spherical particles of different size and/or density excited by vibration or gas flows. The particle volume fraction is relatively large and the particle Stokes number is usually much larger than unity. Studies will show what mechanisms drive the segregation under both fluidized and partial fluidized conditions. The driving forces will be quantified and modeled at a continuum level. The engineering applications focus on using the continuum models to improve predictions of segregation in gas fluidized beds and biomass flows in a combine.

Due to the complexity of the segregation in granular flows and the discrete nature of solid particles, a multiscale modeling strategy is proposed, as presented in figure 1.1. In this strategy, at the macroscale level, a multi-fluid model is used to simulate large scale engineering granular flows, in which both fluid and solid particles are treated as continua and their velocities are locally averaged (Jackson, 2000). At the microscale level, molecular dynamics (MD) is employed to simulate dry granular flows. MD can simulate individual particle movements and the contact forces between particles. The microscale information will give physical insights into the collective particle behaviors, such as flow regimes and microstructure formation, and guide the continuum model development. By obtaining macroscale continuum fields from microscale particle information statistically, the microscale simulations can also be used to validate the closure laws in solid phase rheology and solid-solid phase momentum transfer. Combining

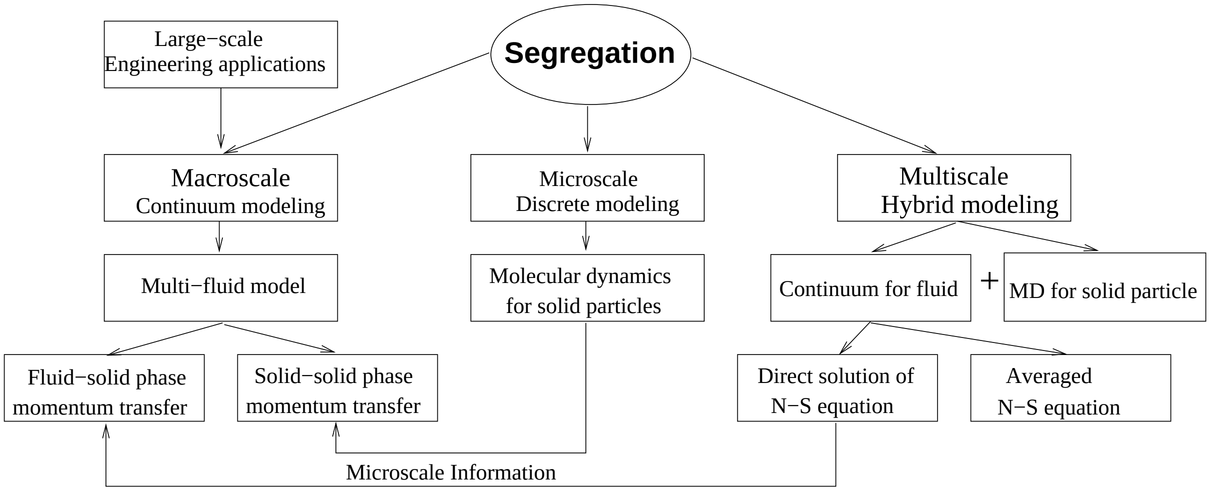

Figure 1.1 Multiscale modeling strategy for simulation of segregation in granular flows.

continuum models for fluid and MD for solid particles, a hybrid model can be formed to study the solid particles behavior under the influence of a fluid. It should be noted that in this research, averaged Navier-Stokes equations for the fluid are used. Fluid-solid interaction is modeled by an empirical correlation for gas-solid drag. Therefore, no instantaneous information about the interaction between fluid and solid can be provided and the simulation accuracy depends on the empirical correlation. The main goal of this research is to investigate the solid particle behavior from the microscale and incorporate more relevant modeling information to the continuum models at the macroscale.

1.3 Outline of the dissertation

In chapter 2, a general survey of modeling methods of granular flows and segregation is presented including macroscale models, microscale models and hybrid methods. In macroscale models, kinetic theory for granular flows (KTGF) is emphasized, while soft-sphere MD or discrete element method (DEM) is stressed for the microscale models since these two are the main tools in this research.

Chapter 3 summarizes the hydrodynamics theory for a multi-fluid model and numerical formulation used in the Multiphase Flow with Interphase eXchanges (MFIX) code, which is extensively used in the macroscale simulation work. The basic procedure of using KTGF to derive constitutive equations of solid phases for the multi-fluid model is also presented.

Application of CFD modeling for biomass flows in a combine is shown in chapter 4 by simulations for grain fluidization and simulations for grain and chaff separation.

Chapter 5 presents an implementation of a particle rotation model using KTGF to the multi-fluid model and the improvements of the accuracy of predicting segregation rates in a bubbling fluidized bed using the improved multi-fluid model.

Chapter 6 studies the rise dynamics of a large particle in a granular bed under vertical vibration using molecular dynamics simulations. Force networks in the granular bed are also investigated. The distribution and the two-point spatial correlation of normal contact are studied. The structural properties of the force network are analyzed using a graph-theoretic approach, which is a modification of a minimum spanning tree (MST) constructed on the particles in physical space.

In chapter 7, simulations of gas-solid fluidized beds are carried out using a hybrid simulation method, which couples the DEM for particle dynamics with the averaged two-fluid (TF) equations for the gas phase. The coupling between the two phases is modeled using an interphase momentum transfer term. The results of the hybrid TF-DEM simulations are compared to experimental data and two-fluid model simulations. The microstructures in fluidized beds are analyzed and the implications to KTGF are discussed. Various forms of the interphase momentum transfer model are examined.

Chapter 8 summaries the main conclusions from the research work in this dissertation. Possible extensions to the dissertation work are discussed from the microscale and macroscale modeling perspectives. An outlook of deriving continuum models that can predict segregation behavior in a broad range of granular flow regimes is given.

It is worth noting that different notations are used in different chapters. Symbols are either listed in a nomenclature list for an individual chapter or explained in context. **Bold type** or over-vector $\vec{()}$ are used for vectors. Sans Serif type or double over-lines $\overline{\overline{()}}$ are used for tensors.

CHAPTER 2. LITERATURE REVIEW

This chapter presents a survey on modeling of segregation phenomena in granular flows. The theories and models for general granular flow behaviors are also reviewed as a basis for understanding the particular segregation phenomena.

2.1 Macroscale (continuum) modeling of granular flows and segregation

Granular materials can behave like solids, liquids or gases depending on material properties and external forcing conditions (Jaeger et al., 1996). Simply, in the quasi-static regime, the external force is constantly supported by the force chains within the granular material. In the transitional regime, as the solid concentration decreases, or the non-dimensional strain rate increases, the internal force chains become intermittent, being continuously destroyed and regenerated by relative particle motion. As this trend continues, the solid concentration further reduces and the non-dimensional strain rate increases, particle motion becomes more agitated, and the external load is supported by the impact momentum transfer generated when the particles collide with the boundary. This complex behavior makes it very difficult to formulate a comprehensive macroscale theory of granular flow, which can describe all the flow regimes. Approaches to formulate a macroscale model can use the following schemes:

- Classical continuum theories
- Statistical mechanics (e.g., kinetic theory for granular flows)
- Micromechanical approach
- Phenomenological models based on experiments or computer simulations

Table 2.1 Comparison of particle properties between granular flows and molecular gases.

Molecular gases particles	Granular flow particles
diameter scale 10^{-10} m	diameter scale $> 10^{-6}$ m
elastic	inelastic
identical	with size distribution
smooth	rough
spherical	non-spherical

Kinetic theory for granular flows (KTGF) has been reasonably successful in describing the "rapid shear" fluidized regime. The development of KTGF, especially the extension to binary mixtures will be reviewed in detail. However, rigorously extending KTGF to moderately dense and dense granular flow has met great difficulties. Alternative models for transitional regime and slow dense granular flows will be reviewed following KTGF.

2.1.1 Kinetic theory for granular flows

Solid particles in the rapid shear regime interact by nearly instantaneous collisions (compared with the mean free time) in a way that is reminiscent of the classical picture of a molecular gas. In this sense, the rapid granular flow is also known as a "granular gas". Although rapid granular flows resemble molecular gases, there are important differences between them, which determine the intrinsic behavior of rapid granular flows. A comparison between granular material particles and molecular gas particles is shown in table 2.1. The important difference is the inelasticity of granular particles, which causes energy losses from collisions of granular particles and leads to the dissipative dynamics.

The physical similarity between rapid shear granular flows and the kinetic theory view of gases has led to research on extending kinetic theory for gases (Chapman and Cowling, 1970) to granular flows. The idea is to derive a set of continuum equations entirely from microscopic models of dissipative individual particle interactions. All of the models assume that particles interact by instantaneous collisions, which implies that only binary interactions need to be considered. Furthermore, molecular chaos is generally assumed, implying that the random motion of even closely neighboring particles are independently distributed.

The most primitive KTGF was derived for identical, smooth, nearly elastic, spherical particles and the form of the velocity distribution function was assumed to be Maxwellian instead of attempting to solve the Boltzmann equation to find the distribution function. The first calculation of this type was done by Savage and Jeffrey (1981), who derived the collisional portion of the stress tensor based on the assumption that the random particle velocities followed a Maxwellian distribution. The theory did not include the granular energy equation. Jenkins and Savage (1983) solved the energy balance for granular temperature but neglected the streaming (kinetic) contribution to the stress tensor, i.e., when the particles are not in collision. Later Lun et al. (1984) first attempted to compute the streaming contribution to the stress tensor and used a perturbation to the Maxwellian velocity distribution. An accurate prediction of streaming stressed was obtained.

The generalization of the KTGF provides a means to address particles with property differences, particle friction, and high inelasticity. The generalization has been done in the following theoretical aspects:

- Non-Maxwellian distribution function by perturbation to the Maxwellian distribution function.
- Homogeneous cooling state as the zeroth order in Chapman-Enskog expansion (Chapman and Cowling, 1970).
- Burnett order Chapman-Enskog expansion (one order higher than Navier-Stokes order).
- Revised Enskog theory (RET) to evaluate radial distribution function for dense flows to correct the inconsistencies with irreversible thermodynamics caused by the standard Enskog theory (SET).
- Ring level kinetic theory to account for the particle velocities correlation in dense flows.

Some of these theoretical aspects will be discussed as follows. KTGF for particles with shapes other than spheres has not been addressed in literature although kinetic theory for rigid ellipsoid have been developed for polyatomic liquids (Theodosopulu and Dahler, 1974).

The effort in extending KTGF to describe granular mixtures of particles with different properties was first done by Jenkins and Mancini (1987) for a planar flow of a dense, binary mixture of smooth, nearly elastic, circular disks and spheres assuming a Maxwellian velocity distribution. Later Jenkins and Mancini (1989) developed a more exact theory using RET involving perturbations to the Maxwellian velocity distribution. They assumed that the energy dissipation in the collision was sufficiently small, such that the deviation of the temperature of each component from the mixture granular temperature is very small. Thus, in the application of their model, they assumed energy equipartition in each component. Based on the work of Jenkins and Mancini (1989), Arnarson and Willits (1998) and Willits and Arnarson (1999) extended KTGF of a binary mixture using the Chapman-Enskog procedure. They solved the Ensgok kinetic equation near the steady-state equilibrium, assuming energy equipartition and almost equal particle mass, to calculate the transport coefficients. They found that the shear viscosity was three times higher than that obtained using only a Maxwellian velocity distribution. Alam et al. (2002) generalized the model of Willits and Arnarson (1999) to a mixture of particles having different mass and size. However, their model was limited to energy equipartition. Zamankhan (1995) solved the Enskog kinetic equation using the Grad method (Grad, 1949) and assumed that the particles fluctuate with the same energy; he concluded that energy non-equipartition must be included in mixtures with different properties. Garzó and Dufty (1999a) showed theoretically that energy equipartition was violated for inelastic collisions of particles of different mechanical properties, and was experimentally confirmed by Wildman and Parkar (2002) and Feitosa and Menon (2002). Lu et al. (2001) developed a model for two-size particles with different granular temperatures; however, the approach they used was phenomenological and inappropriate, thus making their model limited to only the energy equipartition case. Recently Garzó and Dufty (2002) solved the Boltzmann equation for systems away from equilibrium and analyzed the shear viscosity coefficient (Montanero and Garzó, 2003), mass and heat fluxes (Garzó et al., 2006). Their model not only captures the energy non-equipartition, but also is formally correct for a broader range of restitution coefficients. However, their model is restricted to dilute systems. Later on, Garzó and Mon-

Table 2.2 Summary of KTGF models for granular mixtures (EP is abbreviation for equipartition and NEP is for non-equipartition).

References	Single particle velocity distribution	Energy distribution	Radial distribution function	Mixture or phase representation
Jenkins and Mancini (1987)	Maxwellian	NEP	SET	Mixture
Jenkins and Mancini (1989)	Non-Maxwellian	EP	RET	Mixture
Zamankhan (1995)	Non-Maxwellian	EP	RET	Mixture
Arnarson and Willits (1998)	Non-Maxwellian	EP	RET	Mixture
Willits and Arnarson (1999)	Non-Maxwellian	EP	RET	Mixture
Lu et al. (2001)	Maxwellian	NEP	SET	Phase
Garzó and Dufty (2002)	Non-Maxwellian	NEP	SET	Mixture
Garzó and Montanero (2003)	Non-Maxwellian	NEP	RET	Mixture
Rahaman et al. (2003)	Maxwellian	NEP	SET	Mixture
Iddir and Arastoopour (2005)	Non-Maxwellian	NEP	SET	Phase

tanero (2003) extended the same method to moderately dense binary mixture using RET, for which the flow condition was limited to uniform shear flow. Rahaman et al. (2003) also derived a non-equipartition kinetic theory for binary mixtures using a Maxwellian velocity distribution. Most recently, Iddir and Arastoopour (2005) extended KTGF to a multi-type mixture assuming a non-Maxwellian velocity distribution and energy non-equipartition. Each group type is represented by a phase with an average velocity and a granular temperature, unlike previous work, where the fluctuations of the flow variables are about the mixture average. The Enskog kinetic equation for each particulate phase was solved using the Chapman-Enskog procedure. However, in their approach, the deviation from the Maxwellian velocity distribution is in each individual particulate phase and Maxwellian velocity distribution was assumed at the interface and RET is not used. A complete KTGF for dense binary mixtures, which considers non-Maxwellian distribution and energy non-equipartition and employs RET, has not yet available for general flow conditions. A summary of these KTGF models is listed in table 2.2.

The KTGF for a mixture has direct relevance to modeling segregation phenomena. For example, from KTGF, the momentum balance is derived in the following general form

$$\rho_i \frac{\mathrm{d}\mathbf{v}_i}{\mathrm{d}t} = \rho_i \mathbf{F}_i - \rho_i \boldsymbol{\nabla} \cdot \mathsf{P}_i + \boldsymbol{\phi}_i, \tag{2.1}$$

for species or phase i, where $\boldsymbol{\phi}_i$ is the momentum source due to collisions between unlike particles. Each of the previous reviewed KTGF models gives different specific expressions for the constitutive equations. From equation 2.1, a diffusion velocity equation can be derived. For example, using Jenkins and Mancini (1987) theory, a simplified diffusion velocity equation for binary mixture is derived as:

$$\mathbf{v}_1 - \mathbf{v}_2 = -\frac{n^2}{n_1 n_2} D_{12} \mathbf{d}_1, \tag{2.2}$$

where $n = n_1 + n_2$ is the number density of the mixture, D_{12} is the coefficient of ordinary diffusion and $\mathbf{d_1}$ is the diffusion driving force. A few researchers have been using this approach to analyze segregation phenomena in simple granular flows. Hsiau and Hunt (1996) used the theory of Jenkins and Mancini (1989) to investigate the driving force for segregation. Khakhar et al. (1999) compared model predictions based on the Jenkins and Mancini (1989) theory with discrete particle simulations for chute flows. Jenkins and Yoon (2002) studied the segregation criteria for a binary mixture with large particles being dilute under gravity. Arnarson and Jenkins (2002) derived a simplified constitutive theory for a steady, fully developed, rectilinear flow and studied the segregation in this flow with a corrected expression for the ordinary diffusion coefficient. However, most of these applications are limited to particles of slight difference in diameter and mass and for very simple flows. Furthermore the newly derived KTGF by Iddir and Arastoopour (2005) has not been tested in their capability of predicting segregation.

There are also developments to derive KTGF for rough particles. Jenkins and Richman (1985) studied identical, rough inelastic, circular disks. Lun and Savage (1987) developed a kinetic theory for a system of inelastic, rough spherical particles to study the effects of particle surface friction and rotary inertia. They considered only the case of high bulk solids fractions where the major stress contributions are the collisional ones. Later Lun (1991) extended their theory to incorporate the kinetic stresses as well as the kinetic and collisional energy flux for a system of slightly inelastic and slightly rough spheres. In the above theories, two granular temperatures are involved. The first is translational granular temperature, which measures the energy associated with the translational velocity fluctuations. The second is rotational granular temperature. Additional conservation equations for angular momentum and rotational granular temperature were used. Recently, Jenkins and Zhang (2002) simplified the theory to obtain a simple model for rapid flow of identical, slightly frictional, nearly elastic spheres. Details of this model can been found in chapter 5, where application of this model in a multi-fluid formulation has been made.

The dissipative dynamics feature of granular flow makes the assumptions for Chapman-Enskog expansion invalid unless the inelasticity is very small. The kinetic theory of granular flow was limited to a very weak dissipation situation. More recently, a generalization of the Chapman-Enskog expansion for granular flows has been proposed in Brey et al. (1998). This method employs the homogeneous cooling state (HCS) as its zeroth order and uses an expansion in powers of Knudsen number as in the original Chapman-Enskog method. As this method does not employ inelasticity as a small parameter, it is formally correct for all physical values of inelasticity. However, it is unclear whether the use of a local HCS as a zeroth order term in this Chapman-Enskog expansion is justified in principle. This method has already been applied to dense granular flow (Garzó and Dufty, 1999b) and low density binary mixtures (Garzó and Dufty, 2002).

2.1.2 Macroscale models for transition and slow dense granular flows

It is clear that a rapid shear granular flow is seldom realized in nature or in industrial processes. Even if it does occur, it often coexists with a slow flow or a quasi-static regime (Shen and Babic, 1999; Campbell, 2002). For example, in a gas fluidized bed of a binary mixture, the large particles may not be well fluidized when the gas velocity is between the two minimum fluidization velocities for the two different types of particles. The closely packed particles may hinder the segregation of smaller particles (Gera et al., 2004). Many practical flow situations, especially those strongly affected by gravitational forces, fall into a transitional regime (Savage, 1998). It is extremely difficult to construct theoretical models, which are capable to describe the transition and slow dense flow behaviors.

Early models simply *ad hoc* patched together the results taken from KTGF for rapid shear regime and from soil mechanics for plastic regime by assuming simple additivity (Johnson and Jackson, 1987; Srivastava and Sundaresan, 2003) or by switching according to voidage (Syamlal et al., 1993). However, the addition of "frictional" stress (Johnson and Jackson, 1987; Srivastava and Sundaresan, 2003) to collisional stress made extra "frictional" contribution to the solid stress for situations where there is no "frictional" stress. The switching method only considered the voidage regardless of other influences, e.g., the shear rate, on the real solid constitutive behavior. The plastic model failed to capture the no shear zone. For example, the stagnant flow regimes in the hopper shoulders could not be captured (Srivastava and Sundaresan, 2003). Nevertheless, there have been more promising theoretical model developments to capture the transition and slow dense behaviors, some of which are reviewed next.

Savage (1998) proposed a continuum theory based on associated flow rule that relates the strain rate and the shear stress in plastic frictional systems. Averaging strain rate fluctuations yields a Bingham-like constitutive relation, in which the shear stress and strain rate tensors are always coaxial. Furthermore, it also postulates that the viscosity diverges as the density approaches the close-packing limit. A problem of slow granular flow in rough-walled vertical chute flow was studied by this model. A concentration boundary layer being thicker than the velocity boundary layer was obtained, which was consistent with experimental observations.

Aranson and Tsimring (2001, 2002) employed a different approach based on the order parameter description of granular matter. The stress was decomposed into a "fluid" and a "static" part, i.e., $\sigma = \sigma^{\mathrm{f}} + \sigma^{\mathrm{s}}$. The value of the order parameters specifies the ratio between static and "fluid" parts of the stress tensor. The order parameter was assumed to obey dissipative dynamics governed by a free energy functional with two local minima. This description was based on the separation of static and fluid components of the shear stress and assumed Newtonian friction law for the fluid components. The viscosity coefficient is expected to remain finite at the fluidization threshold (Volfson et al., 2003a,b, 2004). The model yields a good qualitative description of many phenomena occurring in granular flows. However, the model is limited to two dimensions (2D) and the correlation of the order parameters was fitted from only 2D molecular simulations. The stress tensor in this model was correctly generalized to an objective form that is independent of the coordinate system by Gao et al. (2005). The objective representation correctly models the isotropic and anisotropic parts of the stress tensor. This general objective form of the model also relaxes the assumption in the original model that the principal axes of the granular stress tensor be coaxial with that of the fluid stress tensor.

Zhang and Rauenzahn (1997) used an ensemble averaging technique to examine the effects of finite particle interaction time and multi-particle collisions and developed a viscoelastic model for granular particles coated with resin. The model predicts that the shear stress is quadratically proportional to the shear rate when the particle concentration is relatively low and that shear stress depends linearly on the rate of strain. Zhang and Rauenzahn (2000) also analyzed the stress relaxation in dense and slow dry granular flows and derived an evolution equation for the collisional stress based on their statistical method (Zhang and Rauenzahn, 1997), which predicts a finite stress at the limit of zero shear rate associated with plasticity of the granular system. The advantage of their approach is that all the model quantities can be computed for microscale simulations. However, the coefficients in their constitutive model were not determined from microscale simulations or experimental data. They used artificially chosen coefficients to show that the model is capable to predict fluid to solid transition.

From the perspective of continuum mechanics, there are many other different approaches, such as non-Newtonian models, rate independent theory, plasticity theories, viscoelastic theories, hypoplastic theory, micropolar models, turbulence models, multiple natural configurations theory, etc.. These are not reviewed here but the readers are referred to an excellent review article by Massoudi (2004).

2.2 Microscale (discrete) modeling of granular flows and segregation

Alternative to the continuum model of granular flows, microscale modeling for granular flows treats granular material as a collection of discrete particles and resolves the particle interaction at the individual particle scale. The particle properties and interaction laws are used with a molecular dynamics (MD) algorithm to get the collective behavior of the dissipative many-body system. The microscale modeling of particles can be used to capture physical behaviors of granular flows usually at a more accurate level than a continuum description, even when coupled with averaged Navier-Stokes equations for the fluid phase (Goldschmidt, 2001; Bokkers et al., 2004). Therefore, microscale simulations can produce useful information to derive macroscopic constitutive relations needed to describe the material within the framework of a macroscale continuum theory. The microscale simulations also serve to validate the continuum models by testing the validation of their underlying assumptions and the range of their applications in terms of all the control parameters (e.g., inelasticity, size, solid fractions, etc.).

There basically exists two different approaches, the so-called soft sphere MD method and the hard sphere, event-driven method. The former is straightforward, easy to generalize, and has numerous applications, while the latter is optimized for rigid interactions and is mainly used for collisional, dissipative granular gases.

The idea of MD is to numerically integrate the equations of motion for all the particles in the system (Allen and Tildesley, 1987; Rapaport, 2004). Soft sphere MD for granular flows or discrete element model (DEM) is to supply contact force models for solid particles to the MD algorithm. [1] Pioneering work in this field was done by Cundall and Strack (1979) and Walton (1992). Many more sophisticated engineering mechanics models have been developed to describe the contact force (Thornton, 1999). Since the realistic modeling of the deformations of the particles is much too complicated, a simplified contact force and the overlap relation (Silbert et al., 2001), the so called spring-dashpot model, is used in this work (demonstrated in chapter 6).

The procedure of soft sphere MD is conceptually simple. However, there are only two-body interactions being employed to characterize a granular system of many particles assuming many-body interactions to result from the sum of the two-particle forces. This assumption may fail for some particular situations. For example, Luding (2004) pointed out that dissipation is very inefficient for long wavelength cooperative modes of motion when many particles are in

---

[1] Note that both methods are identical in spirit, however, different groups of researchers use these (and also other) names.

contact with each other. Furthermore, an accurate description of the simultaneous collision of more than two spheres is not yet available (Hinch, 1995). A relevant disadvantage is that the choice of contact force model may affect the accuracy of the MD method. This cautions us to carefully set up a MD simulation for a real granular system and to be aware of the effect of all kinds of parameters on the phenomena of interest. Despite these disadvantages, soft sphere MD is still a powerful tool to study granular flows when it is being used appropriately.

Most of the soft sphere MD simulations focus on dry granular flows. However, MD has also been coupled with fluid dynamics in hybrid methods to simulate gas solid flows (Tsuji et al., 1993; Xu and Yu, 1997; Yu and Xu, 2003; Feng and Yu, 2007; Beetstra et al., 2007). Volume averaged or instantaneous descriptions of fluid motion were coupled with solid particle motion through interactions between them. However, the details will not be discussed here. The hybrid method used in this work is demonstrated in chapter 7.

In the framework of the hard sphere model, particles are assumed to be perfectly rigid and they follow an undisturbed motion until a collision occurs. Due to the rigidity of the interaction, the collisions occur instantaneously, so that an event-driven simulation method can be used (Lubachevsky, 1991). The interaction force is then impulsive, thus the hard sphere model treats collisions much simpler (than the soft sphere model) by using a collision matrix based on the momentum conservation and energy loss rule. The instantaneous nature of hard sphere collisions is artificial, it is valid when binary collisions dominate and multi-particle contacts are rare. It is mainly useful for simulations of granular gases (Luding and McNamara, 1998; Luding and Herrmann, 1999). However, it has also been applied to simulate dynamics (Hoomans et al., 1996) and segregation (Hoomans et al., 2000) in gas fluidized beds and to test the validation of KTGF in a dense fluidized beds (Goldschmidt et al., 2002).

2.3 Transition from microscale to macroscale

From section 2.1, it can be seen that the macroscale continuum models rely on constitutive equations, which are functions of velocity, stress, strain and other physical quantities, to describe the state of the system. On the microscale, however, the physical quantities are at the individual particle level. Therefore, a so called micro-macro transition (Kirkwood et al., 1949; Luding and Pöschel, 2001) needs to be performed to obtain the physical quantities at the macroscale. The framework through which microscale models reduce to macroscale continuum ones includes irreversible thermodynamics (Truesdell, 1984; Beris and Edwards, 1994; Öttinger, 2005), non-equilibrium statistical mechanics (Chapman and Cowling, 1970; Evans and Morriss, 1990), etc. The continuum models reviewed in section 2.1 provided a few examples. However, the whole topic of the framework is too vast to review here.

What is of particular interest in this work is how to obtain macroscale quantities from the microscale simulations. For this purpose, the homogenization theory in micromechanics, which has been applied to granular material to establish micro-macro relations (Walton, 1987; Emeriault and Cambou, 1996), is used. While it is straightforward to average velocity, density and spin, the stress and strain definitions were given slightly different in the literature (Savage and Jeffrey, 1981; Kruyt and Rothenburg, 1996). Lätzel et al. (2000) and Luding et al. (2001) recently derived macroscale stress and strain equations, which can be easily used based on quantities from discrete element simulations. Their results indicate two contributions to the stress. The first is the dynamic stress due to momentum flux, a kinetic energy density. The second is the static stress due to particle contact, a potential energy density.

For dynamic systems, there is momentum transport via flux of the particles (Luding, 2004). This contribution to the stress tensor is the standard stress in an ideal gas, where the atoms move with a certain fluctuation velocity. In the general case, the dynamic stress in a sample volume V is $\sigma^{\mathbf{d}} = 1/V \sum_i^n m_i \mathbf{C}_i \mathbf{C}_i$, which is a dyadic product of the fluctuation velocity giving a second order tensor with trace $\mathrm{tr}(\sigma^{\mathbf{d}})/D = nT$ being the kinetic energy density in D dimensions. The dynamic stress is essentially identical to the kinetic part of the pressure tensor in kinetic theory (see equation 3.50).

The additional contribution to the stress is due to collisions and contacts, which can be derived from the principle of virtual displacement for soft interaction potentials and can be modified for hard sphere systems (Luding, 2004). The static stress is given as $\sigma^s = 1/V \sum_i^n \sum_{j,j\neq i} \frac{1}{2} \mathbf{r}_{ij} \mathbf{F}_{ij}$. Combining the dynamic and static contributions, the stress tensor for the soft sphere system is:

$$\sigma = \frac{1}{V} \sum_{i}^{n} \left[m_i \mathbf{C}_i \mathbf{C}_i + \sum_{j,j \neq i} \frac{1}{2} \mathbf{r}_{ij} \mathbf{F}_{ij} \right], \tag{2.3}$$

which will be used to determine solid stresses from soft sphere MD simulations.

2.4 Summary

In this chapter, the fundamental macroscale, microscale and hybrid methods for modeling granular flows have been reviewed with emphasis on the capability to predict segregation. The review guides the research to determine the capabilities and limitations of the state-of-art models and to contribute to the new understanding and development of the models.

CHAPTER 3. BASIC THEORIES AND NUMERICAL FORMULATIONS

In this chapter, the hydrodynamic theory for the multi-fluid model and kinetic theory for granular flows are presented. The numerical formulations to solve the hydrodynamic equation system are also shown. This chapter serves to give a overview of the theoretical basis for the entire research work for this thesis.

3.1 Hydrodynamic theory for multi-fluid model

The multi-fluid model for multiphase flow assumes that different phases behave as interpenetrating continua and the instantaneous variables are averaged over a region which is larger than the particle spacing but much smaller than the flow domain. Multiple types of particles should be considered to describe phenomena such as particle segregation and elutriation. Each particle type has a unique diameter with identical material properties (Syamlal et al., 1993).

3.1.1 Governing Equations

The field variables, called phasic volume fractions, are used to determine the fraction of the average volume occupied by each phase. The sum of all of the volume fractions, both for the gas phase and the m^{th} solids phases, where m denotes a unique solids phase, must equal unity

$$\varepsilon_{\mathrm{g}} + \sum_{m=1}^{\mathrm{M}} \varepsilon_{sm} = 1$$

The subscript g indicates the gas phase and s indicates solids phases with the total number of solids phase M. The gas phasic volume fraction is also called the void fraction. The effective densities of the gas phase ρ'_{g} and solids phases $\rho'_{\mathrm{s}m}$ respectively, are

$$\begin{aligned}\rho'_{\mathrm{g}} &= \varepsilon_{\mathrm{g}}\rho_{\mathrm{g}} \\ \rho'_{\mathrm{s}m} &= \varepsilon_{\mathrm{s}m}\rho_{\mathrm{s}m}\end{aligned}$$

The continuity equations for the gas phase and the solids phase m, respectively, are

$$\frac{\partial}{\partial t}(\varepsilon_{\mathrm{g}}\rho_{\mathrm{g}}) + \nabla\cdot(\varepsilon_{\mathrm{g}}\rho_{\mathrm{g}}\vec{v}_{\mathrm{g}}) = \sum_{n=1}^{N_{\mathrm{g}}} R_{\mathrm{g}n} \tag{3.1}$$

$$\frac{\partial}{\partial t}(\varepsilon_{\mathrm{s}m}\rho_{\mathrm{s}m}) + \nabla\cdot(\varepsilon_{\mathrm{s}m}\rho_{\mathrm{s}m}\vec{v}_{\mathrm{s}m}) = \sum_{n=1}^{N_{\mathrm{s}m}} R_{\mathrm{s}mn} \tag{3.2}$$

The first and second terms on the left sides of Eqs. (3.1) and (3.2) are the rate of mass generation per unit volume and the net rate of convective mass flux. The terms of $R_{\mathrm{g}n}$ and $R_{\mathrm{s}mn}$ on the right sides account for interphase mass transfer due to chemical reactions or physical processes.

The momentum equations for the gas phase and the solids phase m have the form

$$\frac{\partial}{\partial t}(\varepsilon_{\mathrm{g}}\rho_{\mathrm{g}}\vec{v}_{\mathrm{g}}) + \nabla\cdot(\varepsilon_{\mathrm{g}}\rho_{\mathrm{g}}\vec{v}_{\mathrm{g}}\vec{v}_{\mathrm{g}}) = \nabla\cdot\overline{\overline{S}}_{\mathrm{g}} + \varepsilon_{\mathrm{g}}\rho_{\mathrm{g}}\vec{g} - \sum_{m=1}^{\mathrm{M}}\vec{I}_{\mathrm{g}m} + \vec{f}_{\mathrm{g}} \tag{3.3}$$

$$\frac{\partial}{\partial t}(\varepsilon_{\mathrm{s}m}\rho_{\mathrm{s}m}\vec{v}_{\mathrm{s}m}) + \nabla\cdot(\varepsilon_{\mathrm{s}m}\rho_{\mathrm{s}m}\vec{v}_{\mathrm{s}m}\vec{v}_{\mathrm{s}m}) = \nabla\cdot\overline{\overline{S}}_{\mathrm{s}m} + \varepsilon_{\mathrm{s}m}\rho_{\mathrm{s}m}\vec{g} + \vec{I}_{\mathrm{g}m} - \sum_{\substack{l=1\\ l\neq m}}^{\mathrm{M}}\vec{I}_{ml} \tag{3.4}$$

The first terms on the left sides of Eqs. (3.3) and (3.4) are the net rate of momentum generation and the second terms are the net rate of momentum transfer by convection. Equations (3.3) and (3.4) include the gas phase and solids phase stress tensors $\overline{\overline{S}}_{\mathrm{g}}$ and $\overline{\overline{S}}_{\mathrm{s}m}$, the body forces due to gravity $\vec{g}$, the flow resistance force $\vec{f}_{\mathrm{g}}$ due to internal porous surfaces, the interaction force $\vec{I}_{\mathrm{g}m}$ accounting for the momentum transfer between the gas phase and the m^{th} solids phase, and the interaction force $\vec{I}_{lm}$ between the m^{th} and l^{th} solids phases.

The internal energy balances for the gas and solids phase m are

$$\varepsilon_{\mathrm{g}}\rho_{\mathrm{g}}C_{\mathrm{pg}}\left(\frac{\partial T_{\mathrm{g}}}{\partial t} + \vec{v}_{\mathrm{g}}\cdot\nabla T_{\mathrm{g}}\right) = -\nabla\cdot\vec{q}_{\mathrm{g}} - \sum_{m=1}^{\mathrm{M}} H_{\mathrm{g}m} - \Delta H_{\mathrm{rg}} + H_{\mathrm{wall}}(T_{\mathrm{wall}} - T_{\mathrm{g}}) \tag{3.5}$$

$$\varepsilon_{\mathrm{s}m}\rho_{\mathrm{s}m}C_{\mathrm{ps}m}\left(\frac{\partial T_{\mathrm{s}m}}{\partial t} + \vec{v}_{\mathrm{s}m}\cdot\nabla T_{\mathrm{s}m}\right) = -\nabla\cdot\vec{q}_{\mathrm{s}m} + H_{\mathrm{g}m} - \Delta H_{\mathrm{rs}m} \tag{3.6}$$

with temperature T and constant pressure specific heats C_p. Equations (3.5) and (3.6) include the conductive heat flux $\vec{q}_\mathrm{g}$ and $\vec{q}_{\mathrm{s}m}$, the gas-solids interphase heat transfer $H_{\mathrm{g}m}$, and the heats of reaction ΔH_rg and $\Delta H_{\mathrm{rs}m}$. The last term in Eq. (3.5) is the heat loss to the wall. Heat transfer between different solids phases and radiative heat transfer are negligible.

The gas and solids phases are formulated to represent an arbitrary number of chemical species, N_g and $N_{\mathrm{s}m}$. The corresponding conservation of species for the gas and solids phases are

$$\frac{\partial}{\partial t}(\varepsilon_\mathrm{g}\rho_\mathrm{g}X_{\mathrm{g}n}) + \nabla\cdot(\varepsilon_\mathrm{g}\rho_\mathrm{g}X_{\mathrm{g}n}\vec{v}_\mathrm{g}) = R_{\mathrm{g}n} \tag{3.7}$$

$$\frac{\partial}{\partial t}(\varepsilon_{\mathrm{s}m}\rho_{\mathrm{s}m}X_{\mathrm{s}mn}) + \nabla\cdot(\varepsilon_{\mathrm{s}m}\rho_{\mathrm{s}m}X_{\mathrm{s}mn}\vec{v}_{\mathrm{s}m}) = R_{\mathrm{s}mn} \tag{3.8}$$

where X is the mass fraction. Equations (3.7) and (3.8) include accumulation, convection and the rate of reaction but neglect diffusive fluxes.

The chemical source terms are closed by reaction kinetic expressions in the species balance equations. It should be noted that the chemical source terms involve a wide range of time scales which will make the equations stiff. Therefore, efficient algorithms must be used to treat these terms.

3.1.2 Constitutive relations

The complete formulation requires that the governing equations be closed. A wide range of constitutive relations can be found by using different approaches, from empirical information to kinetic theory. Most differences between multiphase theories originate from closure assumptions. The closure models used in this research are introduced next.

3.1.2.1 Gas-phase equation of state

The equation of state for the gas phase assumes ideal gas behavior,

$$\rho_\mathrm{g} = \frac{P_\mathrm{g}M_\mathrm{w}}{RT_\mathrm{g}}$$

where P_g is the gas pressure, M_w is the molecular weight and R is the universal gas constant. For an incompressible gas the density is assumed to be constant.

3.1.2.2 Gas-Solids momentum transfer

From previous studies on the dynamics of a single particle in a gas, three important mechanisms for the gas-solids interaction force $\vec{I}_{\mathrm{g}m}$ are considered: drag force, caused by velocity differences between gas-solids phases; buoyancy, caused by the gas pressure gradient; and momentum transfer due to mass transfer between phases. Other forces, such as virtual mass effect caused by relative acceleration between phases, Magnus force caused by particle spin and so on, are not considered. Thus, the gas-solids momentum interaction force becomes

$$\vec{I}_{\mathrm{g}m} = -\varepsilon_{\mathrm{s}m}\nabla P_{\mathrm{g}} - F_{\mathrm{g}m}(\vec{v}_{\mathrm{s}m} - \vec{v}_{\mathrm{g}}) + R_{0m}[\zeta_{0m}\vec{v}_{\mathrm{s}m} + \bar{\zeta}_{0m}\vec{v}_{\mathrm{g}}] \tag{3.9}$$

where R_{0m} is the mass transfer from the gas phase to solids phase m, and

$$\zeta_{0m} = \begin{cases} 1 & \text{for } R_{0m} < 0 \\ 0 & \text{for } R_{0m} > 0 \end{cases}$$

for $\overline{\zeta}_{0m} = 1 - \zeta_{0m}$,

The gas-solids drag formulation for converting terminal velocity correlations to drag correlations (Syamlal et al., 1993) is

$$F_{\mathrm{g}m} = \frac{3\varepsilon_{\mathrm{s}m}\varepsilon_{\mathrm{g}}\rho_{\mathrm{g}}}{4V_{rm}^2 d_{\mathrm{p}m}} C_{\mathrm{DS}}\left[\frac{Re_m}{V_{rm}}\right] |\vec{v}_{\mathrm{s}m} - \vec{v}_{\mathrm{g}}| \tag{3.10}$$

where $d_{\mathrm{p}m}$ is the diameter and V_{rm} is the terminal velocity correlation for the m^{th} solids phase.

$$V_{rm} = 0.5\left(A - 0.06Re_m + \sqrt{(0.06Re_m)^2 + 0.12Re_m(2B - A) + A^2}\right) \tag{3.11}$$

where A and B are the functions of void fraction

$$A = \varepsilon_{\mathrm{g}}^{4.14}, \tag{3.12}$$

and

$$B = \begin{cases} C\varepsilon_g^{1.28} & \text{if } \varepsilon_g \leq 0.85 \\ \varepsilon_g^{D} & \text{if } \varepsilon_g > 0.85. \end{cases} \tag{3.13}$$

The coefficients C and D can be calibrated against experimental data and are set to 0.8 and 2.65, respectively. Note that the coefficients C and D have to satisfy the relation

$$C0.85^{1.28} = 0.85^{D} \tag{3.14}$$

to guarantee the continuity of the function B at $\varepsilon_g = 0.85$. The Reynolds number of the m^{th} solids phase is

$$Re_m = \frac{d_{\text{p}m}|\vec{v}_{\text{s}m} - \vec{v}_{\text{g}}|\rho_{\text{g}}}{\mu_{\text{g}}} \tag{3.15}$$

The single sphere drag function (Dalla Valla, 1948) has the form

$$C_{\text{DS}}\left[\frac{Re_m}{V_{rm}}\right] = \left[0.63 + \frac{4.8}{\sqrt{Re_m/V_{rm}}}\right]^2 \tag{3.16}$$

Equations (3.11), (3.15) and (3.16) are coupled to (3.10) for the complete description of the gas drag coefficient.

3.1.2.3 Solids-solids momentum transfer

The drag between the phases due to velocity differences is assumed as the major effect in the solids-solids momentum transfer. Thus, the momentum transfer I_{ml} between solids is represented as

$$\vec{I}_{ml} = -F_{\text{s}ml}(\vec{v}_{\text{s}l} - \vec{v}_{\text{s}m}) + R_{ml}[\zeta_{ml}\vec{v}_{\text{s}l} + \bar{\zeta}_{ml}\vec{v}_{\text{s}m}] \tag{3.17}$$

where R_{ml} is the mass transfer from solids phase m to solids phase l,

$$\zeta_{ml} = \begin{cases} 1 & \text{for } R_{ml} < 0 \\ 0 & \text{for } R_{ml} > 0 \end{cases}$$

and $\bar{\zeta}_{ml} = 1 - \zeta_{ml}$,

The drag coefficient $F_{\text{s}ml}$ is derived by using a simplified version of kinetic theory (Syamlal, 1987a)

$$F_{\text{s}ml} = \frac{3(1+e_{lm})(\pi/2 + C_{\text{f}lm}\pi^2/8)\varepsilon_{\text{s}l}\rho_{\text{s}l}\varepsilon_{\text{s}m}\rho_{\text{s}m}(d_{\text{p}l} + d_{\text{p}m})^2 g_{0_{lm}}|\vec{v}_{\text{s}l} - \vec{v}_{\text{s}m}|}{2\pi(\rho_{\text{s}l}d_{\text{p}l}^3 + \rho_{\text{s}m}d_{\text{p}m}^3)} \tag{3.18}$$

where e_{lm} and $C_{\text{f}lm}$ are the coefficient of restitution and coefficient of friction, between the l^{th} and m^{th} solids-phase particles, and $g_{0_{lm}}$ is the radial distribution function at contact for a mixture of hard spheres.

3.1.2.4 Gas phase stress tensor

The gas phase stress tensor has two parts: the pressure contribution and the Newtonian viscous stress tensor, which is given by

$$\overline{\overline{S}}_{\mathrm{g}} = -P_{\mathrm{g}}\overline{\overline{I}} + \overline{\overline{\tau}}_{\mathrm{g}} \tag{3.19}$$

The viscous stress tensor, $\overline{\overline{\tau}}_{\mathrm{g}}$, is

$$\overline{\overline{\tau}}_{\mathrm{g}} = 2\varepsilon_{\mathrm{g}}\mu_{\mathrm{g}}\overline{\overline{D}}_{\mathrm{g}} + \varepsilon_{\mathrm{g}}\lambda_{\mathrm{g}}\mathrm{tr}(\overline{\overline{D}}_{\mathrm{g}})\overline{\overline{I}} \tag{3.20}$$

where $\overline{\overline{I}}$ is the identity tensor and $\overline{\overline{D}}_{\mathrm{g}}$ is the strain rate tensor for the gas phase

$$\overline{\overline{D}}_{\mathrm{g}} = \frac{1}{2}\left[\nabla\vec{v}_{\mathrm{g}} + (\nabla\vec{v}_{\mathrm{g}})^{T}\right]$$

3.1.2.5 Solids phase stress tensor

In the solid phase stress tensor term, a solids pressure is calculated to ensure that the volume fraction does not exceed the packed-bed volume fraction. This can be accomplished by treating the particles as an incompressible fluid at a critical void fraction and the pressure is set to zero when the void fraction becomes greater than the packed-bed void fraction (Syamlal and O'Brien, 1988).

Granular flow theory is used to describe the solids phase stresses in detail. There are two distinct flow regimes in granular flow: a viscous or rapidly shearing regime in which stresses arise due to collisional or translational momentum transfer, and a plastic or slowly shearing regime in which stresses arise due to Coulomb friction between grains in close contact. Two different approaches are used for these regimes:

$$\overline{\overline{S}}_{sm} = \begin{cases} -P^{\mathrm{p}}_{sm}\overline{\overline{I}} + \overline{\overline{\tau}}^{\mathrm{p}}_{sm} & \text{if } \varepsilon_{\mathrm{g}} \le \varepsilon^{*}_{\mathrm{g}} \\ -P^{\mathrm{v}}_{sm}\overline{\overline{I}} + \overline{\overline{\tau}}^{\mathrm{v}}_{sm} & \text{if } \varepsilon_{\mathrm{g}} > \varepsilon^{*}_{\mathrm{g}} \end{cases}$$

where P^{p}_{sm} and $\overline{\overline{\tau}}^{\mathrm{p}}_{sm}$ are the pressure and the viscous stress in the m^{th} solids phase for the plastic regime, P^{v}_{sm} and $\overline{\overline{\tau}}^{\mathrm{v}}_{sm}$ are the pressure and the viscous stress for the viscous regime, and $\varepsilon^{*}_{\mathrm{g}}$ is a critical packing number, usually set to the void fraction at minimum fluidization.

The granular stress equation based on kinetic theory (Syamlal, 1987b) is applied to the viscous regime. The granular pressure and stresses are given by

$$P^{\mathrm{v}}_{\mathrm{sm}} = K_{1m}\varepsilon^2_{sm}\theta_m \tag{3.21}$$

$$\overline{\overline{\tau}}^{\mathrm{v}}_{sm} = 2\mu^{\mathrm{v}}_{\mathrm{sm}}\overline{\overline{D}}_{\mathrm{sm}} + \lambda^{\mathrm{v}}_{\mathrm{sm}}\mathrm{tr}(\overline{\overline{D}}_{\mathrm{sm}})\overline{\overline{I}} \tag{3.22}$$

where θ_m is the granular temperature and $\lambda^{\mathrm{v}}_{sm}$ is the second coefficient of viscosity,

$$\lambda^{\mathrm{v}}_{sm} = K_{2m}\varepsilon_{\mathrm{sm}}\sqrt{\theta_m}$$

The shear viscosity factor μ^{v}_{sm} is

$$\mu^{\mathrm{v}}_{sm} = K_{3m}\varepsilon_{\mathrm{sm}}\sqrt{\theta_m}$$

The strain rate tensor, $\overline{\overline{D}}_{sm}$, is given by

$$\overline{\overline{D}}_{\mathrm{sm}} = \frac{1}{2}\left[\nabla\vec{v}_{\mathrm{sm}} + (\nabla\vec{v}_{\mathrm{sm}})^T\right]$$

and K_{1m}, K_{2m} and K_{3m} are

$$K_{1m} = 2(1+e_{mm})\rho_{\mathrm{sm}}g_{0mm}, \tag{3.23}$$

$$K_{2m} = \frac{4d_{pm}\rho_{sm}(1+e_{mm})\varepsilon_{\mathrm{sm}}g_{0mm}}{3\sqrt{\pi}} - \frac{2}{3}K_{3m}, \tag{3.24}$$

$$K_{3m} = \frac{d_{pm}\rho_{sm}}{2}\left\{\frac{\sqrt{\pi}}{3(3-e_{mm})}\left[1+0.4(1+e_{mm})(3e_{mm}-1)\varepsilon_{\mathrm{sm}}g_{0mm}\right] + \frac{8\varepsilon_{sm}g_{0mm}(1+e_{mm})}{5\sqrt{\pi}}\right\}. \tag{3.25}$$

In the plastic flow regime, frictional flow theory (Jenike, 1987) provides an arbitrary function that allows a certain amount of compressibility in the solids phase where

$$P^{\mathrm{p}}_{\mathrm{sm}} = \varepsilon_{\mathrm{sm}}P^* \tag{3.26}$$

and P^* is expressed by an empirical power law

$$P^* = A(\varepsilon^*_{\mathrm{g}} - \varepsilon_{\mathrm{g}})^n$$

for values of $A = 10^{25}$ and $n = 10$.

The solids stress tensor is calculated for solid phase m using the formulation (Schaeffer, 1987)

$$\overline{\overline{\tau}}^{\mathrm{p}}_{\mathrm{sm}} = 2\mu^p_{\mathrm{sm}}\overline{\overline{D}}_{\mathrm{sm}} \tag{3.27}$$

3.1.2.6 Gas-solids heat transfer

The heat transfer between the gas and solids phases is a function of a temperature difference

$$H_{\mathrm{g}m} = -\gamma_{\mathrm{g}m}(T_{\mathrm{s}m} - T_{\mathrm{g}}) \tag{3.28}$$

where $\gamma_{\mathrm{g}m}$ is the heat transfer coefficient between the gas phase and the m^{th} solids phase. The heat transfer coefficient $\gamma_{\mathrm{g}m}$ (Bird et al., 1960) is corrected using the coefficient $\gamma^0_{\mathrm{g}m}$ by adding the influence of the interphase mass transfer,

$$\gamma_{\mathrm{g}m} = \frac{C_{\mathrm{pg}} R_{0m}}{e^{(C_{\mathrm{pg}} R_{0m} \;/\gamma^0_{\mathrm{g}m})} - 1}$$

and the coefficient $\gamma^0_{\mathrm{g}m}$ is

$$\gamma^0_{\mathrm{g}m} = \frac{6 k_{\mathrm{g}} \varepsilon_{\mathrm{s}m} Nu_m}{d^2_{\mathrm{p}m}}$$

The correlation is applicable for a porosity range of 0.35–1.0 and a Reynolds number up to 10^5.

3.1.2.7 Conductive heat flux in gas and solids phase

The conductive heat fluxes for both the gas and solids phases are described according to Fourier's law

$$\vec{q}_{\mathrm{g}} = -\varepsilon_{\mathrm{g}} k_{\mathrm{g}} \nabla T_{\mathrm{g}} \tag{3.29}$$

$$\vec{q}_{\mathrm{s}m} = -\varepsilon_{\mathrm{s}m} k_{\mathrm{s}m} \nabla T_{\mathrm{s}m} \tag{3.30}$$

where k_{g} and $k_{\mathrm{s}m}$ are the thermal conductivity for gas and particle phases, respectively. The particle thermal conductivity (Syamlal and Gidaspow, 1985) has the form

$$\frac{k_{\mathrm{s}m}}{k_{\mathrm{g}}} = \frac{[\Phi_k R_{km} + (1-\Phi_k)\lambda_{rm}]}{\sqrt{1-\varepsilon_{\mathrm{g}}}}, \tag{3.31}$$

where

$$\lambda_{rm} = -\frac{2}{1 - b/R_{km}} \left[\frac{(R_{km}-1)b/R_{km}}{(1-b/R_{km})^2} \ln(b/R_{km}) + \frac{b-1}{(1-b/R_{km})} + \frac{b+1}{2} \right], \tag{3.32}$$

and, for spherical particles,

$$b = 1.25 \left(\frac{1-\varepsilon_{\mathrm{g}}}{\varepsilon_{\mathrm{g}}} \right)^{10/9}. \tag{3.33}$$

The contact area fraction has the value $\Phi_k = 7.26 \times 10^{-3}$.

3.1.2.8 Heat of reaction

The heat of reaction accounts for the difference in temperatures between phases by partitioning reaction processes between each phase. Partitioning of the heat is arbitrary since the averaging required to derive the hydrodynamic equations does not contain any information regarding the gas-solids interface. The actual chemical reactions occur in an interface region, however, the partitioning of the heats of reaction must be based on physical arguments. For example, to partition the heat of the coal combustion reaction $\mathrm{C} + \mathrm{O}_2 \rightarrow \mathrm{CO}_2$, the heat of reaction for the step $\mathrm{C} + \frac{1}{2}\mathrm{O}_2 \rightarrow \mathrm{CO}$ is assigned to the solids phase (ΔH_{rs} in Eq. (3.6)) and the heat of reaction for the step $\mathrm{CO} + \frac{1}{2}\mathrm{O}_2 \rightarrow \mathrm{CO}_2$ is assigned to the gas phase (ΔH_{rg} in Eq. (3.5)).

3.1.2.9 Granular energy equations

The constitutive relation for granular flow is based on kinetic theory of smooth, slightly inelastic, spherical particles. The relationship contains the granular temperature θ_m which is proportional to the granular energy of the continuum. The granular temperature is introduced as a measure of the particle velocity fluctuations

$$\frac{3}{2}\theta_m = \frac{1}{2}\langle \vec{C}_m^2 \rangle$$

where $\vec{C}_m$ is the fluctuating component of the instantaneous velocity $\vec{c}_m$ of the m^{th} solids phase

$$\vec{c}_m = \vec{v}_{\mathrm{sm}} + \vec{C}_m$$

The transport of granular energy is

$$\frac{3}{2}\left[\frac{\partial(\varepsilon_{\mathrm{sm}}\rho_{\mathrm{sm}}\theta_m)}{\partial t} + \nabla\cdot(\varepsilon_{\mathrm{sm}}\rho_{\mathrm{sm}}\theta_m)\vec{v}_{\mathrm{sm}}\right] = \overline{\overline{S}}_{sm} : \nabla\vec{v}_{\mathrm{sm}} - \nabla\cdot\vec{q}_{\theta_m} - \gamma_{\theta_m} + \Phi_{\mathrm{g}m} + \sum_{l=1, l\neq m}^{\mathrm{M}} \Phi_{lm} \quad (3.34)$$

where γ_{θ_m} is the rate of granular energy dissipation due to inelastic collisions of the form (Lun et al., 1984)

$$\gamma_{\theta_m} = K_{4m}\varepsilon_{\mathrm{sm}}^2\theta_m^{\frac{3}{2}}$$

and $\vec{q}_{\theta_m}$ is the diffusive flux of granular energy

$$\vec{q}_{\theta_m} = -k_{\theta_m}\nabla\theta_m$$

The term Φ_{gm} is the transfer of granular energy between the gas phase and the m^{th} solids phase, and Φ_{lm} accounts for the transfer of granular energy between the m^{th} and l^{th} solids phases. The formulation for granular energy transfer (Ding and Gidaspow, 1990) is

$$\Phi_{gm} = -3F_{gm}\theta_m$$

and Φ_{lm} is ignored by setting $\Phi_{lm} = 0$.

3.1.3 Initial and boundary conditions

3.1.3.1 Initial conditions

The initial values of all field variables must be specified for the entire computational domain. However, the initial conditions are usually not of interest, and the solution is governed by the boundary conditions. Therefore, the initial conditions need only be physically correct to initiate convergence of the equations.

3.1.3.2 Boundary conditions

Two types of inflow boundary conditions are possible, constant velocity or constant mass flux. Specifying constant pressure is the most common condition for the fluid outflow boundary. At impermeable walls, the normal velocities are set to zero. The condition for the tangential components is specified either as a non-slip or as a free-slip condition. The fixed temperature and specified heat flux can be used as thermal boundary conditions. For species equations, either specified species concentration or species diffusion flux can be used.

3.2 Kinetic theory for granular flows

The procedure of deriving the constitutive equations for the solid stress tensor in section 3.1.2.5 and the granular energy flux and dissipation in section 3.1.2.9 is presented next. In kinetic theory, a system of N spheres of diameter σ, mass m and velocity $\mathbf{c}$ is considered.The state of the granular flow is described by particle velocity distribution functions. The evolution of velocity distribution functions is governed by the Boltzmann equation

$$\frac{\partial f}{\partial t} + \mathbf{c} \cdot \frac{\partial f}{\partial \mathbf{r}} + \mathbf{F} \cdot \frac{\partial f}{\partial \mathbf{c}} = \left(\frac{\partial f}{\partial t} \right)_{\text{coll}}, \tag{3.35}$$

where $\mathbf{r}$ is the position vector of a particle, $\mathbf{F}$ is external force and $\left(\frac{\partial f}{\partial t}\right)_{\text{coll}}$ is equal to the rate of change in the velocity distribution function f at a fixed point due to collisions. It can be expressed as an integral evaluating collision effects on the distribution function. (In dense flows, the collision integral is modified according to Enskog (Chapman and Cowling, 1970). The thus modified equation 3.35 is referred as the Enskog kinetic equation.)

The single-particle velocity distribution function $f^{(1)}(\mathbf{c}, \mathbf{r}, t)$ is defined so that $f^{(1)}(\mathbf{c}, \mathbf{r}, t)\mathrm{d}\mathbf{c}$ is the probable number of particles per unit volume at $\mathbf{r}$ and t with velocities in the element $\mathrm{d}\mathbf{c}$ at $\mathbf{c}$. Integrating $f^{(1)}(\mathbf{c}, \mathbf{r}, t)$ over all velocities gives the local number density of particles

$$\int f^{(1)}(\mathbf{c}, \mathbf{r}, t)\mathrm{d}\mathbf{c} = n(\mathbf{r}, t). \tag{3.36}$$

Given any property $\psi(\mathbf{c})$, its mean, or ensemble average, $< \psi >$ is determined in terms of $f^{(1)}$ by

$$< \psi > = \frac{1}{n} \int \psi(\mathbf{c}) f^{(1)}(\mathbf{c}, \mathbf{r}, t)\, \mathrm{d}\mathbf{c}. \tag{3.37}$$

As in the case of molecular gases (or liquids), one can define macroscopic fields for granular flows, such as the granular temperature T, velocity $\mathbf{v} =< \mathbf{c} >$, and mass density $\rho =< m >$. It is common to define the granular temperature in a slightly different way than for molecular gases; T is defined as the average over an ensemble of the square of the fluctuating velocities of the grains:

$$T = \frac{1}{3} < C^2 > \tag{3.38}$$

where $\mathbf{C} = \mathbf{c} - \mathbf{v}$ is the fluctuation velocity of a grain.

The statistics of binary collisions are determined by the complete pair distribution function $f^{(2)}$, a function of two particle velocities, positions and time, defined so that

$$f^{(2)}(\mathbf{c}_1, \mathbf{r}_1, \mathbf{c}_2, \mathbf{r}_2, t)\, \mathrm{d}\mathbf{c}_1\, \mathrm{d}\mathbf{r}_1\, \mathrm{d}\mathbf{c}_2\, \mathrm{d}\mathbf{r}_2 \tag{3.39}$$

is, at time t, the probable number of pairs of particles located in the volume elements $\mathrm{d}\mathbf{r}_1$, $\mathrm{d}\mathbf{r}_2$ centered at the points $\mathbf{r}_1$ and $\mathbf{r}_2$ and having velocities in the ranges $\mathrm{d}\mathbf{c}_1$ and $\mathrm{d}\mathbf{c}_2$ at $\mathbf{c}_1$ and $\mathbf{c}_2$.

3.2.1 Collision dynamics

Collision dynamics is then needed to determine the quantities exchanged during a collision, i.e., to determine the integrand in the collision integral in equation 3.35. Consider the collision of two identical smooth spherical particles. Quantities associated with each sphere are distinguished by the subscript 1 or 2 and primes denote the values of these quantities following a collision.

The balance of linear momentum requires that the velocity vectors $\mathbf{c}_1'$ and $\mathbf{c}_2'$ of the center of each particle after a collision be related to those $\mathbf{c}_1$ and $\mathbf{c}_2$ before the collision by

$$m\mathbf{c}_1' = m\mathbf{c}_1 - \mathbf{J}, \quad m\mathbf{c}_2' = m\mathbf{c}_2 + \mathbf{J}, \tag{3.40}$$

where $\mathbf{J}$ is the impulse of the force exerted by particle 1 upon particle 2 in the collision. The relative velocity $\mathbf{c}_{12}'$ of the centers of the particles after the collision is

$$\mathbf{c}_{12}' \equiv \mathbf{c}_1' - \mathbf{c}_2'. \tag{3.41}$$

Its component normal to the plane of contact can be related to the corresponding component prior to the collision by

$$(\mathbf{k} \cdot \mathbf{c}_{12}') = -e(\mathbf{k} \cdot \mathbf{c}_{12}), \tag{3.42}$$

where $\mathbf{k}$ is the unit vector directed from the center of the first particle to that of the second particle at contact, and e is the coefficient of normal restitution. Depending upon the material of the particle, e may range from zero to unity. When e equals unity, the relative velocities of the centers of the particles are reversed upon collision and energy is conserved. Values of e less than unity involve the dissipation of energy.

With equation 3.41 and equation 3.42, the value of the impulse $\mathbf{J}$ may be expressed in terms of $\mathbf{c}_{12}$ as

$$\mathbf{J} = \frac{1}{2}m(1+e)(\mathbf{k} \cdot \mathbf{c}_{12})\mathbf{k}. \tag{3.43}$$

The energy loss ΔE in the collision is

$$\Delta E = \frac{1}{4}m(e^2-1)(\mathbf{k} \cdot \mathbf{c}_{12})^2. \tag{3.44}$$

Knowing the collision dynamics, the transport equations can be evaluated. To obtain the transport equations, let $\psi(\mathbf{c})$ be any property of a particle. Multiplying equation 3.35 by $\psi(\mathbf{c})$ and integrating over $\mathbf{c}$, a transport equation for $\psi(\mathbf{c})$ is obtained:

$$\frac{\partial}{\partial t}\langle n\psi\rangle = n\langle D\psi\rangle - \boldsymbol{\nabla}\cdot\langle n\mathbf{c}\psi\rangle + \mathbb{C}(\psi), \tag{3.45}$$

where $D\psi \equiv \frac{\mathrm{d}\mathbf{c}}{\mathrm{d}t}\cdot\frac{\partial\psi}{\partial\mathbf{c}} = m^{-1}\mathbf{F}\cdot\frac{\partial\psi}{\partial\mathbf{c}}$ and $\mathbf{F} = \mathbf{F}(\mathbf{r}, t)$ is the external force acting on a particle, and $\mathbb{C}$ is the mean collisional rate of change of ψ per unit volume. After examining the details of a collision, $\mathbb{C}$ is obtained in the form

$$\mathbb{C}(\psi) = -\boldsymbol{\nabla}\cdot\boldsymbol{\theta}(\psi) + \chi(\psi), \tag{3.46}$$

where the collisional transfer contribution is

$$\begin{aligned}\boldsymbol{\theta} = &-\frac{\sigma^3}{2}\int_{\mathbf{c}_{12}\cdot\mathbf{k}>0}(\psi_1' - \psi_1)(\mathbf{c}_{12}\cdot\mathbf{k})\mathbf{k}\left[1 - \frac{1}{2}\sigma\mathbf{k}\cdot\boldsymbol{\nabla} + \frac{1}{3!}(\sigma\mathbf{k}\cdot\boldsymbol{\nabla})^2 + \cdots\right]\\ &\times f^{(2)}(\mathbf{r}, \mathbf{c}_1; \mathbf{r}+\sigma\mathbf{k}, \mathbf{c}_2; t)\ \mathrm{d}\mathbf{k}\ \mathrm{d}\mathbf{c}_1\ \mathrm{d}\mathbf{c}_2,\end{aligned}$$

and the "source-like" contribution is

$$\chi = \frac{\sigma^2}{2}\int_{\mathbf{c}_{12}\cdot\mathbf{k}>0}(\psi_2' + \psi_1' - \psi_2 - \psi_1)(\mathbf{c}_{12}\cdot\mathbf{k})f^{(2)}(\mathbf{r}-\sigma\mathbf{k}, \mathbf{c}_1; \mathbf{r}, \mathbf{c}_2; t)\ \mathrm{d}\mathbf{k}\ \mathrm{d}\mathbf{c}_1\ \mathrm{d}\mathbf{c}_2.$$

Note that, when ψ is a summational invariant, χ is zero.

3.2.2 Conservation equations

By taking ψ to be m, $m\mathbf{c}$ and $\frac{1}{2}mc^2$ in equation 3.45, after the averaging operation "$<>$", the hydrodynamic conservation equations are deduced in the forms of

$$\frac{\mathrm{d}\rho}{\mathrm{d}t} = -\rho\nabla\cdot\mathbf{v}, \tag{3.47}$$

$$\rho\frac{\mathrm{d}\mathbf{v}}{\mathrm{d}t} = \rho\mathbf{F} - \rho\boldsymbol{\nabla}\cdot\mathsf{P}, \tag{3.48}$$

$$\frac{3}{2}\frac{\mathrm{d}T}{\mathrm{d}t} = -\mathsf{P} : \boldsymbol{\nabla}\mathbf{v} - \boldsymbol{\nabla}\cdot\mathbf{q} - \Gamma. \tag{3.49}$$

The total pressure tensor P is the sum of a kinetic (streaming) part

$$\mathsf{P}_k = \rho\langle\mathbf{C}\mathbf{C}\rangle, \tag{3.50}$$

and a collisional part

$$\mathsf{P}_c = \boldsymbol{\theta}(m\mathbf{C}). \tag{3.51}$$

The fluctuation energy flux $\mathbf{q}$ is the sum of a kinetic part

$$\mathbf{q}_k = \frac{1}{2}\rho\langle C^2\mathbf{C}\rangle, \tag{3.52}$$

and a collisional part

$$\mathbf{q}_c = \boldsymbol{\theta}(\frac{1}{2}mC^2). \tag{3.53}$$

The Γ is the collisional rate of dissipation per unit volume:

$$\Gamma = -\chi(\frac{1}{2}mc^2). \tag{3.54}$$

3.2.3 Constitutive equations

Lun et al. (1984) assumed the single-particle distribution function $f^{(1)}$ is a perturbation to the local equilibrium Maxwellian single-particle velocity distribution function. They also made the Enskog assumption that the pair distribution function

$$f^{(2)}(\mathbf{c}_1, \mathbf{r}_1, \mathbf{c}_2, \mathbf{r}_2; t) = g_0(\sigma) f^{(1)}(\mathbf{c}_1, \mathbf{r} - \sigma\mathbf{k}; t) f^{(1)}(\mathbf{c}_2, \mathbf{r}; t), \tag{3.55}$$

where the equilibrium radial distribution function $g_0(\sigma)$ was taken to be the one given by Carnahan and Starling (1969).

With these treatments, the constitutive equations 3.50 to 3.54 were evaluated. The results were adopted in the multi-fluid model in MFIX as shown in sections 3.1.2.5 and 3.1.2.9.

3.3 Numerical formulation

A finite volume approach is used for the numerical discretization of the equations for multiphase flows. The approach has an advantage to ensure the conservation laws for mass, momentum and energy. The conservative property of finite volume methods is more attractive, especially if a fine grid is too computationally expensive. Thus, even for coarse grids, the solutions hold the integral balances (Patankar, 1980).

3.3.1 A staggered grid

A staggered grid is used for discretizing the partial differential equations. Scalars such as pressure, void fraction, temperature, and mass fraction are stored at the cell centers and the velocity components are stored at the cell surfaces. If all variables such as velocity and pressure are stored on the same grid points, the pressures for two alternate grid points appear in the momentum equations. Thus the zigzag pressure field for a one-dimensional domain and checkerboard pressure field for a two-dimensional domain develop as an acceptable solution. More complex results exist for three-dimensional case and a similar situation appears for the velocity components from continuity equations (Patankar, 1980). If a staggered grid is used, unphysical pressure and velocity fields will not occur since two neighboring grid points appear in the momentum equations.

3.3.2 Discretization

3.3.2.1 Discretization of the governing equations

The discretization of the governing equations is discussed using the transport equation for a scalar variable Φ

$$\frac{\partial}{\partial t}(\varepsilon_m \rho_m \Phi) + \frac{\partial}{\partial x_i}(\varepsilon_m \rho_m v_{mi} \Phi) = \frac{\partial}{\partial x_i}\left(\Gamma_\Phi \frac{\partial \Phi}{\partial x_i}\right) + R_\Phi \tag{3.56}$$

where $m = 0$ denotes the gas phase, $m = 1$ to M denotes the solids phases, Γ_Φ is the diffusion coefficient for Φ and R_Φ is the source term.

Equation (3.56) has all the features of the equations for multiphase flow except the interphase transfer term. The interphase transfer term is important in the multiphase flow equations and is discussed in §3.3.2.2. The equation is integrated over a control volume. Figure 3.1 shows a computational cell and the nomenclature of discretization (Syamlal, 1994). The point P is at the center of the control volume and its neighboring points are referred to as E, W, N, S, T, B. The half-node positions are referred to as e, w, n, s, t, b.

A one-dimensional scalar equation is used as an example for discretization. Convection-

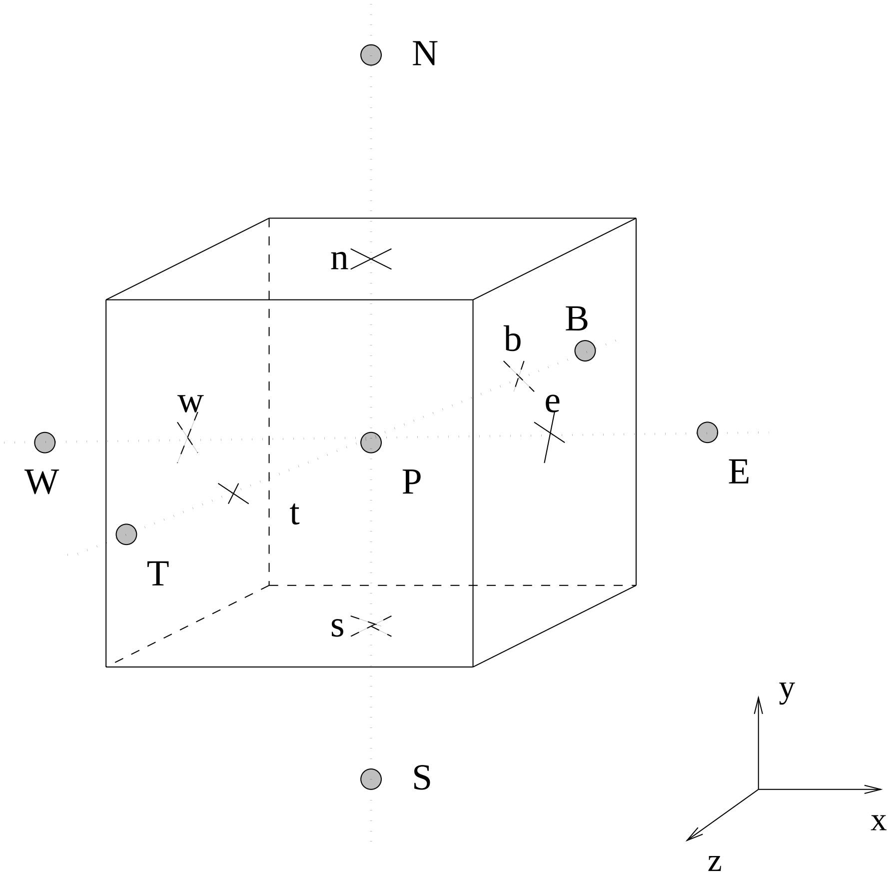

Figure 3.1 Computational cell for the scalar equations

diffusion terms have the following form in the x-direction

$$\rho u \frac{\partial \Phi}{\partial x} - \frac{\partial}{\partial x}\left(\Gamma \frac{\partial \Phi}{\partial x}\right) \tag{3.57}$$

Equation (3.57) is integrated over a control volume dV shown in Fig. 3.2.

$$\int \left[\rho u \frac{\partial \Phi}{\partial x} - \frac{\partial}{\partial x}\left(\Gamma \frac{\partial \Phi}{\partial x}\right)\right] dV = \left[\rho u \Phi_{\mathrm{e}} - \left(\Gamma \frac{\partial \Phi}{\partial x}\right)_{\mathrm{e}}\right] A_{\mathrm{e}} - \left[\rho u \Phi_{w} - \left(\Gamma \frac{\partial \Phi}{\partial x}\right)_{\mathrm{w}}\right] A_{\mathrm{w}} \tag{3.58}$$

With assumption of the piecewise-linear profile between the grids, the diffusive flux, for example, at the east-face becomes

$$\left(\Gamma \frac{\partial \Phi}{\partial x}\right)_{\mathrm{e}} \approx \Gamma_{\mathrm{e}} \frac{(\Phi_{\mathrm{E}} - \Phi_{\mathrm{P}})}{\delta x_{\mathrm{e}}} \tag{3.59}$$

with second order accuracy. Other fluxes have a similar form.

Higher-order schemes for discretizing convection terms are used to prevent numerical diffusion which typically occurs with first-order schemes such as the upwind method. First-order

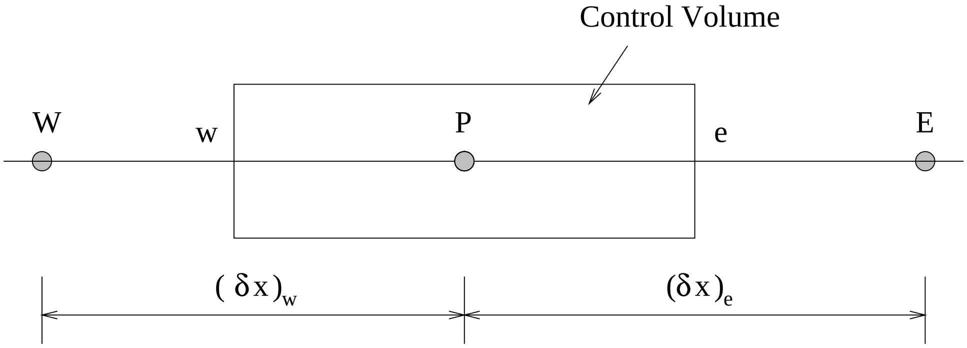

Figure 3.2 Nomenclature for the discretization in the x-direction

schemes lead to pointed bubble shapes in simulations of bubbling fluidized beds (Syamlal, 1998). However, high-order schemes tend to be deficient due to oscillations when discontinuities are encountered. Total variation diminishing (TVD) schemes in the high-order methods can help avoid oscillations. Such schemes use a limiter on the dependent variables (Tannehill et al., 1997). The value of Φ_e at the east face is an example of a TVD scheme and it has the form

$$\Phi_e = \xi_{\mathrm{e}}\Phi_{\mathrm{E}} + \bar{\xi}_{\mathrm{e}}\Phi_{\mathrm{P}} \tag{3.60}$$

where $\bar{\xi}_{\mathrm{e}} = 1 - \xi_{\mathrm{e}}$.

The convection weighting factor ξ_{e} in Eq. (3.60) is calculated from the down-wind factor dwf_{e}, where

if $u_{\mathrm{e}} \geq 0$

$$\Phi_{\mathrm{e}} = dwf_{\mathrm{e}}\Phi_{\mathrm{E}} + (1 - dwf_{\mathrm{e}})\Phi_{\mathrm{P}}$$

$$\xi_{\mathrm{e}} = dwf_{\mathrm{e}}$$

if $u_{\mathrm{e}} < 0$

$$\Phi_{\mathrm{e}} = dwf_{\mathrm{e}}\Phi_{\mathrm{P}} + (1 - dwf_{\mathrm{e}})\Phi_{\mathrm{E}}$$

$$\xi_{\mathrm{e}} = 1 - dwf_{\mathrm{e}}$$

The down-wind factor dwf_{e} is calculated using the superbee method which can be applied to explicit conservative convection and diffusion schemes of any order of accuracy (Leonard, 1991)

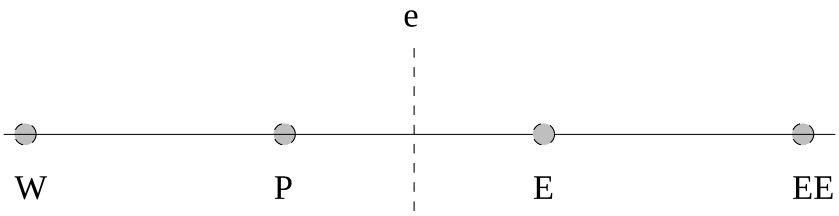

Figure 3.3 Node locations for the TVD scheme

$$dwf_{\mathrm{e}} = \tfrac{1}{2}\max[0, \min(1, 2\theta), \min(2, \theta)]$$

where $\theta = \tilde{\Phi}_{\mathrm{C}}\ /(1 - \tilde{\Phi}_{\mathrm{C}})$ and $\tilde{\Phi}_{\mathrm{C}}$ is

if $u_{\mathrm{e}} \geq 0$

$$\tilde{\Phi}_{\mathrm{C}} = \frac{\Phi_{\mathrm{P}} - \Phi_{\mathrm{W}}}{\Phi_{\mathrm{E}} - \Phi_{\mathrm{W}}}$$

if $u_{\mathrm{e}} < 0$

$$\tilde{\Phi}_{\mathrm{C}} = \frac{\Phi_{\mathrm{E}} - \Phi_{\mathrm{EE}}}{\Phi_{\mathrm{P}} - \Phi_{\mathrm{EE}}}$$

The locations of Φ_{E}, Φ_{W}, Φ_{P} and Φ_{EE} are shown in Fig. 3.3.

The transient term in discretized form is

$$\int \frac{\partial}{\partial t}(\varepsilon_m \rho_m \Phi) dV \approx \left[(\varepsilon_m \rho_m \Phi)_{\mathrm{P}} - (\varepsilon_m \rho_m \Phi)^0_{\mathrm{P}}\right] \frac{\delta V}{\delta t} \tag{3.61}$$

where the superscript 0 indicates previous time step values. Source terms are usually nonlinear and are first linearized as

$$R_\Phi \approx \bar{R}_\Phi - R'_\Phi \Phi_{\mathrm{P}} \tag{3.62}$$

where $\bar{R}_\Phi$ stands for the constant part of R_Φ, while R'_Φ is the coefficient of Φ_{P}. Then, the integration of the source term gives

$$\int R_\Phi dV \approx \bar{R}_\Phi \delta V - R'_\Phi \Phi_{\mathrm{P}} \delta V \tag{3.63}$$

For the stability of the iteration, $R'_\Phi \geq 0$.

All scalar equations may be arranged to get the following linear equation for Φ

$$a_{\mathrm{P}} \Phi_{\mathrm{P}} = \sum_{nb} a_{nb} \Phi_{nb} + b \tag{3.64}$$

where b is a source term. Equation (3.64) should be subtracted by the discretized continuity equation, which is multiplied by Φ (Patankar, 1980).

3.3.2.2 Interphase phase transfer terms

The continuity equations for multiphase flows have a source term for interphase mass transfer $\sum R_{lm}$ and can be discretized as

$$\Phi_{\mathrm{P}} \sum_{l=0}^{\mathrm{M}} R_{lm} = \Phi_{\mathrm{P}} \langle R_{lm} \rangle - \Phi_{\mathrm{P}} \langle -R_{lm} \rangle \tag{3.65}$$

where $l = 0$ indicates gas phase and

$$\langle R \rangle = \begin{cases} 0 & \text{if } R \leq 0 \\ R & \text{if } R > 0 \end{cases}$$

The first term on the right side of Eq. (3.65) is substituted in the source term b of Eq. (3.64). $\langle -R_{lm} \rangle$ in the second term of Eq. (3.65) is substituted in a_P of Eq. (3.64).

The interphase momentum and energy transfer terms $\sum F_{lm}(u_l - u_m)$ and $\sum \gamma_{lm}(T_l - T_m)$ strongly couple the components of velocity and temperature amongst the phases. These terms should be made fully implicit for solving the equations. However, the equations for each velocity component must be solved together, which leads to a nonstandard matrix structure. The partial elimination of interphase coupling (Syamlal, 1998) is used for decoupling the equations.

3.3.2.3 Boundary conditions

Periodic boundary conditions also referred to as cyclic conditions, are specified for the azimuthal direction in cylindrical coordinates. Rotationally (without pressure drop) or translationally (with pressure drop) cyclic boundary conditions may be specified at any of the boundaries.

The free-slip condition is shown schematically in Fig. 3.4 for a cell abut a wall and the ghost cell. The free-slip requirement is

$$(V)_{\text{ghost cell}} = (V)_{\text{near wall cell}}$$

so that the gradient of the velocity at the wall is zero. The boundary condition becomes

$$V(i) - V(i-1) = 0 \tag{3.66}$$

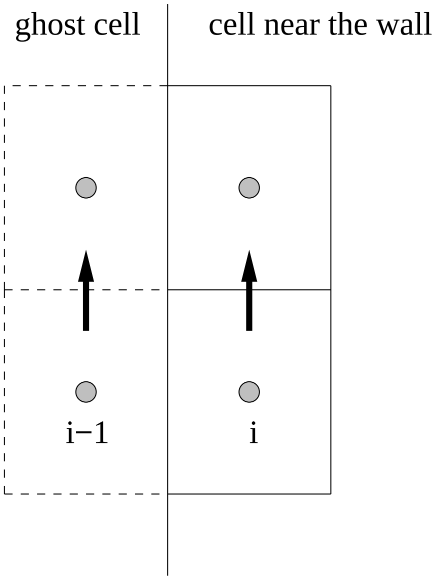

Figure 3.4 Free-slip wall boundary condition

The no-slip condition shown schematically in Fig. 3.5 is set as

$$(V)_{\text{ghost cell}} = -(V)_{\text{near wall cell}}$$

so that the velocity at the wall is zero. The boundary condition becomes

$$V(i) + V(i-1) = 0 \tag{3.67}$$

3.3.3 Modified SIMPLE method

The semi-implicit method for pressure-linked equations (SIMPLE) was developed for the calculation of the single flow field and it has served well (Patankar, 1980). Here, an extension of SIMPLE is used to solve the discretized equations. However, the method requires modifications for multiphase flows due to more field variables and more equations.

The SIMPLE algorithm derives the pressure correction equation to handle the pressure terms in the momentum equations. These pressure terms are not expressed explicitly using an equation. Velocities solved from the momentum equations with the correct pressure satisfy the continuity equations. Similar procedures can be applied to multiphase flows using solids pressure corrections. However, the solids volume fraction correction equation is used instead

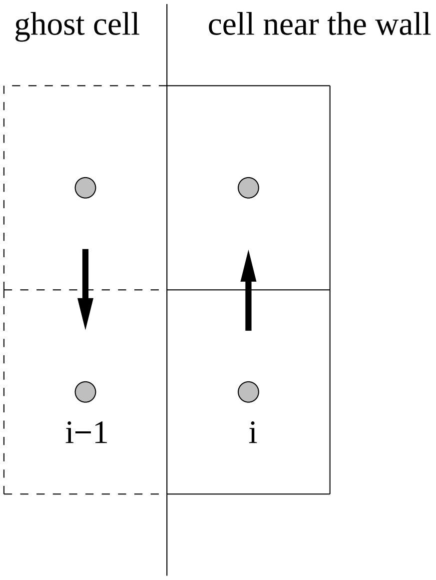

Figure 3.5 No-slip wall boundary condition

of solids pressure correction equation since solids pressure correction equation requires that $\partial P_s / \partial \varepsilon_s$ does not vanish when $\varepsilon_s \to 0$.

In densely packed regions, the solids pressure is an exponentially increasing function of the solids volume fraction. A small increase in the solids volume fraction will cause a large increase in the solids pressure. For numerical stability, solids volume fraction corrections are under-relaxed, where

$$\text{If } (\varepsilon_m)_{\text{new}} > (\varepsilon)_{\text{p}} \text{ and } \varepsilon'_m > 0$$

$$\varepsilon'_m = \omega_{\varepsilon_m} \varepsilon'_m \tag{3.68}$$

and ε_{p} is the volume fraction for the packed region, ω_{ε_m} is an under-relaxation factor, and ε'_m is correction of solids volume fraction with guessed value ε^*_m

$$\varepsilon_m = \varepsilon^*_m + \varepsilon'_m \tag{3.69}$$

Transient simulations are performed since gas solids flows are inherently unstable. Small time steps for a simulation and under-relaxation for iteration are chosen to ensure the numerical stability. Further numerical details and parameters will be discussed with results.

CHAPTER 4. BIOMASS FLOW IN A COMBINE

In this chapter, CFD simulations using the multi-fluid model presented in chapter 3 will be applied to investigate the gas biomass flow process in single-pass multi-component harvesting equipment.

4.1 Introduction

The expression "combine harvester" comes from the fact that in the old days, field binders were used to harvest the grain crop into shocks, which were taken to the stationary threshing machines to separate the grain. These two operations were "combined" in one grain harvester. Today, the time has come to develop the next generation of harvesters that "combine" yet another set of processes into a single harvest machine. The result must be equipment that can harvest multiple crop components (i.e., grain and stems) in a single pass across the field.

As part of this innovation effort, CFD analyses are used to understand the biomass segregation mechanisms in the combines. The segregation of different components of the biomass, i.e., grain, chaff, and stems, occurs mainly in the cleaning shoe unit in a combine (see figure 4.1). There is usually a cleaning loss of 0.1% - 0.5%, which is one of the essential criteria for the work quality of a combine. Understanding the segregation mechanism is very beneficial for the design and operation of a combine.

Segregation is most difficult in the material layer on top of the sieves. Experimental results (see figure 4.2 (CIGR, 1999)) show that with a constant fan speed, losses increase sharply at low throughputs because some grain is blown out, i.e., in the flight phase. On the other end losses increase also at a high throughput because the material layer can not be loosened enough and grain penetration is hampered, i.e., in the bulk phase. Maintaining the fluidization state

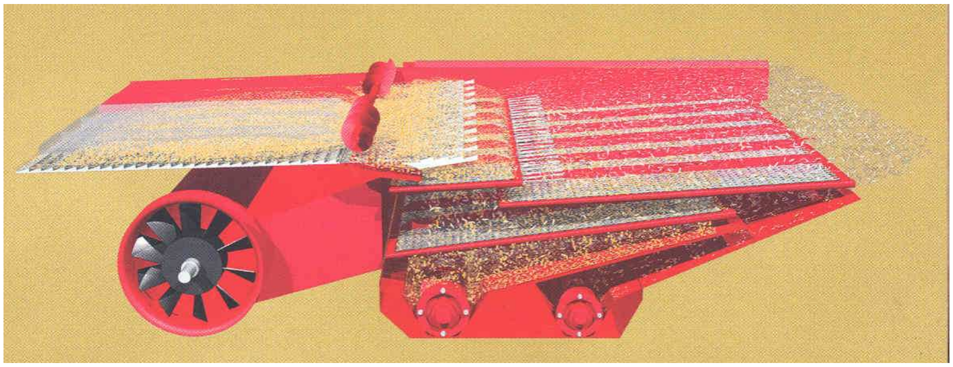

(a) A 3D model

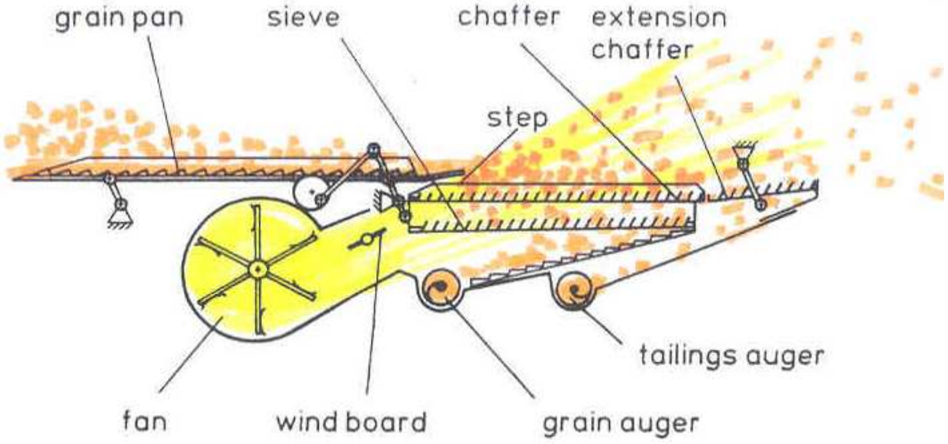

(b) Schematic drawing showing different parts

Figure 4.1 Clean shoe unit in a combine for (a) a 3D model and (b) a 2D schematic.

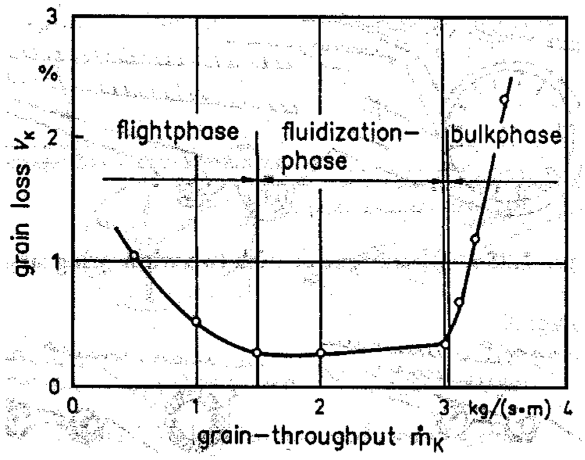

Figure 4.2 Grain loss versus grain throughput at a constant fan speed.

of the material allows good penetration of the grain through the layer and reduces grain loss. Therefore, the research efforts have been focused on studying the fluidization state of grain and chaff and the segregation in a fluidized bed.

4.2 Grain fluidization experiments and simulations

The grain has a non-spherical shape and the fluidization characteristics have not been well studied in the literature, especially the drag force between gas (typically air) and grain in a fluidized state has not been carefully measured. The drag force equation used in MFIX (see equation 3.10) can take non-sphericity into account by using the particle dynamic diameter (the diameter of a sphere having the same surface-to-volume ratio). However, the drag force equation is an empirical correlation according to experimental results of different types of particles (e.g., the experiments by Wen and Yu (1966)), which may deviate from the air-grain drag characteristics. Therefore, grain fluidization experiments were conducted at the Idaho National Laboratory to obtain grain-chaff fluidization characteristics in a controlled study. Grain material properties were also measured, as listed in table 4.1. The experimental procedure is first briefly introduced.

The experiment apparatus is a small-scale air column, whose dimension and instrumentation are shown in figure 4.3. Experiments were performed for a grain bed with initial height of

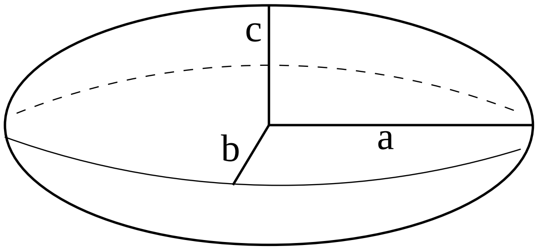

dimensions (cm):	a = 0.32; b = 0.16; c = 0.16.
sphericity:	0.58
material density (g/cm^3):	1.4918

Table 4.1 Grain is approximated as an ellipsoidal with semi-axes of length a, b and c.

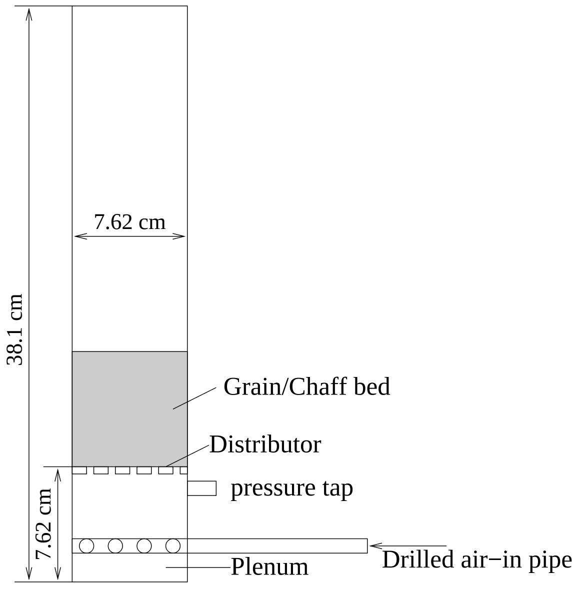

Figure 4.3 Schematic graph of the central plane view of the air column for grain-chaff fluidization experiments.

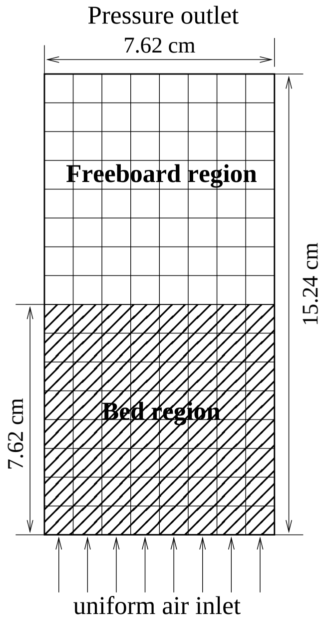

Figure 4.4 2D computational domain with boundary conditions specified for the grain fluidization simulation.

7.62 cm, which was compacted using vibration. Pressure drop across the bed and distributor was measured for different flow rates. The experimental data was used to calibrate the drag force formula used in MFIX simulations.

A two dimensional geometry was used to simulate the grain fluidization experiment with an initial bed height of 7.62 cm. The computational domain is shown in figure 4.4, and the basic computational parameters are listed in table 4.2. The full height of the experimental domain was not simulated because experimental observations showed the bed did not expand higher than 10 cm. A number of cases were run with inlet velocities of $n \times 10.35$ cm/s, where $n = 1, 2 \ldots 10$. The velocities were so chosen that the corresponding flow rates represent uniform increasing increments within the range of the experimental flow rates. The pressure drop across the bed was obtained from the computational results and compared to experimental data, as shown in figure 4.5. To calibrate the drag force formula against the experimental data, the coefficients C and D in equation 3.13 were adjusted to make the computed results agree reasonably with the experimental data. The simulation results obtained from three sets of coefficient values are denoted as “CFD 1”, “CFD 2” and “CFD 3”, respectively in figure 4.5.

Table 4.2 Computational parameters and initial and boundary conditions for the grain fluidization simulation.

Geometry:	
Height of domain	15.24 cm
Width of domain	7.62 cm
Horizontal grid size, Δx	0.95 cm
Vertical grid size, Δy	0.95 cm
Initial conditions:	
Freeboard region	
ε_{g}	1.0
V_{g}	U_{mf}
Bed region	
Initial bed height	7.62 cm
ε_{g}	0.404
V_{g}	$U_{\mathrm{mf}}/\varepsilon_{\mathrm{mf}}$
Boundary conditions:	
Uniform gas inflow	Specified velocity
Specified pressure at outlet	101325.00 Pa
Wall boundary for gas phase	No slip
Wall boundary for solid phase	No slip
Numerical scheme:	
Modified SIMPLE algorithm (see chapter 3)	
Spatial discretization	Second order
Temporal discretization	First order

The values are listed in table 4.3. It can be observed from figure 4.5 that the simulations whose drag force equation using $C = 0.8$ $D = 2.65$ (CFD 1) predict a pressure drop curve that falls in the middle range of the experimental pressure drop curves. Therefore, the drag force equation with the coefficients, $C = 0.8$ $D = 2.65$, is thought to be able to predict reasonably the air-grain interaction in a typical combine clearing shoe setting. This parameter setting was used for simulating biomass flow in a combine.

4.3 Simulation of biomass flow in a combine

CFD simulations for grain and chaff segregation have been performed using a three dimensional computational domain (see figure 4.6) resembling the upper space in the cleaning shoe of a combine. Grain and chaff are modeled as spherical particles with the same dynamic

Table 4.3 The values of coefficient C and D used for the simulations

	C	D
CFD 1:	0.8	2.65
CFD 2	0.7	3.44
CFD 3:	0.64	4.03

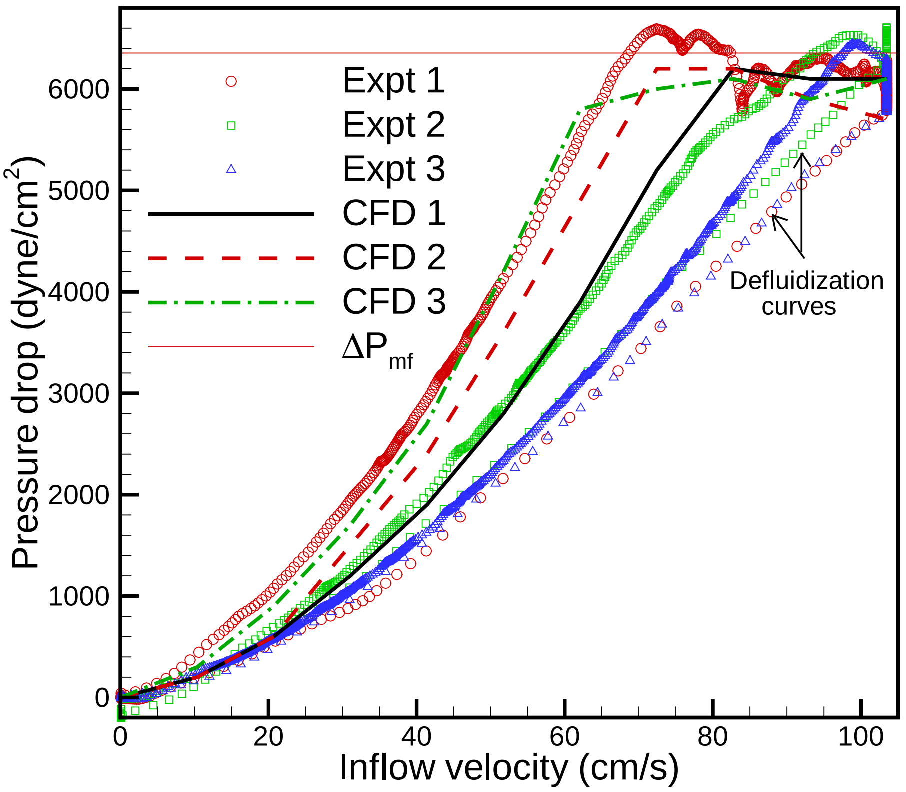

Figure 4.5 Experimental and computational pressure drop across the grain bed. In the legend, “Expt 1”, “Expt 2” and “Expt 3” are the results from the three sets of repeated experiments; “CFD 1”, “CFD 2” and “CFD 3” are the results from CFD simulations with drag force equation using coefficients $C = 0.8$ $D = 2.65$, $C = 0.7$ $D = 3.44$ and $C = 0.64$ $D = 4.03$, respectively. The red horizontal solid line is a guide to eyes for a minimum fluidization pressure, ΔP_{mf}. This pressure is calculated from the balance of pressure force with the bed weight, i.e., $\Delta P_{\mathrm{mf}} = (1 - \varepsilon_{\mathrm{gmf}})(\rho_{\mathrm{s}} - \rho_{\mathrm{g}})gH$, where H is the bed height.

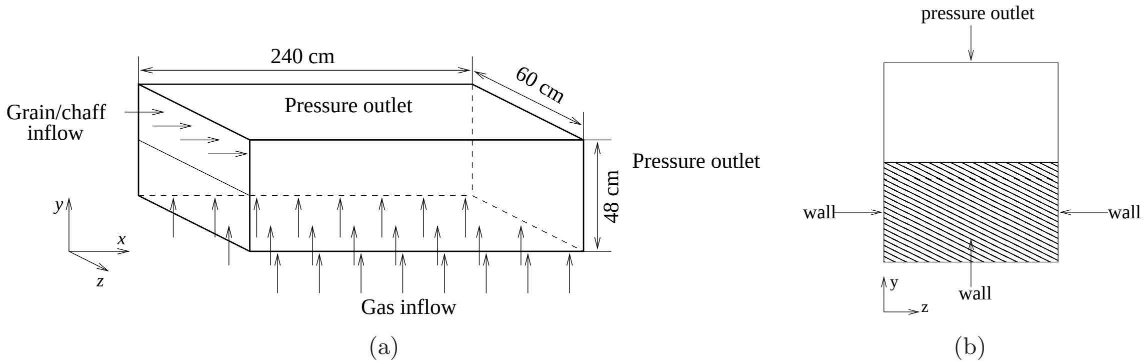

Figure 4.6 Computational domain for the simulation of biomass flow in a combine shown in (a) a 3D view and (b) a view from y-z plane.

diameter. However, the material density of chaff is much less than that of grain; typically grain density is 30 $\sim$ 40 times that of chaff. As seen from figure 4.6, grain and chaff are fed into the domain from the upper part of the left y-z plane, mimicking the process of biomass coming from the grain pan in a combine. Air flows in from the bottom of the domain. The boundary conditions at the right y-z plane and top x-z plane are boundaries where ambient pressure is specified. The rest of the domain boundaries are walls. Extensive simulations with various air inflow velocities, grain and chaff feeding velocities have been performed for engineering application purposes. However, since the results are not qualitatively different for the modeling purpose, only one typical simulation is presented here. The computational parameters are listed in table 4.4.

The biomass flow process was simulated for 10 seconds. The results at the fifth second are presented in figures 4.7–4.11, showing a 3D view of y-z planes and the central x-y plane. Figure 4.7 shows the volume fractions of grain. It is demonstrated that grain is deposited to the bottom of the domain after it drops from the upper inlet. The grain velocity profile shown in figure 4.8 also indicates the trend of grain deposition. The volume fractions of chaff in figure 4.9 show that chaff distributes mostly in the upper part of the domain and is blown out the domain from the top and right outlets. The chaff velocity profile in figure 4.10 shows the chaff blows out of the domain and it largely follows the trajectory of the gas flow as shown in figure 4.11. To quantitatively study the segregation of grain from chaff, the average particle

Table 4.4 Computational parameters and initial and boundary conditions for the simulation of biomass flow in a combine.

Geometry:	
Length of domain x	240 cm
Height of domain y	48 cm
Width of domain z	60 cm
Grid size Δx	6 cm
Grid size Δy	6 cm
Grid size Δz	6 cm
Particle properties:	
Grain diameter	0.23 cm
Grain density	1.4918 g/cm^3
Chaff diameter	0.23 cm
Chaff density	0.0406 g/cm^3
Initial conditions:	
ε_{g}	1.0
V_{g}	85 cm/s
Boundary conditions:	
Uniform gas inflow	$V_{\mathrm{g}} = 85$ cm/s
Grain-chaff inflow	$U = 10$cm/s
Specified pressure at outlet	101325.0 Pa
Grain volume fraction at inlet	0.05
Chaff volume fraction at inlet	0.55
Wall boundary for gas phase	No slip
Wall boundary for solid phase	No slip
Numerical scheme:	
Modified SIMPLE algorithm (see chapter 3)	
Spatial discretization	Second order
Temporal discretization	First order

heights of grain and chaff are shown in figure 4.12. An average particle height is defined as

$$< h_{\mathrm{p}} >= \frac{\sum_i^{N_{\mathrm{part}}} h_i}{N_{\mathrm{part}}} = \frac{\sum_k^{N_{\mathrm{cells}}} \varepsilon_{\mathrm{s},\,k} h_k}{\sum_k^{N_{\mathrm{cells}}} \varepsilon_{\mathrm{s},\,k}}. \tag{4.1}$$

The grain is quickly segregated at the bottom after 1 second while the chaff concentrates at the upper part of the domain. Therefore, the basic segregation phenomena of biomass flow in a combine is captured by the simulation.

4.4 Summary

In this chapter, it has been demonstrated that the grain fluidization characteristics, specifically the pressure drop curve, can be predicted by CFD simulations using the multi-fluid model presented in chapter 3. The coefficients in the drag force model need to be calibrated to reasonably reflect the fluctuations of the pressure drops in repeated experiments. The segregation of grain from chaff in a combine has also been captured by CFD simulations.

However, it should be noted that the real particle properties such as roughness, shape and size distribution are not considered in the current multi-fluid model. The additional complexity caused by these properties are not able to be captured by the model. For example, it was observed in the experiments that a pre-mixed grain and chaff mixture was difficult to be fluidized and segregated. The whole biomass bed tended to be slugging, which could be caused by particle inter-locking and friction. The inter-locking phenomena may happen in a real combine but cannot be captured by the current model.

In order to derive models that can more accurately predict realistic multiphase flows, the physics at particle scale is studied using the kinetic theory for granular flow, molecular dynamics and a hybrid method. The studies are presented in the following chapters.

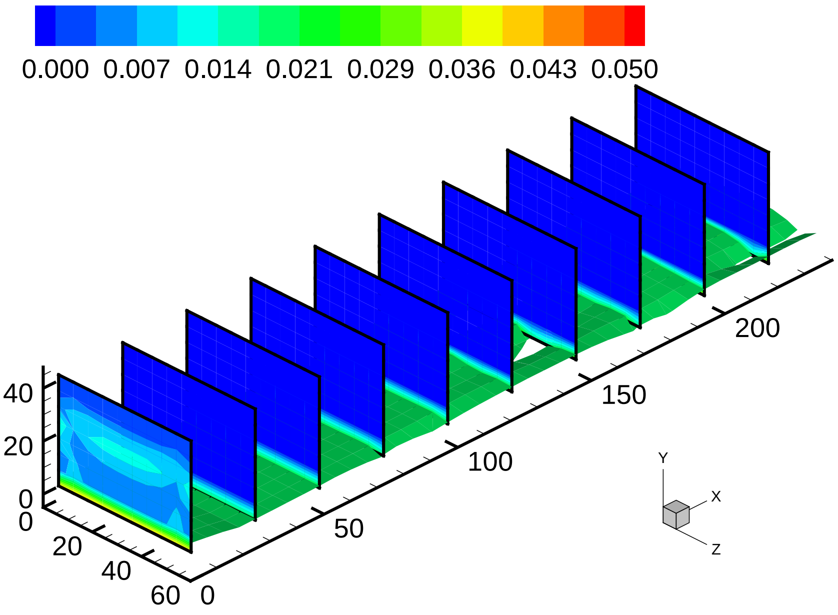

(a)

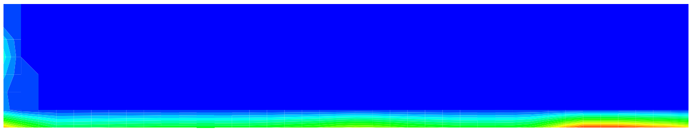

(b)

Figure 4.7 Grain volume fraction distribution shown in (a) the y-z planes and an iso-surface at volume fraction 0.02 and (b) the middle x-y plane. The contour levels indicate the values of volume fractions. The length unit is cm.

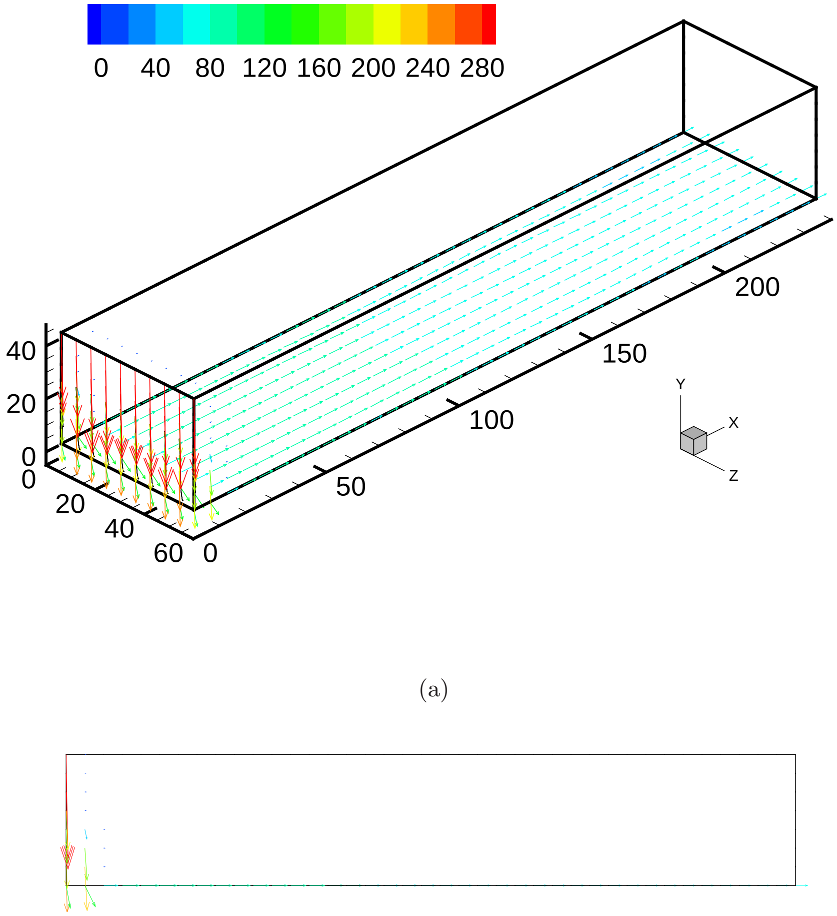

(a)

(b)

Figure 4.8 Grain velocity vectors with their lengths and colors indicating the velocity magnitudes shown in (a) a three dimensional view and (b) a middle x-y plane. The velocity unit is cm/s. The length unit is cm.

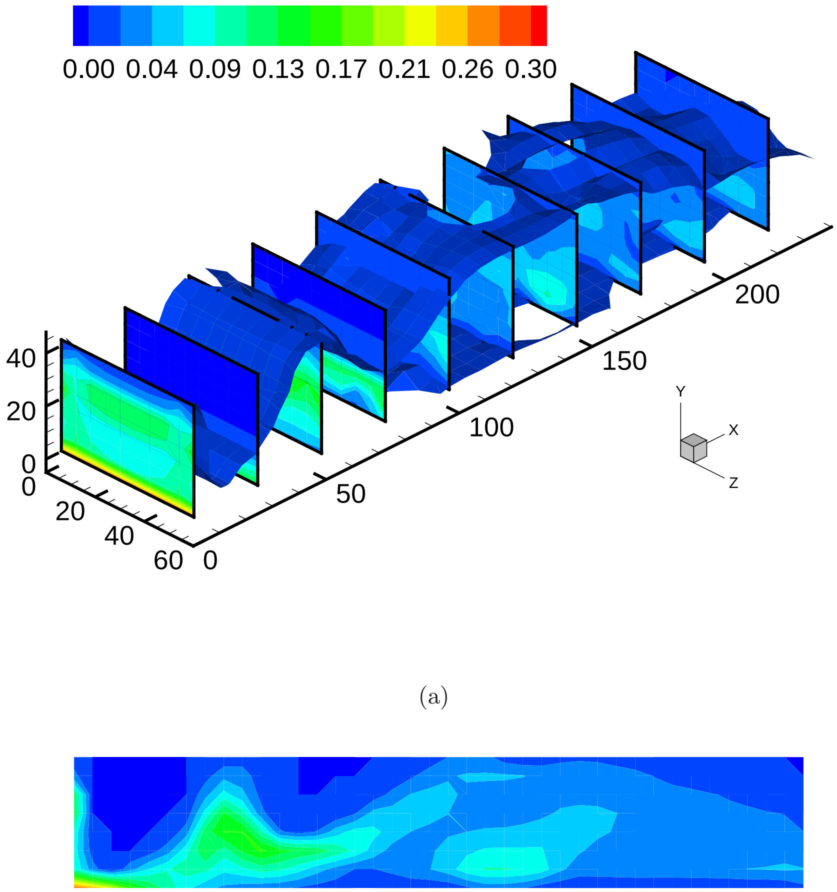

(a)

(b)

Figure 4.9 Chaff volume fraction distribution shown in (a) the y-z planes and an iso-surface at volume fraction 0.02 and (b) the middle x-y plane. The contour levels indicate the values of volume fractions. The length unit is cm.

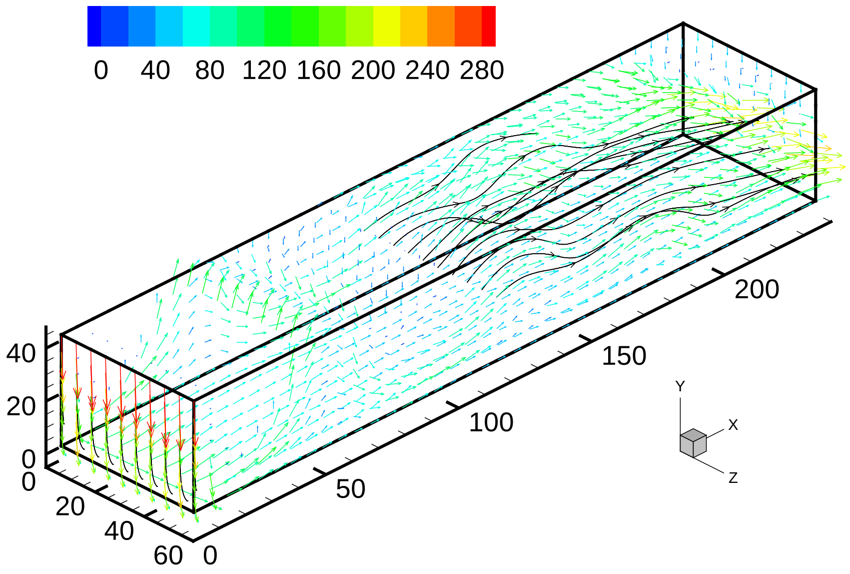

(a)

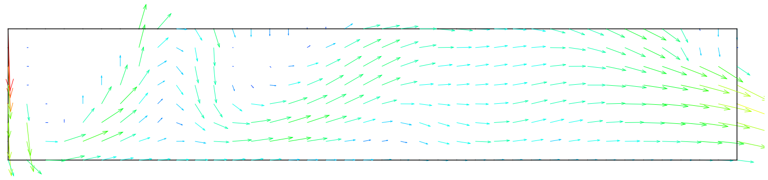

(b)

Figure 4.10 Chaff velocity vectors with their lengths and colors indicating the velocity magnitudes in (a) a three dimensional view and (b) a middle x-y plane. The black curves are streamlines originated at the inlet and middle y-z planes, respectively. The velocity unit is cm/s. The length unit is cm.

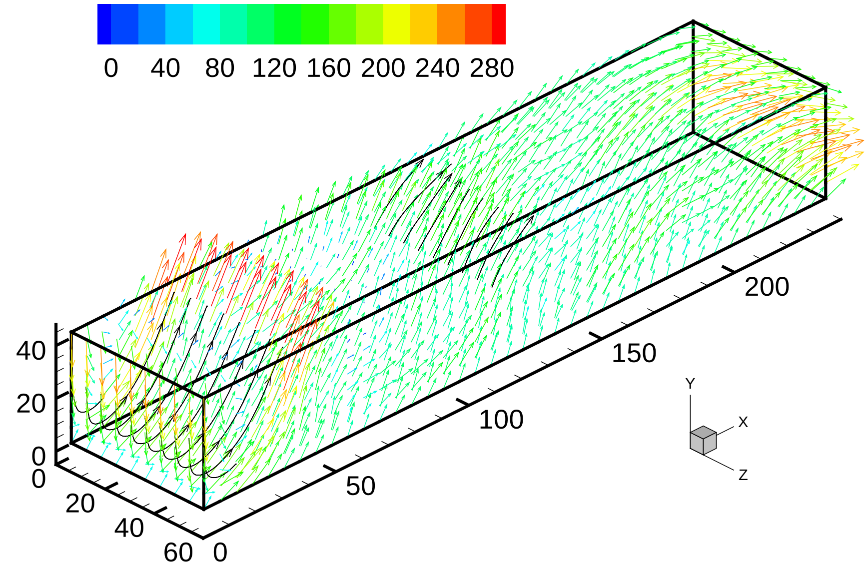

(a)

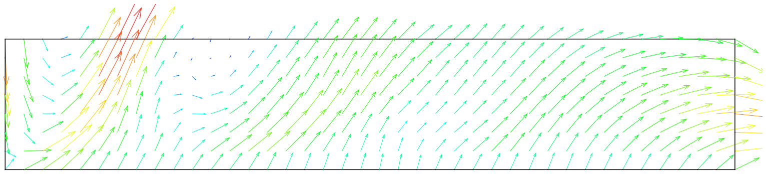

(b)

Figure 4.11 Gas velocity vectors with their lengths and colors indicating the velocity magnitudes in (a) a three dimensional view and (b) a middle x-y plane.The black curves are streamlines originated at the inlet and middle y-z planes, respectively. The velocity unit is cm/s. The length unit is cm.

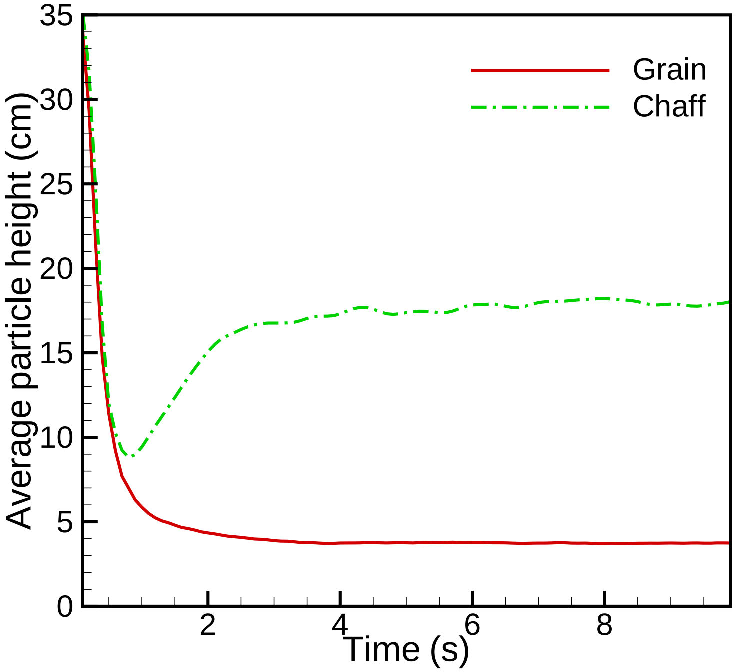

Figure 4.12 Average particle heights of grain and chaff as functions of time.

CHAPTER 5. HYDRODYNAMIC MODELING OF PARTICLE ROTATION FOR SEGREGATION IN BUBBLING GAS FLUIDIZED BEDS

A paper published in *Chemical Engineering Science* [1]

Jin Sun and Francine Battaglia

Abstract

A multi-fluid Eulerian model has been improved by incorporating particle rotation using kinetic theory for rapid granular flow of slightly frictional spheres. A simplified model was implemented without changing the current kinetic theory framework by introducing an effective coefficient of restitution to account for additional energy dissipation due to frictional collisions. Simulations without and with particle rotation were performed to study the bubble dynamics and bed expansion in a monodispersed bubbling gas-fluidized bed and the segregation phenomena in a bidispersed bubbling gas-fluidized bed. Results were compared between simulations without and with particle rotation and with corresponding experimental results. It was found that the multi-fluid model with particle rotation better captures the bubble dynamics and time-averaged bed behavior. The model predictions of segregation percentages agreed with experimental data in the fluidization regime where kinetic theory is valid to describe segregation and mixing.

---

[1] *Chemical Engineering Science*, 61(5):1470–1479, 2006.

Nomenclature

$\vec{c}$	Instantaneous particle velocity
$\vec{C}$	Translational particle velocity fluctuation
d	Particle diameter
e	Coefficient of normal restitution
F	Drag coefficient
$\vec{g}$	Gravity
g_0	Equilibrium radial distribution function at contact
I	Moment of inertia of a particle
$\vec{I}$	Interphase momentum transfer
J_{coll}	Rate of dissipation of translational fluctuation kinetic energy due to particle collisions
J_{vis}	Rate of dissipation of translational fluctuation kinetic energy due to interstitial gas viscous damping
m_p	Mass of a particle
$\vec{n}$	Unit normal vector from a boundary to particles
R	Rate of formation
Re	Reynolds number
S_{d}	Segregation degree
S_{p}	Segregation percentage
$\overline{\overline{S}}$	Stress tensor
U	Fuidization velocity
$\vec{v}$	Velocity for gas and solids phases
x	Mass fraction

Greek letters

β_0	Coefficient of tangential restitution
Φ	Particle shape factor

ϕ'	Specularity coefficient for wall
Γ	Rate of dissipation of rotational fluctuation kinetic energy
γ_{slip}	Production of translational fluctuation kinetic energy due to gas-particle slip
μ	Coefficient of friction
$\vec{\omega}$	Particle angular velocity
$\vec{\Omega}$	Fluctuation in particle angular velocity
ε	Volume fraction
ρ	Density
θ_{t}	Translational granular temperature
θ_{r}	Rotational granular temperature

Superscripts/Subscripts

eff	Effective parameters
g	Gas phase
coll	Collision
l	l^{th}solid phase
m	m^{th}solid phase
M	Number of phases
mf	Minimum fluidization
max	Maximum value
N	Number of species
p	Particle
r	Rotational
s	Solid phase
t	Translational
w	Wall boundary

5.1 Introduction

It is not uncommon to encounter industrial applications of dense gas-solid fluidized beds for mixtures of particles with different physical properties such as size and density. Examples of industrial applications are coal gasification, fluidized bed polymerization and granulation. In such systems, the mixing of solids is often incomplete and a vertically non-uniform blend of particles forms. For example, in a system consisting of particles of equal density but different size, the bigger particles tend to reside at the bottom of the bed if the inlet velocity does not exceed the minimum fluidization velocity of the bigger particles. The bigger particles in this case are commonly referred to as jetsam. Smaller particles will float and reside at the top of the bed, commonly referred to as floatsam (Hoffmann et al., 1993). Knowledge of the degree and rate of this kind of segregation phenomena is very important for several reasons. In many industrial fluidized beds, good mixing is required for uniform product quality or to avoid defluidization. In other applications, however, the tendency for segregation is utilized such as the case for continuous removal of a product.

Segregation phenomena in gas-fluidized beds have been extensively studied. Hoffmann et al. (1993) experimentally studied systems consisting of particles of equal density but different sizes. Wu and Baeyens (1998) also examined the behavior of equal density systems of large and small particles. They showed segregation patterns where larger particles migrated to the bottom, whereas the smaller particles concentrated at the top section of the bed. Nienow and Naimer (1980) performed experiments on systems consisting of particles of equal size but different density. These studies indicate that mixing and segregation of bubbling fluidized beds are largely determined by the bubble dynamics. Bubbles act as a vehicle for both mixing and segregation. Goldschmidt et al. (2003) measured bed expansion and segregation dynamics with particles of well-known properties (size, shape, density and collision properties) in dense gas-fluidized bed using digital image analysis. An advantage of the experimental setup is that it can be easily simulated numerically using robust hydrodynamic models.

Numerical simulations of the hydrodynamics of gas-fluidized beds have been employed as a useful tool to study segregation phenomena. Recently, Hoomans et al. (2000) showed bubble dynamics in dense gas-fluidized beds strongly depend on the amount of energy dissipated by particle-particle collisions using hard sphere discrete particle models. Goldschmidt et al. (Goldschmidt et al., 2001a,b; Goldschmidt, 2001) used Eulerian models to study the segregation phenomena in bubbling gas-fluidized beds. The number of particles specified using a discrete particle model (typically less than 10^6) was an order of magnitude lower than that encountered in most industrial fluidized beds (Goldschmidt, 2001).

In order to describe the segregation phenomena in large industrial-scale fluidized bed reactors, a multi-fluid Eulerian model is better than a Lagrangian model due to the computational expense to simulate large numbers of particles. In this kind of model both gas and particulate phases are described as interpenetrating continua and the kinetic theory of granular flow (KTGF) is used to provide constitutive closures for particulate phases. Although Eulerian models have been developed and used to study bed hydrodynamics and segregation (Goldschmidt et al., 2001a,b; Goldschmidt, 2001; Enwald et al., 1996; Gidaspow, 1994), these models can not describe quantitatively segregation rates in polydispersed fluidized beds. For example, higher segregation rates were predicted by numerical simulations compared with experiments, as reported by Goldschmidt et al. (2001b). It is speculated that KTGF, which is limited to slightly inelastic spherical particles and does not allow for particle rotation, underestimates the amount of energy dissipated in the frictional inelastic collisions for common particles. Consequently the bubble intensity is underestimated. Further studies (Goldschmidt, 2001) showed that the absence of rotation and subsequent energy losses is a deficiency of the multi-fluid model in contrast to discrete particle models which provide closer resemblance to experimental results. Therefore, it should be of interest to incorporate particle rotation into the hydrodynamic model and analyze the effects on segregation in gas-fluidized beds.

In principle, particle rotation can be incorporated in a multi-fluid model by addition of conservation equations for angular momentum and rotational fluctuation kinetic energy. Jenkins and Richman (1985) and Lun and Savage (1987) derived models for rough disks and spheres, respectively. The kinetic energies associated with fluctuations in both translational velocity and spin were considered. The addition of conservation equations for angular momentum and rotational fluctuation kinetic energy greatly increase the complexity of the kinetic theory. Since the most important influence of particle rotation on bed dynamics is the energy dissipation, a simpler approach which only modifies the granular energy dissipation seems promising.

In this work, particle rotation is incorporated into a multi-fluid Eulerian model using a simple kinetic theory for rapid granular flow of slightly frictional spheres (Jenkins and Zhang, 2002). The improved multi-fluid Eulerian model is used to study the size-driven segregation in a bidispersed gas-solid fluidized bed. Results from the particle rotation model are compared with numerical simulations without particle rotation and with corresponding experimental results.

5.2 Methodology

5.2.1 Basic multi-fluid model

A Fortran code, Multiphase Flow with Interphase eXchanges (MFIX), is used for all simulations in this work. The multi-fluid Eulerian model in MFIX divides the particle mixture into a discrete number of phases, each of which can have different physical properties and can be mathematically described as interpenetrating continua. The governing equations for the multi-fluid model are as follows (Syamlal et al., 1993):

Continuity equation for gas phase

$$\frac{\partial}{\partial t}(\varepsilon_{\mathrm{g}}\rho_{\mathrm{g}}) + \nabla\cdot(\varepsilon_{\mathrm{g}}\rho_{\mathrm{g}}\vec{v}_{\mathrm{g}}) = \sum_{n=1}^{N_{\mathrm{g}}} R_{\mathrm{g}n} \quad . \tag{5.1}$$

Continuity equation for m^{th} solid phase

$$\frac{\partial}{\partial t}(\varepsilon_{sm}\rho_{sm}) + \nabla\cdot(\varepsilon_{sm}\rho_{sm}\vec{v}_{sm}) = \sum_{n=1}^{N_{sm}} R_{smn} \quad . \tag{5.2}$$

Momentum equation for gas-phase

$$\frac{\partial}{\partial t}(\varepsilon_{\mathrm{g}}\rho_{\mathrm{g}}\vec{v}_{\mathrm{g}}) + \nabla\cdot(\varepsilon_{\mathrm{g}}\rho_{\mathrm{g}}\vec{v}_{\mathrm{g}}\vec{v}_{\mathrm{g}}) = \nabla\cdot\overline{\overline{S}}_{\mathrm{g}} + \varepsilon_{\mathrm{g}}\rho_{\mathrm{g}}\vec{\mathrm{g}} - \sum_{m=1}^{M}\vec{I}_{\mathrm{g}m} \quad . \tag{5.3}$$

Momentum equation for m^{th} solid-phase

$$\frac{\partial}{\partial t}(\varepsilon_{sm}\rho_{\mathrm{s}m}\vec{v}_{\mathrm{s}m}) + \nabla\cdot(\varepsilon_{sm}\rho_{\mathrm{s}m}\vec{v}_{\mathrm{s}m}\vec{v}_{\mathrm{s}m}) = \\ \nabla\cdot\overline{\overline{S}}_{\mathrm{s}m} + \varepsilon_{sm}\rho_{\mathrm{s}m}\vec{g} + \vec{I}_{\mathrm{g}m} - \sum_{\substack{l=1\\ l\neq m}}^{M}\vec{I}_{ml} \quad . \tag{5.4}$$

Translational granular temperature equation (Agrawal et al., 2001)

$$\frac{3}{2}\left[\frac{\partial}{\partial t}(\varepsilon_{sm}\rho_{\mathrm{s}m}\theta_{\mathrm{s}m,\mathrm{t}}) + \nabla\cdot(\varepsilon_{sm}\rho_{\mathrm{s}m}\theta_{\mathrm{s}m,\mathrm{t}}\vec{v}_{\mathrm{s}m})\right] = \\ -\nabla\cdot\vec{q}_{\mathrm{s}m} - \overline{\overline{S}}_{\mathrm{s}m} : \nabla\vec{v}_{\mathrm{s}m} + \gamma_{\mathrm{s}m,\mathrm{slip}} - J_{\mathrm{s}m,\mathrm{coll}} - J_{\mathrm{s}m,\mathrm{vis}} \quad , \tag{5.5}$$

where the translational granular temperature is defined as

$$\theta_{\mathrm{s}m,\mathrm{t}} = \frac{1}{3} < C_{\mathrm{s}m}^2 > . \tag{5.6}$$

The fluctuation in the particle translational velocity shown in Eqn. 5.6 is defined as $\vec{C}_{\mathrm{s}m} = \vec{c}_{\mathrm{s}m} - < \vec{c}_{\mathrm{s}m} >$, where $\vec{c}_{\mathrm{s}m}$ is the instantaneous translational velocity and <> is the ensemble average.

Constitutive equations for the gas phase stress tensor ($\overline{\overline{S}}_{\mathrm{g}}$) and gas-solid momentum transfer ($\vec{I}_{\mathrm{g}m}$) can be found in Syamlal et al. (1993). The solid-solid interaction term ($\vec{I}_{\mathrm{s}m}$) was derived by Syamlal (1987a) using a simple model from kinetic theory, in which singlet velocity distribution functions were expressed as Dirac delta functions. Thus, granular temperature terms do not appear in the solid-solid interaction. The constitutive equations for multi-component solid mixtures are derived from granular flow theory. There are two distinct flow regimes for granular flow: a viscous or rapidly shearing regime in which stresses arise due to collisional or translational momentum transfer, and a plastic or slowly shearing regime in which stresses arise due to Coulomb friction between particles in enduring contact (Syamlal et al., 1993). The rapid granular flow regime is of main interest in this research. The constitutive equations used in MFIX for this regime were derived based on kinetic theory of granular flow, derived by Lun et al. (1984) and modified by Ma and Ahmadi (1988) to take into account of the effects of interstitial gas on particle phase viscosity and thermal diffusivity.

The constitutive relationship and boundary conditions, which will be modified in the particle rotation model, are shown in the following. The rate of dissipation of translational fluctuation kinetic energy due to particle collisions is defined as:

$$J_{sm,\mathrm{coll}} = \frac{12}{\sqrt{\pi}}(1-e_{\mathrm{sm}}^2)\frac{\rho_{sm}\varepsilon_{\mathrm{sm}}^2}{d_m} g_{0mm}\theta_{sm,\mathrm{t}}^{3/2} \quad . \tag{5.7}$$

The partial slip boundary conditions for particle-wall interactions, proposed by Johnson and Jackson (1987), are employed. The boundary condition for the slip velocity is:

$$\vec{v}_{sm,\mathrm{slip}} \cdot \overline{\overline{S}}_{sm} \cdot \vec{n} + \frac{\sqrt{3}\pi}{6\varepsilon_{sm,\,\max}}\phi' \rho_{sm}\varepsilon_{sm} g_{0mm}\theta_{\mathrm{sm,t}}^{1/2}|\vec{v}_{sm,\mathrm{slip}}|^2 = 0 \quad . \tag{5.8}$$

The boundary condition for the flux of translational fluctuation energy to the wall is:

$$-\vec{n}\cdot\vec{q}_{sm} = \frac{\sqrt{3}\pi}{4\varepsilon_{sm,\,\max}}(1-e_{\mathrm{w}}^2)\varepsilon_{sm}\rho_{sm} g_{0mm}\theta_{sm,\mathrm{t}}^{3/2} + \vec{v}_{sm,\mathrm{slip}} \cdot \overline{\overline{S}}_{sm} \cdot \vec{n} \quad , \tag{5.9}$$

where

$$\vec{v}_{sm,\mathrm{slip}} = \vec{v}_{\mathrm{sm}} - \vec{v}_{\mathrm{w}} \quad . \tag{5.10}$$

5.2.2 Particle rotation model

Most common particles are frictional as well as inelastic. As a result, particles can rotate with angular velocity $\vec{\omega}$ and translate under rapid rates of deformation. Lun et al. (Lun and Savage, 1987; Lun, 1991) developed a kinetic theory for a system of inelastic, rough spheres to study the effects of particle surface friction and rotational inertia. Jenkins and Richman (1985) used Grad's method of moments to derive conservation laws and constitutive relations for planar flows of a dense gas consisting of identical, rough, inelastic, circular disks. In these theories (Lun and Savage, 1987; Lun, 1991; Jenkins and Richman, 1985), two granular temperatures are involved. The first is translational granular temperature θ_{t}, which measures the energy associated with the translational velocity fluctuations, as defined in Eqn. 5.6. The second is rotational granular temperature θ_{r}, which measures the energy associated with the angular velocity fluctuations, defined as $\theta_{\mathrm{r}} = \frac{1}{3m_p} I < \Omega^2 >$, where I is moment of inertia, $\vec{\Omega} = \vec{\omega} - < \vec{\omega} >$ is the angular velocity fluctuation and m_p is the mass of a particle. Additional conservation equations for angular momentum and rotational granular temperature are required, which greatly increase the complexity of the kinetic theory and is often difficult to apply to general flows. Since the most important influence of particle rotation on bed dynamics is the additional energy dissipation due to frictional collisions, a simpler approach which only modifies the translational fluctuation energy dissipation seems promising.

A simple model from kinetic theory for rapid flow of identical, slightly frictional, nearly elastic spheres (Jenkins and Zhang, 2002) was adapted to incorporate particle rotation into the multi-fluid model presented in the previous section. In this model, the frictional collision is described by a normal restitution coefficient e, a friction coefficient μ and a tangential restitution coefficient β_0. For slightly frictional spheres, the distribution of translational velocities does not differ too much from that for smooth spheres. The balance equations for the moments associated with the rotational degree of freedom are satisfied in an approximate way by ignoring unsteady and inhomogeneous terms. Thus, the conservation of angular momentum reduces to the requirement that the mean spin of spheres be equal to half the vorticity of their mean velocity. The conservation of rotational fluctuation kinetic energy is approximately satisfied by requiring that the net rate of energy production for the angular velocity fluctuations is zero. The influence of friction on the collisional transfer of linear momentum and translational energy is negligible, and the stress and the translational energy flux are identical to those for smooth, elastic spheres. Only the dissipation rates for translational and rotational fluctuation energy, $J_{sm,\mathrm{coll}}$ and Γ_{sm} respectively, are influenced by friction. The approximations of $J_{sm,\mathrm{coll}}$ and Γ_{sm} are (Jenkins and Zhang, 2002):

$$J_{sm,\mathrm{coll}} = \frac{12}{\sqrt{\pi}} \frac{\rho_\mathrm{s} \varepsilon_{sm}^2}{d_m} g_{0mm} \theta_{sm,\mathrm{t}}^{3/2} \left[2(1-e_{sm}) + a_1 - a_2 \frac{\theta_{sm,\mathrm{r}}}{\theta_{sm,\mathrm{t}}} \right] \quad , \tag{5.11}$$

where

$$a_1 \equiv \frac{\mu}{\mu_0} \left[\pi \mu_0 \left(1 - \frac{2}{\pi} \arctan \mu_0 \right) + \frac{2\mu_0^2}{1+\mu_0^2} \left(1 - 2\frac{\mu}{\mu_0} \right) \right] \quad , \tag{5.12}$$

$$a_2 \equiv \frac{5\mu}{\mu_0} \left[\frac{\pi}{2} \mu_0 \left(1 - \frac{2}{\pi} \arctan \mu_0 \right) - \frac{\mu_0^4}{(1+\mu_0^2)^2} \right] \quad , \tag{5.13}$$

and

$$\Gamma_{sm} = -\frac{120}{\sqrt{\pi}} \frac{\rho_\mathrm{s} \varepsilon_{sm}^2}{d_{\mathrm{p}m}} g_{0mm} \theta_{sm,\mathrm{t}}^{3/2} \left[b_1 - b_2 \frac{\theta_{sm,\mathrm{r}}}{\theta_{sm,\mathrm{t}}} \right] \quad , \tag{5.14}$$

where

$$b_1 \equiv \left(\frac{\mu}{\mu_0}\right)^2 \frac{\mu_0^2}{1+\mu_0^2} \tag{5.15}$$

$$b_2 \equiv \frac{\mu}{2\mu_0}\left[\frac{\pi}{2}\mu_0\left(1-\frac{2}{\pi}\arctan\mu_0\right)+\frac{\mu_0^2}{1+\mu_0^2}\right] \tag{5.16}$$

$$\mu_0 \equiv \frac{7}{2}\mu\frac{1+e_{sm}}{1+\beta_0} \quad . \tag{5.17}$$

The conservation equation for rotational granular energy is approximately satisfied by setting the rate of dissipation of rotational granular energy equal to zero. Then, the rotational granular temperature $\theta_{sm,\mathrm{r}}$ is determined in terms of the translational granular temperature $\theta_{sm,\mathrm{t}}$:

$$\frac{\theta_{sm,\mathrm{r}}}{\theta_{sm,\mathrm{t}}} = \frac{b_1}{b_2} \quad . \tag{5.18}$$

Substituting Eqn. 5.18 to Eqn. 5.11 and comparing the result to Eqn. 5.7, we can define an effective coefficient of restitution $e_{sm,\mathrm{eff}}$ (assuming that $(1+e_{sm}) \approx 2$, i.e. nearly elastic):

$$e_{sm,\mathrm{eff}} = e_{sm} - \frac{1}{2}a_1 + \frac{a_2 b_1}{2b_2}. \tag{5.19}$$

Thus, the kinetic theory for slightly frictional, nearly elastic spheres has the same structure as that for frictionless spheres, i.e., only conservation of mass, mean translational velocity and translational temperature need to be considered. The modification to the multi-fluid model is through the introduction of an effective coefficient of restitution that incorporates the additional dissipation due to frictional interactions in the rate of dissipation of translational fluctuation energy.

The only equations that need to be modified are the dissipation terms in the translational granular temperature equation and the partial slip boundary condition for the flux of translational fluctuation energy to the wall. The corresponding equations, 5.7 and 5.9 become:

$$J_{sm,\mathrm{coll}} = \frac{12}{\sqrt{\pi}}(1+e_{\mathrm{sm}})(1-e_{\mathrm{sm,eff}})\frac{\rho_{\mathrm{sm}}\varepsilon_{\mathrm{sm}}^2}{d_m} g_{0mm}\theta_{\mathrm{sm,t}}^{3/2} \quad , \tag{5.20}$$

and

$$-\vec{n}\cdot\vec{q}_{\mathrm{sm}} = \frac{\sqrt{3}\pi}{4\varepsilon_{\mathrm{s,\,max}}}(1+e_{\mathrm{w}})(1-e_{\mathrm{w,eff}})\varepsilon_{sm}\rho_{sm}g_{0mm}\theta_{\mathrm{sm,t}}^{3/2} + \vec{v}_{\mathrm{sm,slip}}\cdot\overline{\overline{S}}_{sm}\cdot\vec{n} \quad . \tag{5.21}$$

5.2.3 Numerical formulation

MFIX uses a finite volume approach with a staggered grid for the discretization of the governing equations to reduce numerical instabilities (Syamlal, 1998). Scalars such as pressure and volume fraction are stored at the cell centers and the velocity components are stored at cell surfaces. A second-order discretization is used for spatial derivatives and first-order discretization for temporal derivatives. A modified SIMPLE algorithm with partial elimination of interphase coupling is employed to solve the discretized equations (Syamlal, 1998).

5.3 Computational cases and results

The effects of particle rotation on the hydrodynamics of segregation in a gas-solid fluidized bed is examined. Previous experiments by Goldschmidt et al. (Goldschmidt, 2001; Goldschmidt et al., 2003) are used to benchmark the numerical simulations using the multi-fluid model with and without particle rotation. Goldschmidt et al. examined monodispersed (Goldschmidt, 2001) and bidispersed (Goldschmidt et al., 2003) gas-solid fluidized systems using digital image analysis techniques. The rectangular geometry of the experimental setup was pseudo-two-dimensional due to the small chamber depth relative to the height and width (see Tab. 5.1). The thin depth suppresses particle motion in that direction in the experiments and the effect of the front and back walls to the bed was not considered of interest (Goldschmidt, 2001).

A two-dimensional computational domain was used in the fluidized bed simulations, which is a physical reliable model of the pseudo-two-dimensional experiment. The dimensions are shown in Fig. 5.1 for a Cartesian coordinate system. The domain and grid size are specified in Tab. 5.2. Although the experiment used a system with a domain height of 70 cm, the computational domain height was reduced to 45 cm to avoid computationally expensive simulations yet ensuring the bed dynamics are physical. It was evident from the experiments that the bed did not expand above 30 cm. The particle properties and collision parameters cited in the experiments (see Tab. 5.1) are used as input parameters for the numerical work to test and validate the particle rotation model. The effective coefficients of restitution for these two kinds of particles are calculated using Eqn. 5.19 and the values are shown in Tab. 5.1.

Table 5.1 Geometry of the experimental system and particle properties.

height		70 cm
width		15 cm
depth		1.5 cm
	Small particles	Large particles
d_p	1.52 ± 0.04 mm	2.49 ± 0.02 mm
ρ_p	2523 ± 6 kg/m^3	2526 ± 6 kg/m^3
Φ_p	~ 1	~ 1
U_mf	92 cm/s	128 cm/s
Particle-particle collision parameters		
e_{sm}	0.97 ± 0.01	0.97 ± 0.01
μ	0.15 ± 0.015	0.10 ± 0.01
β_0	0.33 ± 0.05	0.33 ± 0.05
$e_{m,\mathrm{eff}}$	0.83	0.86
Particle-wall collision parameters		
e_w	0.97 ± 0.01	0.97 ± 0.01
μ_w	0.10 ± 0.015	0.09 ± 0.01
$\beta_{0,\mathrm{w}}$	0.33 ± 0.05	0.33 ± 0.05
$e_{\mathrm{w,eff}}$	0.86	0.87

A spatial grid refinement study was performed to determine the grid sensitivity of the computational results. Three successively halved grids, i.e., coarse, medium and fine grids, were used. The study showed that the grid refinement from coarse to medium grid size improved the results by a relatively large degree, while refinement from medium to fine grid size had little influence on time-averaged results. A Richardson extrapolation based on the medium and fine grids was used to provide error estimates. The time-averaged voidage for medium grid had an average error of 1.4 % and a maximum error of 3.7 %, compared to the Richardson extrapolation results. As a conclusion from the grid refinement study, the medium grid size was used for the remaining simulations as cited in Tab. 5.2. In addition, the current grid size is of the order of a few particle diameters, which is thought to adequately resolve the meso-scale structures of gas-solid flows (Agrawal et al., 2001). Computational results were not sensitive to time step change since an adaptive time stepping algorithm was used. For all

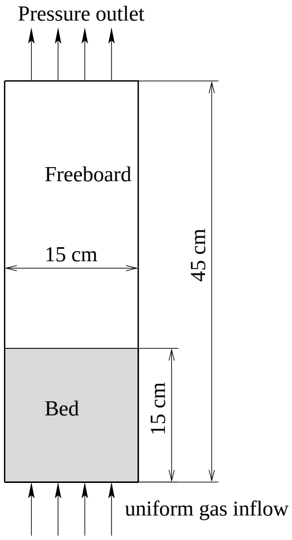

Figure 5.1 Geometry of the 2-D computational domain and boundary conditions.

simulations, the initial and boundary conditions are listed in Tab. 5.2, and numbers for the minimum fluidization voidage and inlet gas velocity will follow in the text.

A case simulating the monodispersed powder of large particles was first performed to calibrate the particle rotation model incorporated into MFIX. The minimum fluidization voidage $\varepsilon_{\mathrm{mf}}$ was set to 0.417 and the gas inflow velocity was 1.5 U_{mf}, where the U_{mf} is for large particles (see Tab. 5.2). Simulations without and with particle rotation were run for 10 seconds. The instantaneous gas volume fractions are shown at two-second intervals in Fig. 5.2. Each subfigure (a-f) has a pair of frames, whereby the left frame shows results for the simulation without particle rotation and the right frame shows results with particle rotation. The model with particle rotation predicts bigger bubbles and higher gas volume fractions compared to the model without particle rotation. The primary reason is that more energy dissipates due to particle rotation and particle velocities decrease after impact, leading to a more closely spaced particle ensemble and thus higher gas volume fraction. A consequence is that gas-solid interactions exert higher drag forces on particles and cause the particles to move vigorously. Thus, particle rotation increases the bubble intensity, which is consistent with the numerical findings of Hoomans et al. (1996) using a discrete particle model.

Time-averaged results were analyzed after 5 s to avoid initial transient fluctuations. Aver-

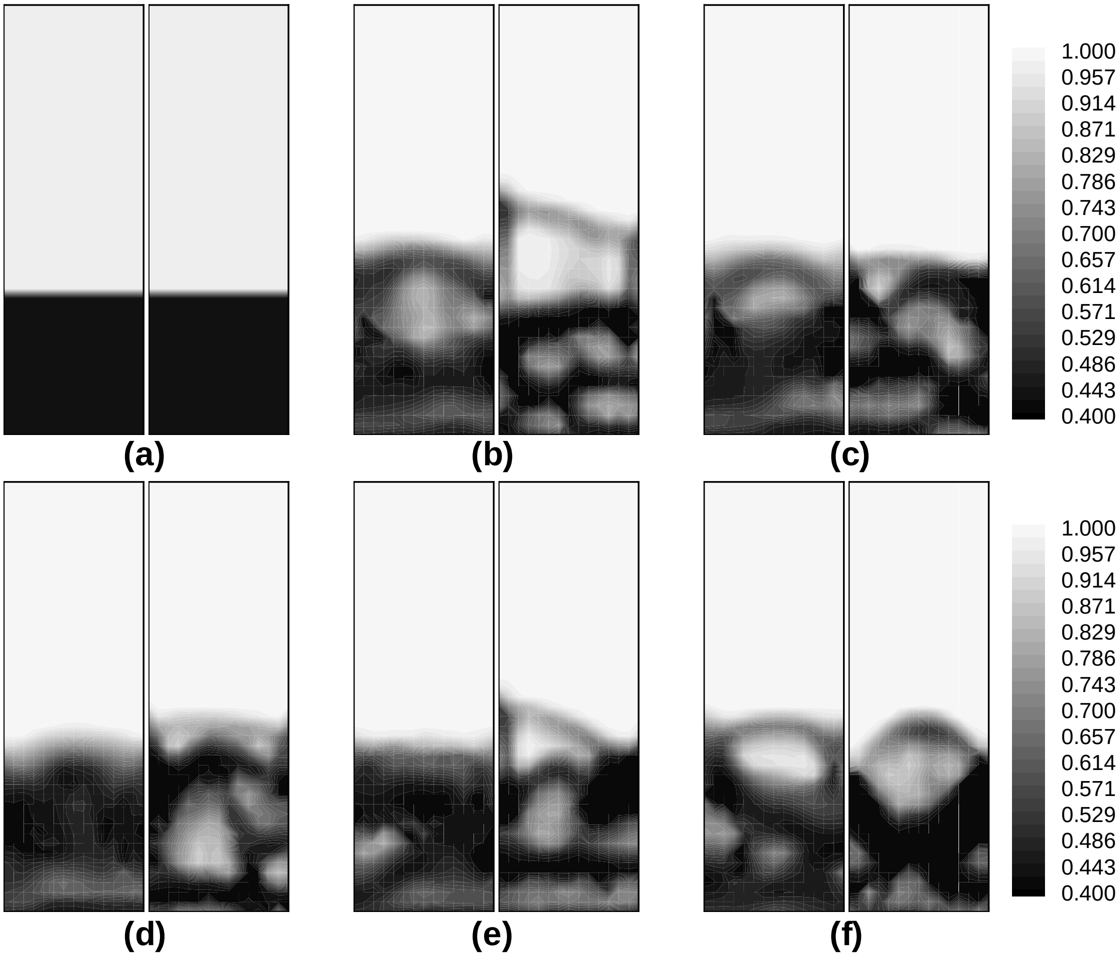

Figure 5.2 Instantaneous gas volume fraction for a monodispersed fluidized bed with inlet gas velocity of 1.5 U_{mf} at (a) 0 s, (b) 2 s, (c) 4 s, (d) 6 s, (e) 8 s and (f) 10 s. For each subframe, the left side are simulations without particle rotation and the right frame with particle rotation.

Table 5.2 Computational domain and general initial and boundary conditions.

Geometry:	
Height of domain	45 cm
Width of domain	15 cm
Horizontal grid size, Δx	1.0 cm
Vertical grid size, Δy	1.0 cm
Initial conditions:	
Freeboard region	
ε_{g}	1.0
v_{g}	U_{mf}
Bed region	
Initial bed height	15 cm
ε_{g}	$\varepsilon_{\mathrm{mf}}$
v_{g}	$U_{\mathrm{mf}}/\varepsilon_{\mathrm{mf}}$
Boundary conditions:	
Uniform gas inflow	Specified velocity
Specified pressure at outlet	101325.0 Pa
Wall boundary for gas phase	No slip
Wall boundary for solid phase	Partial slip

aging from 5 s to 10 s is sufficient since further averaging in time beyond 10 s provides no new additional information for this monodispersed system. The solid volume fraction averaged over 5-10 s is shown in Fig. 5.3 (a) and (b) without and with particle rotation, respectively. The particle volume fraction profile without particle rotation has a more homogeneous distribution. With particle rotation, higher particle volume fractions were obtained near the walls and larger bubbles formed in the bed center as was demonstrated in Fig. 5.2. This near-wall distribution is consistent with experimental observations of Goldschmidt (2001). In Fig. 5.4, a similar comparison shows that the particle rotation model also predicts better particle distribution for the same case where the inlet gas velocity is increased to 2.0 U_{mf}.

To characterize the bed expansion, an average particle height is defined as

$$< h_{\mathrm{p}} >= \frac{\sum_i^{N_{\mathrm{part}}} h_i}{N_{\mathrm{part}}} = \frac{\sum_k^{N_{\mathrm{cells}}} \varepsilon_{\mathrm{s},\,k} h_k}{\sum_k^{N_{\mathrm{cells}}} \varepsilon_{\mathrm{s},\,k}}. \tag{5.22}$$

The time-averaged particle height was calculated over 5-10 s. The $< h_{\mathrm{p}} >$ from the simulations without and with particle rotation were compared to the experimental data in

Table 5.3 Time averaged bed heights from experiments and simulations.

	1.5 U_{mf}	2.0 U_{mf}
Experiments	0.1140 m	0.1180 m
Model without rotation	0.0921 m	0.1102 m
Model with rotation	0.0973 m	0.1176 m

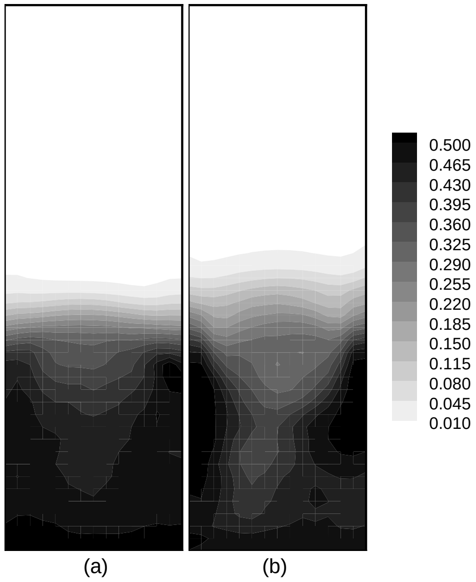

Figure 5.3 Time averaged particle volume fraction for a monodispersed fluidized bed with inlet gas velocity of 1.5 U_{mf} for the model (a) without particle rotation and (b) with particle rotation.

Tab. 5.3. Overall, the model with particle rotation was able to better capture bubble dynamics and bed expansion of monodispersed gas-solid fluidized systems. Based on these results for a monodispersed fluidized bed, the particle rotation model should better predict the segregation phenomena in a polydispersed system where bubbles play a dominant role in transporting particles.

Simulations of a binary mixture of small and large particles were examined next. The minimum fluidization voidage is also 0.417. The initial gas velocity v_{g} was set as the minimum fluidization velocity of the small particles in the freeboard region. The mass fraction of the small particles x_{small} was 0.5. Small and large particles were perfectly mixed. This assumption yields equal volume fractions of both small and large particles assuming the maximum packing density

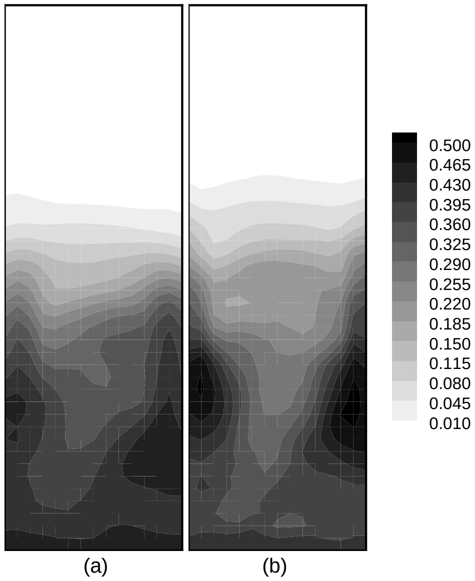

Figure 5.4 Time averaged particle volume fraction for a monodispersed fluidized bed with inlet gas velocity of 2.0 U_{mf} for the model (a) without particle rotation and (b) with particle rotation.

in a fluidized state for small and large particles are equal. The gas inflow velocity is 1.3 m/s, slightly higher than the minimum fluidization velocity of the larger particles. Simulations without and with particle rotation were both run for 20 s each.

Figure 5.5 shows bubble dynamics of the binary mixture system without and with particle rotation. The instantaneous gas volume fractions are shown in Fig. 5.5. Each subfigure (a-f) has a pair of frames, whereby the left frame shows results for the simulation without particle rotation and the right frame shows results for particle rotation. It can be seen that larger bubbles formed, i.e., the bubble intensity increased, with the inclusion of particle rotation.

To understand the particles distribution in the bed, time averaged solid volume fractions spatially averaged over the bed width, are shown in Fig. 5.6 with respect to the bed height. Each curve represents the particle distribution with respect to particle size and rotation. The model without particle rotation predicts significant segregation, whereby large particles predominately occupy the bottom of the bed and small particles reside closer to the top. In contrast, the solid volume fractions of the small and large particles based on the rotation model tend to be equally distributed throughout the bed. The model with particle rotation

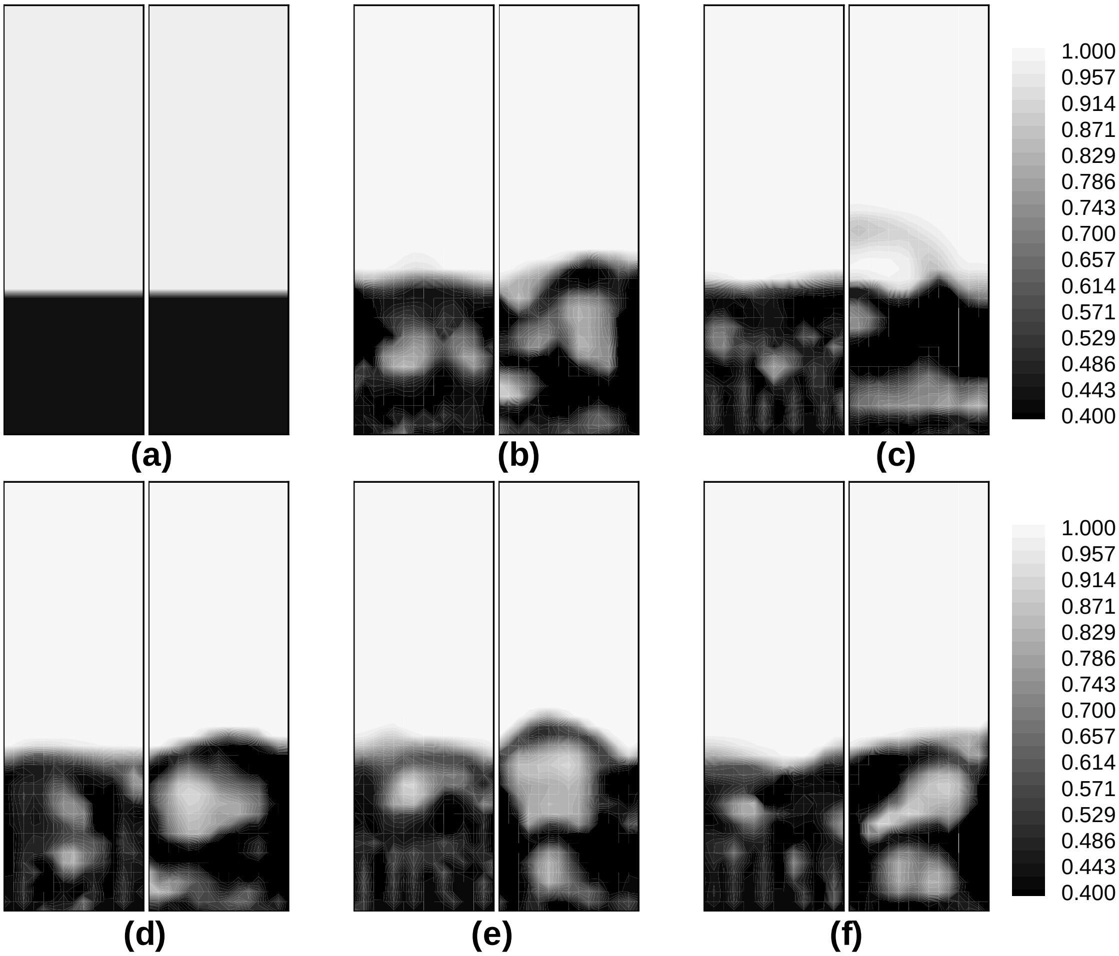

Figure 5.5 Instantaneous gas volume fraction for a bidispersed fluidized bed at (a) 0 s, (b) 6 s, (c) 10 s, (d) 14 s, (e) 18 s and (f) 20 s. For each subframe, The left side are simulations without particle rotation and the right frame with particle rotation.

predicts better mixing except at the bottom, where there is a small difference between them. The model with particle rotation also predicts higher bed expansion because of larger bubble intensity as mentioned above.

To further investigate the segregation extent and rate, the segregation percentage is defined (Goldschmidt et al., 2003):

$$s_{\mathrm{p}} = \frac{S_{\mathrm{p}} - 1}{S_{\mathrm{p,max}} - 1}, \tag{5.23}$$

and s_{p} equals 0 when the particles are perfectly mixed and 1 when the mixture has completely segregated. The parameter S_{p} is the ratio of the average heights of the small and large particles

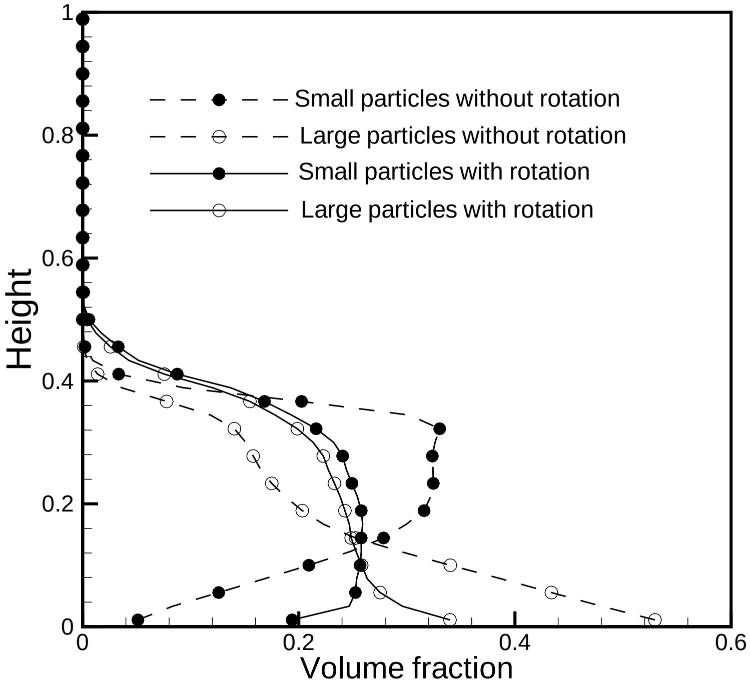

Figure 5.6 Time averaged solid volume fractions as a function of bed height normalized by the maximum bed height 45 cm.

according to Eqn. 5.22:

$$S_{\mathrm{p}} = \frac{< h_{\mathrm{small}} >}{< h_{\mathrm{large}} >}. \tag{5.24}$$

The parameter $S_{\mathrm{p,max}}$ is the maximum degree of segregation, which can be calculated in terms of mixture composition (assuming the maximum packing density in the fluidized state for small particles equals that for large particles) from:

$$S_{\mathrm{p,max}} = \frac{2 - x_{\mathrm{small}}}{1 - x_{\mathrm{small}}}. \tag{5.25}$$

Figure 5.7 shows the segregation percentage for the numerical simulations without and with particle rotation and how they compare to the experimental data provided by Goldschmidt (Goldschmidt et al., 2003; Goldschmidt, 2001). The experimental data were averaged over 1 s time intervals, while the numerical results are instantaneous values at 0.1 s time intervals. The simulation without particle rotation over-predicts the segregation percentages and has a much higher segregation rate. The simulation with particle rotation, on the other hand,

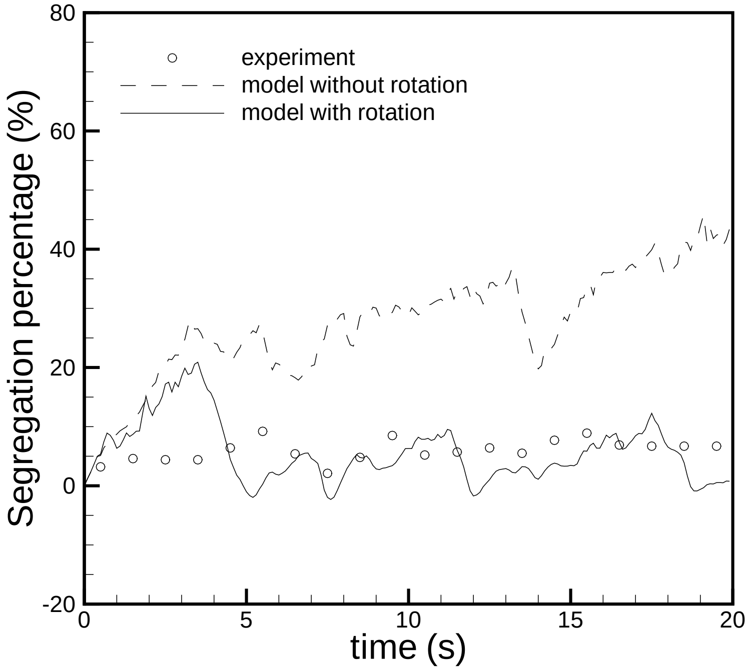

Figure 5.7 Segregation percentages from simulations without and with particle rotation and experiments for gas inlet velocity of 1.30 m/s, experimental data were averaged over 1 s time intervals.

is in good agreement with the experimental data. For this case, recall that the inlet velocity was slightly greater than the minimum fluidization velocity for the larger particles. Thus, both small and large particles fluidize, creating a well mixed system.

Further simulations using MFIX (without and with the rotational model) were conducted for other bidispersed fluidized bed systems (for example, the study by Hoomans et al. (2000)). Results showed the same improvement: the rotational model effectively reduced segregation percentages as long as the inlet gas flow was within the same limits with respect to the small and large particle minimum fluidization velocities.

It is, however, worth while to point out that the particle rotation model does not have the same kind of improvement for segregation cases where the gas inlet velocity is between the minimum fluidization velocities of the small and large particles. As shown in Fig. 5.8, for a case with gas inlet velocity at 1.0 m/s, numerical results with and without particle rotation

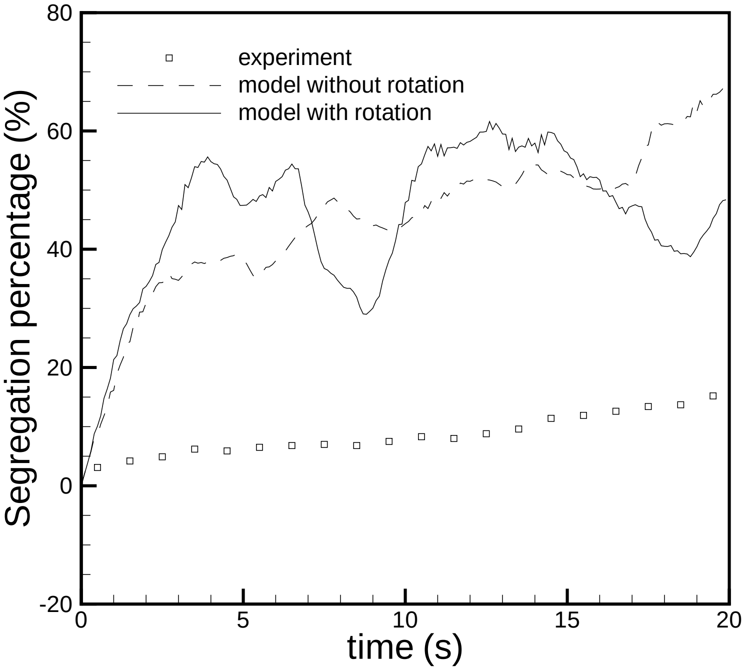

Figure 5.8 Segregation percentages from simulations without and with particle rotation and experimentsfor gas inlet velocity of 1.00 m/s, experimental data were averaged over 1 s time intervals.

both predicted much higher segregation percentages than the experimental data. The particle rotation model predicted larger fluctuations of the segregation percentages, which can also be attributed to the increased bubble intensity by this model. The major discrepancy between numerical results and experimental results, however, is due to the fact that the large particles are not very well fluidized in this conditions and thus the "hindrance effect" (Gera et al., 2004) is produced between the small particles and the reluctant large particles. To account for this kind of hindrance effect is beyond the capability of the current kinetic theory for granular flows.

5.4 Conclusions

A multi-fluid Eulerian model has been improved by incorporating particle rotation using a simplified kinetic theory for rapid granular flow of slightly frictional spheres. Simulations without and with particle rotation were performed to study bubble dynamics in a monodispersed gas-solid fluidized bed and segregation phenomena in a dense gas-solid fluidized bed of a binary solid mixture. Results were compared between simulations with and without the particle rotation model and with corresponding experimental results. To the authors' knowledge, this is the first time a multi-fluid model with particle rotation has been used to study segregation phenomena in gas-fluidized beds. In the monodispersed system, bubble intensity and bed expansion increased as a result of more energy dissipation with the particle rotation model, which better agrees with experimental results. In the binary systems studied in this paper, better agreement was achieved by using the model with particle rotation in the regime where kinetic theory is applicable and the particle-particle interactions have a noticeable effect on segregation. Despite these limitations on applications of the particle rotation model, preliminary results indicated that particle rotation is an important microscopic physics to be incorporated into the fundamental hydrodynamic model.

For further model development, the particle rotation effect can be more directly coupled to the momentum transfer between solid phases, which is very important to segregation, in the following two aspects. First, the granular temperature can be included in the solids momentum transfer term. Second, the influence of particle rotation on collisional transfer of the linear momentum can be considered by more sophisticated kinetic theory. Whether including these two factors will better model segregation phenomena in bubbling gas-fluidized beds will be of interest for further investigation. The authors also recognize that the two-dimensional domain reduces the rotation effect, therefore, particle rotation in a three-dimensional domain will be addressed in future studies.

CHAPTER 6. DYNAMICS AND STRUCTURES OF SEGREGATION IN A DENSE, VIBRATING GRANULAR BED

A paper published in *Physical Review E* [1]

Jin Sun, Francine Battaglia and Shankar Subramaniam

Abstract

We study the rise dynamics of a large particle in a granular bed under vertical vibration using molecular dynamics simulations. Systematic variation of the particle properties and external wall friction in the simulations shows that the large particle rising is very sensitive to external wall friction. The dynamical response of the granular bed with wall friction is shown to include an expansion stage and a compression stage within one cycle. With wall friction, large-scale force networks bearing larger-than-average forces are found in the compression stage. However, without wall friction, large strong force networks do not exist. The distribution of normal contact forces in the force networks is found to have an exponential tail similar to those in packing experiments. Numerical estimation of the two-point spatial correlation of normal contact force reveals predominantly short-range force correlation persisting over only 2-3 particle diameters. The structural properties of the force network are analyzed using a novel graph-theoretic approach, which is a modification of a minimum spanning tree (MST) constructed on the particles in physical space. The modified MST algorithm, which identifies *local* structures such as nearest neighbors, asymptotically recovers all particle contacts, the force distribution, and spatial force correlation of the force network. This indicates that although wall friction strongly affects the rising dynamics of the Brazil nut over the device scale (tens of particle diameters) through the force network, it does so through *local* short-range interactions.

---

[1] *Physical Review E (Statistical, Nonlinear, and Soft Matter Physics)*, 74(6):061307–13, 2006.

Thus this study affirms the basis for *local* constitutive models in continuum descriptions of segregation.

6.1 Introduction

Segregation in granular media occurs both in nature and in industrial processes. Therefore, a fundamental understanding of the dynamics and mechanisms of segregation is of practical importance. A canonical problem in granular segregation is the rise or fall of a large particle in a bed of small particles as a consequence of vibration applied to the granular bed. This phenomenon was first named the "Brazil nut problem" (BNP) [2] by Rosato et al. (1987), who used a Monte Carlo method to study this problem. Since then there have been extensive experimental studies, theoretical investigations, and computer simulations of the BNP. Simulation of the BNP is acknowledged as a benchmark of granular segregation.

Granular segregation observed in the BNP is dependent on particle properties, flow conditions and external boundary conditions, and is not explained by a single mechanism. While many mechanisms have been proposed from different perspectives to explain the BNP phenomenon, no unified theory has yet emerged and our understanding is still incomplete. This is in part because the mechanisms do not solely manifest themselves in clearly demarcated regimes, but rather they appear to coexist across different regimes. The problem is further complicated by the interaction between different time and length scales, which is affected by the bed vibration parameters, namely the amplitude and frequency (Rosato et al., 2002).

The vibration parameters can be characterized by the dimensionless amplitude A_0/d_0, where A_0 is the vibration amplitude and d_0 is the particle diameter, and the dimensionless frequency $\omega_0\sqrt{d_0/g}$. When characterizing the dynamics of the BNP, these appear in combination as a dimensionless acceleration $\Gamma = A_0\omega_0^2/g$, which characterizes the acceleration due to external forced vibration relative to gravity.

Some segregation mechanisms may be classified into two categories according to the acceleration and frequency in the system (Huerta and Ruiz-Suárez, 2004b). For $\Gamma > 1$ and low

---

[2] The Brazil nut is a name coined from the observed behavior of shaking a can of mixed nuts and noting that the Brazil nut rises to the top.

frequencies, convection and inertia are proposed as segregation mechanisms. Convection, where particles descend along vertical (frictional) walls and ascend at the center, is proposed as the dominant mechanism (Knight et al., 1993) when ρ_{r}, the relative density of the large particle to small particles, is less than a critical value ρ_{rc} ($\rho_{\mathrm{rc}} \approx 0.57$ from experiments in Ref. (Huerta and Ruiz-Suárez, 2004a)). On the other hand, inertia dominates when $\rho_{\mathrm{r}} > \rho_{\mathrm{rc}}$. The inertia effect is believed to dominate segregation in the granular system studied in this paper, where $\Gamma = 3.39$, $\omega_0 \sqrt{d_0/g} = 0.67$ and $\rho_{\mathrm{r}} = 7.09$ (calculated from parameters in Table 6.1).

For $\Gamma > 1$ with small amplitudes and high frequencies, where the granulate is fluidized without convection, a "buoyancy force" analogous to fluid buoyancy has been proposed to predict the Brazil nut effect (Shishodia and Wassgren, 2001; Trujillo et al., 2003). Other mechanisms from topological considerations have also been proposed, such as arching (Duran et al., 1993) and "void filling" beneath large particles (Rosato et al., 2002). In addition to these mechanisms, air-driven segregation has also been found to be important in the case of very fine particles (Möbius et al., 2001; Burtally et al., 2002; Möbius et al., 2004). Despite the variety of mechanisms proposed, many important details of the microscopic dynamics driving the segregation remain unknown. For instance, while the existence of force chains in three-dimensional vibrating granular systems and its role in the segregation have been hypothesized (Nahmad-Molinari et al., 2003), the sensitivity of the force chain formation to external boundary conditions is still unclear.

In this paper, we investigate the segregation dynamics of the BNP using molecular dynamics (MD) simulations, which allow us to systematically examine the effects of particle properties and external wall boundary conditions that are not easily controllable in experimental studies. We compare the rising time to a related experimental system (Nahmad-Molinari et al., 2003) and show that the rising of the large particle is very sensitive to wall friction. Furthermore, we show the existence of large-scale force networks when wall friction is present and relate the rise dynamics to formation and destruction of these force networks. We also calculate the force distribution and force correlation within the granular bulk and discuss their physical implications and similarity to force statistics in granular packs. We propose a graph-theoretic

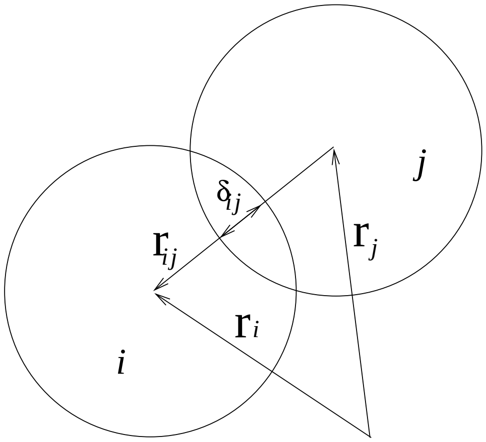

Figure 6.1 Schematic of two particles i and j in contact and position vectors $\mathbf{r}_i$, $\mathbf{r}_j$, respectively, with overlap δ_{ij}.

approach based on minimum spanning trees (MST) to analyze the force networks. The multi-pass MST is shown to capture microstructural information, i.e., the particle configuration and connectivity information, which may be used to define a length scale for continuum modeling. Force statistics are also recovered by the multi-pass MST algorithm.

In the next section we briefly describe the simulation methodology and computational model setup. In section 6.3, we present results for rising dynamics, force networks and the MST algorithm. In section 6.4 we summarize and conclude this work.

6.2 Model and method

Molecular dynamics simulations of the Brazil nut problem are performed using a soft sphere model for one large particle and $N-1$ small particles, which interact via contact laws and friction only on contact. Since the realistic modeling of particle deformations is complicated, a simplified contact force and the overlap relation (Silbert et al., 2001), the so called spring-dashpot model, is used in this work. The principle of the computational model used in the MD simulations is demonstrated in the following.

For two contacting particles $\{i, j\}$, with radii $\{a_i, a_j\}$, at positions $\{\mathbf{r}_i, \mathbf{r}_j\}$, with velocities $\{\mathbf{v}_i, \mathbf{v}_j\}$ and angular velocities $\{\boldsymbol{\omega}_i, \boldsymbol{\omega}_j\}$ (see figure 6.1), the normal compression δ_{ij}, relative normal velocity $\mathbf{v}_{\mathrm{n}_{ij}}$, and relative tangential velocity $\mathbf{v}_{\mathrm{t}_{ij}}$ are (Silbert et al., 2001):

$$\delta_{ij} = d - r_{ij}, \tag{6.1}$$

$$\mathbf{v}_{\mathrm{n}_{ij}} = (\mathbf{v}_{ij} \cdot \mathbf{n}_{ij})\mathbf{n}_{ij}, \tag{6.2}$$

$$\mathbf{v}_{\mathrm{t}_{ij}} = \mathbf{v}_{ij} - \mathbf{v}_{n_{ij}} - (a_i\boldsymbol{\omega}_i + a_j\boldsymbol{\omega}_j) \times \mathbf{n}_{ij}, \tag{6.3}$$

where $d = a_i + a_j$, $\mathbf{r}_{ij} = \mathbf{r}_i - \mathbf{r}_j$, $\mathbf{n}_{ij} = \mathbf{r}_{ij}/r_{ij}$, with $r_{ij} = |\mathbf{r}_{ij}|$ and $\mathbf{v}_{ij} = \mathbf{v}_i - \mathbf{v}_j$. The rate of change of the elastic tangential displacement $\mathbf{u}_{\mathrm{t}_{ij}}$, set to zero at the initiation of a contact is:

$$\frac{\mathrm{d}\mathbf{u}_{\mathrm{t}_{ij}}}{\mathrm{d}t} = \mathbf{v}_{\mathrm{t}_{ij}} - \frac{(\mathbf{u}_{\mathrm{t}_{ij}} \cdot \mathbf{v}_{ij})\mathbf{r}_{ij}}{r_{ij}^2}. \tag{6.4}$$

The last term in equation 6.4 arises from the rigid body rotation around the contact point and ensures that $\mathbf{u}_{\mathrm{t}_{ij}}$ always lies in the local tangent plane of contact. Normal and tangential forces acting on particle i are:

$$\mathbf{F}_{\mathrm{n}_{ij}} = f(\delta_{ij}/d)(k_{\mathrm{n}}\delta_{ij}\mathbf{n}_{ij} - \gamma_{\mathrm{n}} m_{\mathrm{eff}}\mathbf{v}_{\mathrm{n}_{ij}}), \tag{6.5}$$

$$\mathbf{F}_{\mathrm{t}_{ij}} = f(\delta_{ij}/d)(-k_{\mathrm{t}}\mathbf{u}_{\mathrm{t}_{ij}} - \gamma_{\mathrm{t}} m_{\mathrm{eff}}\mathbf{v}_{\mathrm{t}_{ij}}), \tag{6.6}$$

where $k_{\mathrm{n,t}}$ and $\gamma_{\mathrm{n,t}}$ are the spring stiffness and viscoelastic constants, respectively, and $m_{\mathrm{eff}} = m_i m_j/(m_i + m_j)$ is the effective mass of spheres with masses m_i and m_j. The corresponding contact force on particle j is simply given by Newton's third law, i.e., $\mathbf{F}_{ji} = -\mathbf{F}_{ij}$. The function $f(\delta_{ij}/d) = 1$ is for the linear spring-dashpot model, and $f(\delta_{ij}/d) = \sqrt{\delta_{ij}/d}$ is for Hertzian contacts with viscoelastic damping between spheres.

Static friction is implemented by keeping track of the elastic shear displacement throughout the lifetime of a contact. The static yield criterion, characterized by a local particle friction coefficient μ, is modeled by truncating the magnitude of $\mathbf{u}_{\mathrm{t}_{ij}}$ as necessary to satisfy $|\mathbf{F}_{\mathrm{t}_{ij}}| < |\mu\mathbf{F}_{\mathrm{n}_{ij}}|$. Thus the contact surfaces are treated as "sticking" when $|\mathbf{F}_{\mathrm{t}_{ij}}| < |\mu\mathbf{F}_{\mathrm{n}_{ij}}|$, and as "slipping" when the yield criterion is satisfied.

In a gravitational field $\mathbf{g}$, the translational and rotational accelerations of particles are determined by Newton's second law in terms of the total forces acting on each particle i:

$$\mathbf{F}_i^{\mathrm{tot}} = m_i\mathbf{g} + \sum_j \mathbf{F}_{\mathrm{n}_{ij}} + \mathbf{F}_{\mathrm{t}_{ij}} - b\mathbf{v}_i, \tag{6.7}$$

and total torques acting on each particle i:

$$\boldsymbol{\tau}_i^{\text{tot}} = -\frac{1}{2}\sum_j \mathbf{r}_{ij} \times \mathbf{F}_{\mathrm{t}_{ij}}. \tag{6.8}$$

The last term $-b\mathbf{v}_i$ in the force equation represents an external damping force. This term is used to artificially enhance the energy dissipation due to two-particle contact, which is under-predicted by the MD contact force model (Luding, 2004; Luding et al., 1994). A similar damping term can also arise from the viscous drag a particle experiences due to the presence of an interstitial fluid, but that term is proportional to the relative velocity between particle and fluid.

The amount of energy lost in collisions is characterized by the inelasticity through the value of the coefficient of restitution e, which is defined as the negative ratio of the particle normal velocity after collision to the velocity before collision. For the linear spring-dashpot model, the coefficient of normal restitution and contact time can be analytically obtained:

$$e_{\mathrm{n}} = \exp(-\gamma_{\mathrm{n}} t_{\mathrm{c}}/2), \tag{6.9}$$

where the contact time t_{c} is given by:

$$t_{\mathrm{c}} = \pi(k_{\mathrm{n}}/m_{\mathrm{eff}} - \gamma_{\mathrm{n}}^2/4)^{-1/2}. \tag{6.10}$$

The value of the spring constant should be large enough to avoid particle interpenetration, yet not so large as to require an unreasonably small simulation time step δt, since an accurate simulation typically requires $\delta t \sim t_{\mathrm{c}}/50$. After the contact force is calculated, the equations of motion, which are ordinary differential equations, can be numerically integrated to get the particle trajectories.

The computational setup models the experiment in Ref. (Nahmad-Molinari et al., 2003). In the experimental work, a steel bead was placed at the bottom of a bed of cabbage seeds in a column vibrated by a sinusoidal excitation. The available experimental parameters include the granular bed height of 12 cm; small particle diameter of 0.2 cm, large particle diameter of 0.632 cm, and their densities of 7.8 g/cm^3 and 1.1 g/cm^3, respectively; and the sinusoidal vibration with frequency 7.5 Hz and amplitude 1.5 cm. The basic computational parameters

Table 6.1 Basic computational parameters settings

	Small particle	Large particle
Number of particles	7600 [3]	1
Particle diameter	d_0	3.16 (d_0)
Particle density	1.91 (m_0/d_0^3)	13.54 (m_0/d_0^3)
Particle normal stiffness coefficient k_n	$2 \times 10^5\,(k_0)$	
Particle tangential stiffness coefficient k_t	$\frac{2}{7}\,k_\mathrm{n}$	
Particle normal damping coefficient γ_n	$40\,(\frac{1}{t_0})$	
Particle tangential damping coefficient γ_t	$0\,(\frac{1}{t_0})$	
Particle friction coefficient μ	0.5	
Background damping coefficient b	0 for most cases $(m_0\sqrt{g/d_0})$ [4]	
Particle restitution coefficient	0.9	0.86
Wall normal stiffness coefficient	$2 \times 10^5\,(k_0)$	
Wall tangential stiffness coefficient	$\frac{2}{7}\,k_\mathrm{n}$	
Wall normal damping coefficient	$40\,(\frac{1}{t_0})$	
Wall tangential damping coefficient	$20\,(\frac{1}{t_0})$	
Wall friction coefficient μ_wall	0.5	
Vibration frequency	$0.107\,(\frac{1}{t_0})$	
Vibration amplitude A_0	$7.5\,(d_0)$	
Time step	$2 \times 10^{-4}\,(t_0)$	

are chosen to mimic the experiment as closely as possible, and are listed in Table 6.1. In this computational study, a non-dimensional system of equations are solved, where the scaling factors for distance, time, velocity, force, elastic constants, and stresses are: d_0, $t_0 = \sqrt{d_0/g}$, $v_0 = \sqrt{gd_0}$, $F_0 = m_0g$, $k_0 = m_0g/d_0$ and $\sigma = m_0g/d_0^2$, respectively. The diameter and mass of the small particles are d_0 and m_0.

All the cases were simulated in three-dimensions using a molecular dynamics code for granular materials, GRANFLOW (Silbert et al., 2001). The granular media is confined in a cylindrical container, as shown in Fig. 6.2. The cylinder has a diameter of $12.25\,d_0$ and the cylinder height is effectively infinite to allow for unrestricted particle rise. The initial particle configuration (Fig. 6.2) for the large particle is at the bottom of the bed, surrounded by small particles. The initial condition for the segregation simulations is constructed in two steps. First, the large particle is fixed at the bottom and surrounded by small particles. The entire column is vibrated at a high frequency until an equilibrium height is reached; then the frequency is terminated to allow the particles to relax to a ground state, where the total particle kinetic

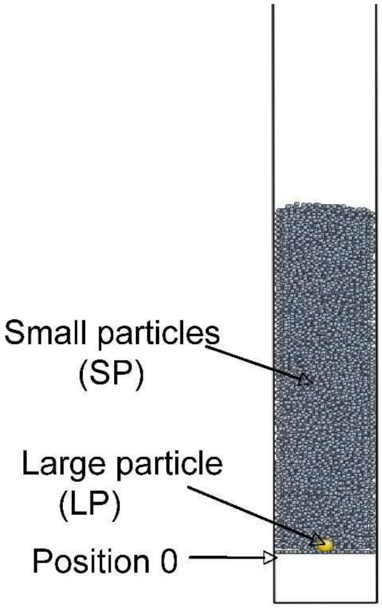

Figure 6.2 (Color online) The initial particle configuration as seen in a vertical cut-plane through the 3-D simulation, with the large particle (in yellow) at the bottom and the surrounding small particles (in grey).

energy is zero. At this state, the particles are arranged in a compact configuration, which is then used as the initial condition for the segregation study. For the case with 6001 particles, the initial bed height is about 43 d_0 and with 7601 particles, the initial height is about 55 d_0. The different heights of the granular pack will be indicated for the cases in the next section. It should be noted that the MD model allows for contact force and friction between the particles and the cylindrical walls in the same way as described for two particles but with infinite mass and diameter for the walls.

In this paper we focus on analyzing segregation using the particle sizes, mass ratio and external excitation conditions as specified in Table 6.1. Unlike most experimental work, where these parameters are varied to determine their effect on the segregation mechanism, we use these parameters as given conditions and investigate other effects that cannot easily be studied by experimental techniques. The effect of wall friction on the Brazil nut rising dynamics as well as the parametric studies are investigated in the next section.

6.3 Results

6.3.1 Brazil nut rising dynamics

The rise time of the large particle is an important phenomenological indicator of segregation in the Brazil nut problem. Although many particle properties needed for the MD simulations are not known from the experiment, a set of computational parameters is established (see Table 6.1) to predict the correct rising behavior of the large particle, i.e., rising from the bottom to the top and fluctuating about an equilibrium height with small amplitudes [5]. The rise time predicted from one simulation is compared with the experimental results (Nahmad-Molinari et al., 2003) as shown in Fig. 6.3. Note that in this simulation the background damping coefficient $b = 0.24$ in $m_0\sqrt{g/d_0}$ units was chosen to obtain a quantitative match with the experimental result, but it is set to zero in the other simulations because it has no effect on the qualitative behavior of the simulated system. Therefore, for all the other simulations the background damping is set to zero, unless otherwise noted.

We perform parametric studies of the BNP to elucidate the effect of MD simulation parameters on rising behavior. We show that this rising behavior is robustly independent of many particle properties but sensitive to wall friction. We first investigate the effect of varying spring stiffness constant. The value of spring stiffness constant $k_\mathrm{n} = 2 \times 10^5\, k_0$ is smaller than the common value of $O(10^{10}\, k_0)$, which "softens" the particles used in the simulation. However, it is shown in Fig. 6.4(a) that with increasing spring stiffness, the large particle rise time approaches an asymptotic value, with $k_\mathrm{n} = 2 \times 10^5\, k_0$ giving a rise time close to the asymptotic value. Two different particle contact force models, namely the linear spring-dashpot model and the Hertzian model, did not change the rising behavior qualitatively, as shown in Fig. 6.4(b). With the Hertzian model, the large particle rise time was slightly slower and fluctuations in the particle position were reduced.

Interstitial gas within the granular media may play an important role in the segregation when granular particle sizes are small (Burtally et al., 2002; Möbius et al., 2004). The inter-

---

[5] Fluctuations about the equilibrium height occur due to impacts with the top layer particles which are not confined in the upward direction. In this paper, only the simulations with small fluctuations are considered, which excludes the reentrance phenomena.

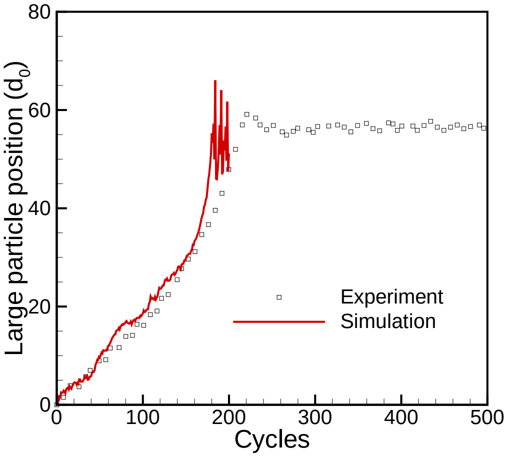

Figure 6.3 (Color online) The large particle position as a function of shaking cycles predicted from one simulation case of a granular pack with initial height of 55 d_0 with background damping, $b = 0.24$ in $m_0\sqrt{g/d_0}$ units (solid line), compared with the corresponding experimental results (open squares) Nahmad-Molinari et al. (2003).

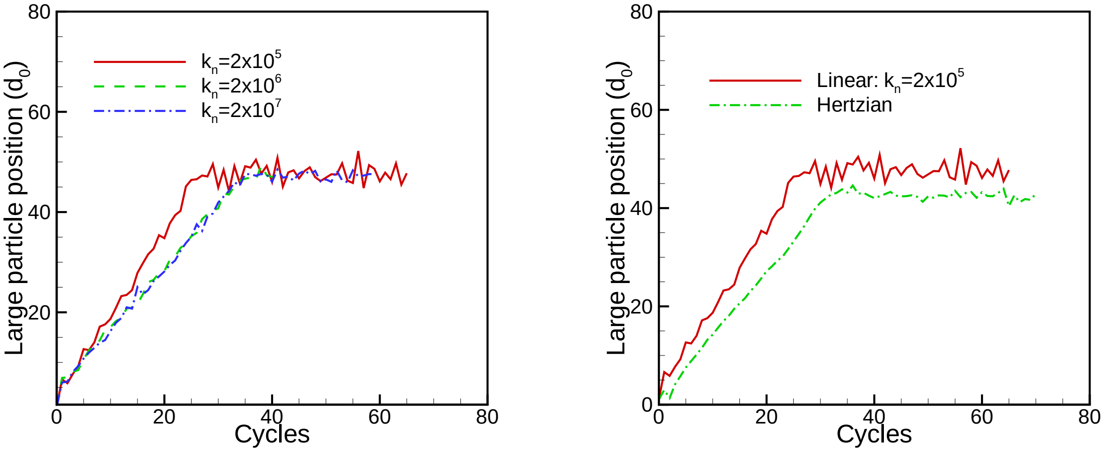

(a)

(b)

Figure 6.4 (Color online) The large particle position as a function of shaking cycles for (a) different values of spring stiffness coefficient k_n and (b) the linear and Hertzian spring-dashpot force models in a granular pack with initial height of 43 d_0.

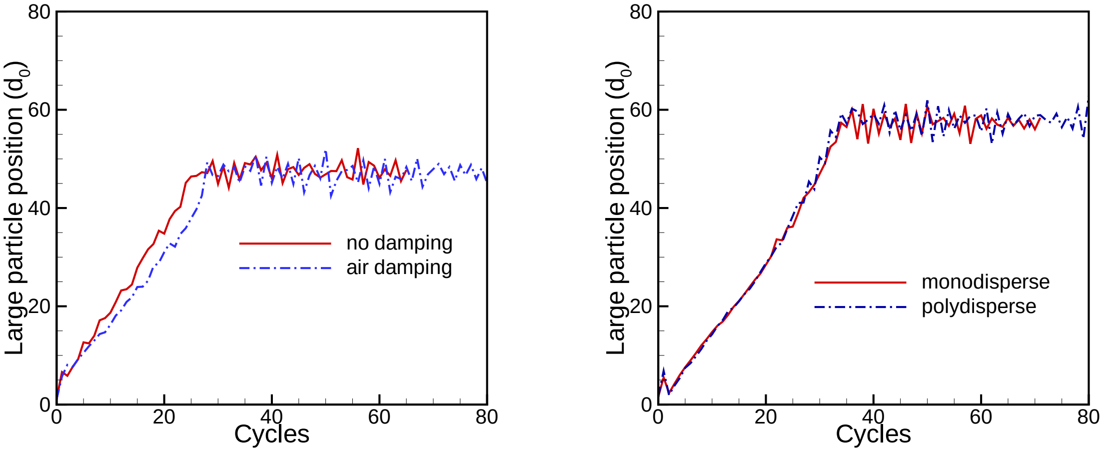

(a)

(b)

Figure 6.5 (Color online) The large particle position as a function of shaking cycles for (a) varying interstitial air damping in a granular pack with initial height of 43 d_0, (b) small particle size distributions in a granular pack with initial height of 55 d_0.

stitial gas flow effect was investigated by modeling air as an incompressible fluid and treating the granular bed as a porous medium, which gives rise to a damping term proportional to the particle slip velocity in the particle force (Biswas et al., 2003). This damping term is of the same form as the last term in equation 6.7 except that the velocity is the particle *slip* velocity (in place of the particle velocity), and the damping coefficient b is in the range $10^{-3} \sim 10^{-2}$ (in $m_0\sqrt{g/d_0}$ units). Comparing the large particle rise time with and without interstitial air effects, it can be seen from Fig. 6.5(a) that the interstitial air has minimal influence on the rise time. Thus, for this particular problem, the segregation of small and large particles are not adversely affected by the presence of interstitial air, i.e., this is not air-driven segregation.

The effects of small particle polydispersity was examined for a monodispersed case and polydispersed case, where the small particle diameters ranged from $0.9\,d_0$ to $1.1\,d_0$. The polydispersed case in Fig. 6.5(b) demonstrates almost identical rising behavior. Particle friction is another important particle property. Its effects on granular packings has been systematically studied (Silbert et al., 2002a,b). However, its effects on the dynamics in granular systems are still not clear. In this Brazil nut problem, it is shown that the variation of particle friction coef-

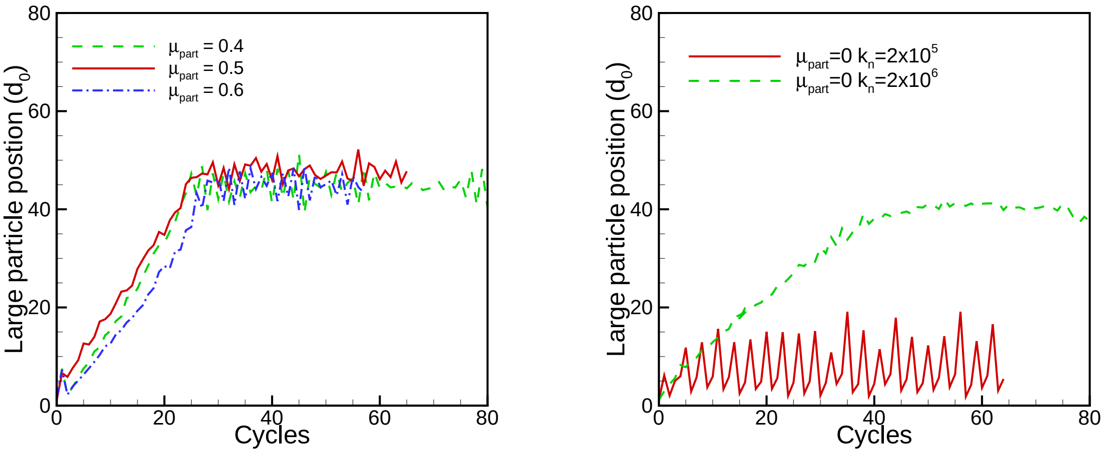

(a)

(b)

Figure 6.6 (Color online) The large particle position as a function of shaking cycles for (a) different particle friction coefficients and (b) different spring stiffness constants in a granular pack with initial height of 43 d_0.

ficient within a reasonable range does not change the rising behavior significantly (Fig. 6.6(a)). Even when there is no friction between the particles (Fig. 6.6(b)), the large particle can still rise when the particle elastic coefficient is set to $k_\mathrm{n} = 2 \times 10^6\ k_0$. This excludes particle friction as a necessary condition for the large particle to rise.

However, friction between particles and the confining cylindrical wall, referred to as wall friction hereafter, critically impacts the dynamic response of the granular system. The impact is analogous to the wall friction effects on the internal stress distribution in static granular packings as previously studied by simulations (Landry et al., 2003) and experiments (Vanel and Clément, 1999). The rising behavior of the large particle is very sensitive to wall friction. The large particle oscillates with the granular bed but cannot sustain a rising motion when the wall friction coefficient μ_wall is reduced from 0.5 to 0.1 as shown in Fig. 6.7(a). As μ_wall is reduced to zero, the fluctuation in the large particle position becomes larger as shown in Fig. 6.7(b). Increasing particle stiffness for this situation only decreases the magnitude of the fluctuation and the large particle does not rise. Thus, wall friction is necessary for the large particle to rise.

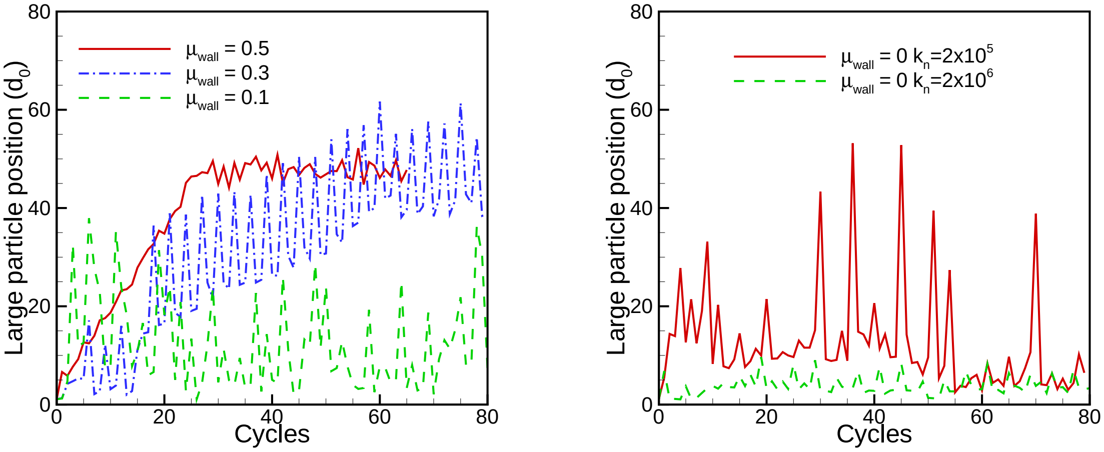

(a)

(b)

Figure 6.7 (Color online) The large particle position as a function of shaking cycles for (a) different wall friction coefficients and (b) different spring stiffness constants for no wall friction in a granular pack with initial height of 43 d_0.

A comparison between the large particle rising behaviors with ($\mu_{\text{wall}} = 0.5$) and without wall friction ($\mu_{\text{wall}} = 0.0$), as shown in Fig. 6.8(a), demonstrates that the large particle rises to the top after 30 cycles and stays at the surface of the granular bed with wall friction. However, without wall friction the large particle oscillates with no regular pattern. A closer look at the displacements for a smaller range of cycles with wall friction, shown in Fig. 6.8(b), reveals that the center of mass of the small particles and the large particle, vary in a one-cycle pattern. It is, therefore, worthwhile to analyze the dynamics of particles within one cycle. Taking a window from cycle 10 to cycle 11, as shown in Fig. 6.9, it can be observed from both the displacements (Fig. 6.9(a)) and the velocities (Fig. 6.9(b)) that the entire granular bed loses contact with the vibrating base at approximately $T = 10.05$ when the acceleration equals $-g$, and subsequently impacts with the base at around $T = 10.85$. The stage from $T = 10.05$ to 10.85 is defined as the expansion stage since the granular bed experiences dilatation during this period, while the rest of the cycle is defined as the compression stage corresponding to compaction of the granulates. These concepts will be further elucidated by the microstructural analysis presented in the next section.

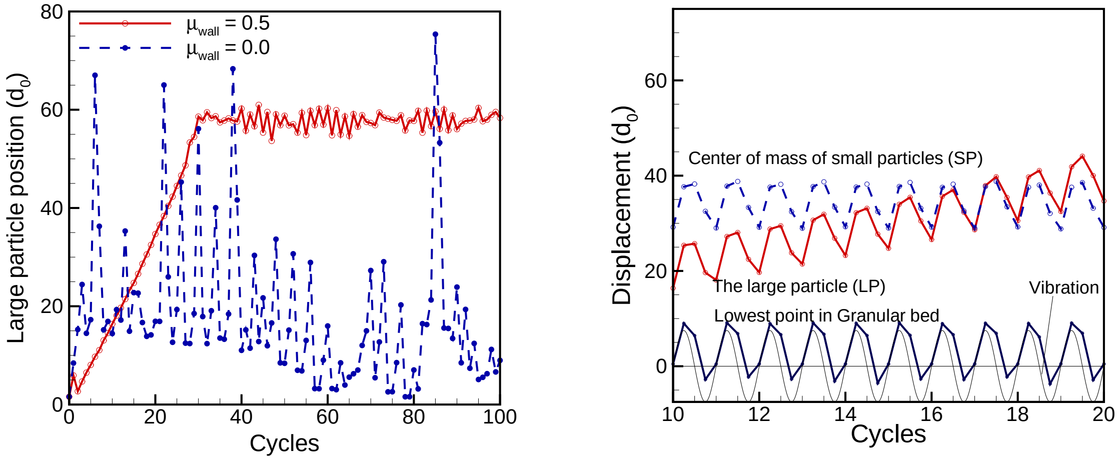

(a)

(b)

Figure 6.8 (Color online) The large particle position as a function of the shaking cycles for (a) varying wall friction μ_{wall} and (b) particle positions for the case with wall friction ($\mu_{\text{wall}} = 0.5$) from $T = 10$ to $T = 20$ in a granular pack with initial height of 55 d_0. The sinusoidal curve is shown to illustrate the vibration frequency.

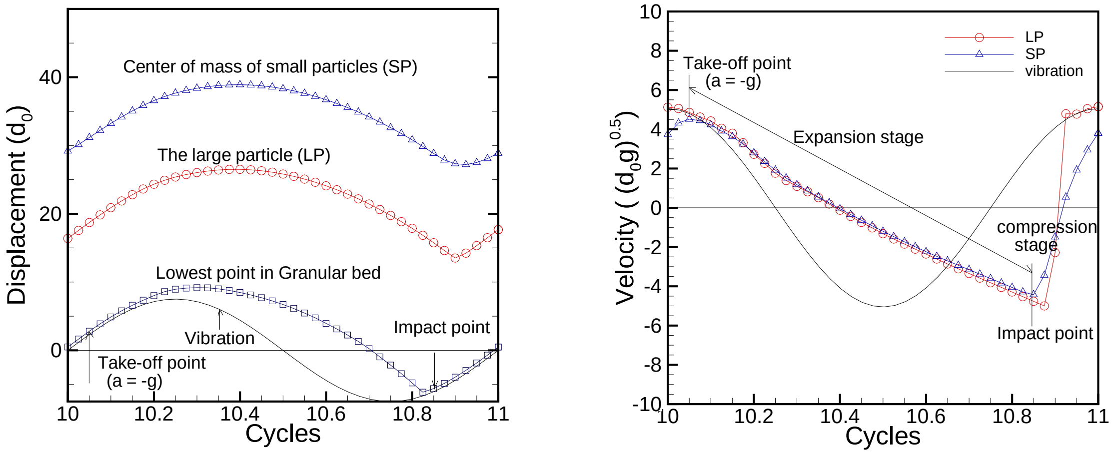

(a)

(b)

Figure 6.9 (Color online) Changes in (a) particle displacements and (b) velocities within one cycle for the case with wall friction in a granular pack with initial height of 55 d_0. The sinusoidal curve is shown to illustrate the vibration frequency.

In the expansion stage, the large particle experiences a free rise and fall together with the small particles (the height gained by the large particle can be obtained from the displacement data in Fig. 6.9(a), and it is close to $\sqrt{v^2/2g}$ calculated from the velocity data from Fig. 6.9(b).) However, in the compression stage, the large particle quickly adjusts to the vibration velocity which is transmitted through a strong force network. The large particle's velocity is greater than the velocity of the center mass of small particles (Fig. 6.9(b)). As a result the large particle rises to a higher position at cycle 11 than that at the beginning of cycle 10 (Fig. 6.9(a)). The reason behind this dynamical variation is closely related to the force network formation and destruction in one cycle as demonstrated in the next section.

6.3.2 Force networks and statistics

It is natural to speculate whether there exist structures in non-fluidized granular media (Nahmad-Molinari et al., 2003), similar to the force networks in static packings (Silbert et al., 2002b) or arches shown in two-dimensional vibrating piles (Duran et al., 1993, 1995). This is indeed the case as shown in the following data analysis, where the interaction between structures and dynamics is revealed.

Average coordination number, defined as the average number of contacts per particle, is a measure that is sensitive to the local particle configuration and has been used to characterize the static mechanical equilibrium state in static packing (Silbert et al., 2002a). In the dynamic problem studied in this paper, the time evolution of the coordination number averaged over all the particles in granular media is used to understand the dynamic response of the system and the corresponding structural information at each instance. As shown in Fig. 6.10(a), the average coordination number for the granular system with wall friction $\mu_{\text{wall}} = 0.5$ shows a periodic pattern, while the one for the granular system without wall friction shows an irregular pattern. It can be seen from the evolution of the average coordination number within one cycle in Fig. 6.10(b), that the average coordination number falls below unity during the expansion stage, indicating most particles have no contact. However, the average coordination number in the compression stage rises to 3, indicating there are multiple contacts for a particle and

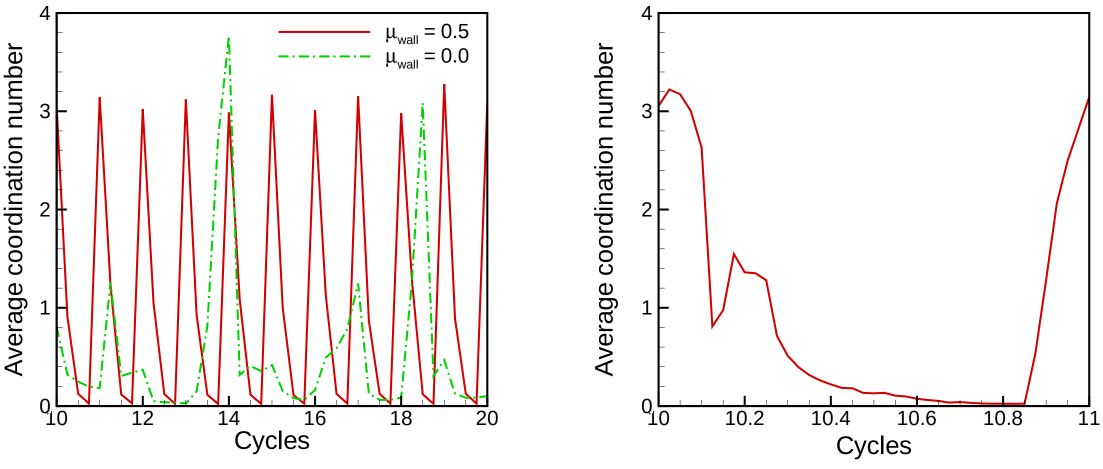

(a)

(b)

Figure 6.10 (Color online) Time evolution of the average coordination number for all the particles (a) varying within 10 cycles and (b) varying within one cycle for $\mu_{\text{wall}} = 0.5$ in a granular pack with initial height of 55 d_0.

suggesting the presence of a force network during this stage.

To provide direct evidence of the existence of force networks during the compression stage, a graph algorithm was used to identify force networks. A force network is defined as a collection of particles such that every particle in the force network is in contact with at least one other particle, and each particle has a nonzero normal contact force. For the case with wall friction and a total of 7601 particles, the total number of force networks at $T = 10$ is 80. These networks range from the minimum of two particles in contact to a very large network with many particles. It is found that at the time instant when the average coordination number reaches it maximum value of 3.2, most particles are indeed in a large force network. Of the total number of 7601 particles, 5796 particles (including the large particle) are in a force network with a network-averaged coordination number of 3.98.

Therefore, the lack of a strong force network during the expansion stage allows the large particle to move freely. The force network in the compression stage, however, supports the large particle and transmits the velocity boundary condition directly to the large particle. Since not all the small particles are in the same force network, their average velocity is not the same as that of the large particle.

A corresponding force network analysis for the case with $\mu_{\text{wall}} = 0$ reveals that there are no large force networks for most of the cycle, and the magnitude of the forces is much smaller than that with wall friction present. Configurations of the force network are visualized comparing the cases with, and without, wall friction in Fig. 6.11(a) and Fig. 6.11(b), respectively. In both figures, for clarity only connections between particles whose normal contact force F_n is greater than the average normal contact force $\bar{F}_n$ are shown. From Fig. 6.11(a), it can be clearly seen that extended force-bearing structures exist over a long length scale with wall friction; in contrast, there are no large force networks with strong forces when there is no wall friction, which results in the oscillation of the large particle.

Further analysis of the largest force network with 5796 particles reveals a strong subnetwork of 3375 particles, which carries forces $F_{\text{n}} > \bar{F}_{\text{n}}$, where $\bar{F}_{\text{n}}$ is the average normal contact force. This indicates a wide distribution of forces in the force networks. The statistics of all normal forces in the force networks are characterized by the probability density function (PDF) of the scaled forces $f = F_{\text{n}}/\bar{F}_{\text{n}}$. The PDF at $T = 10$ for $\mu_{\text{wall}} = 0.5$ is shown in Fig. 6.12(a). The PDF shows the generic feature of the force distribution in static granular packings (Mueth et al., 1998; Silbert et al., 2002b), i.e., it exhibits a peak (plateau) for small forces ($f < 1$) and exponential decay for large forces ($f > 1$). Mueth et al. (1998) fitted their experimental data with an empirical function of the form

$$P(f) = a(1 - be^{-f^2})e^{-\beta f}, \tag{6.11}$$

and found $a = 3.0$, $b = 0.75$, and $\beta = 1.5 \pm 0.1$ for a static packing of glass spheres in a cylindrical container. To compare with the static packing experimental data, we fit Eq. 6.11 to our computational data and find the function with $a = 2.46$, $b = 0.83$, and $\beta = 1.35$ agrees well with the force distribution in the force networks as shown in Fig. 6.12(a). For the expansion stages and the case where $\mu_{\text{wall}} = 0.0$, the number of contact forces is small and the PDF of forces suffers from large statistical error due to insufficient samples. Therefore, the PDF for those situations is not discussed here.

In addition to the PDF of the force distribution, the force pair correlation was also computed

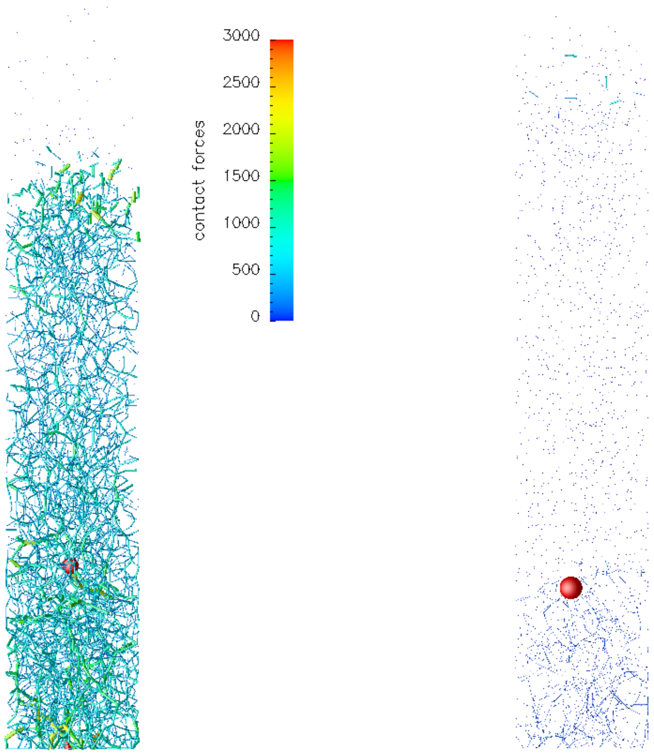

(a) (b)

Figure 6.11 (Color online) Force networks in the granular media at cycle 10 for (a) $\mu_{\text{wall}} = 0.5$ (b) $\mu_{\text{wall}} = 0.0$. In the figures, both the edge thickness and color scales are proportional to the magnitude of normal forces. The (red) sphere indicates the position of the large particle and the dots indicate the positions of small particles. Only the edge with forces $F_n > \bar{F}_n$ are shown.

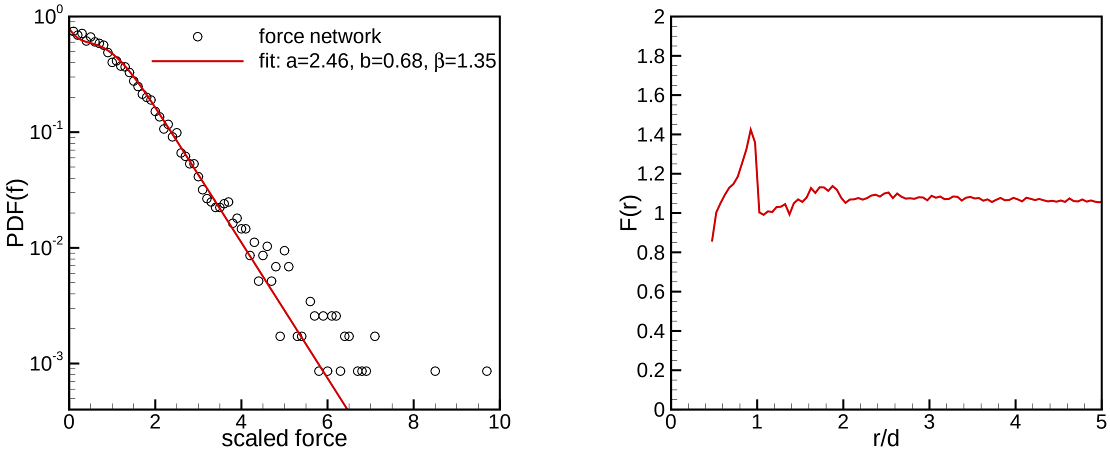

(a)

(b)

Figure 6.12 (Color online) (a) Probability densities for normal contact force based on all contacts from the computed data (open circles) and fitted with Eq. 6.11 (solid line) using $a = 2.46$, $b = 0.68$, and $\beta = 1.35$. (b) Force correlation function constructed from all contact forces.

with the aim of characterizing the force correlation length. The spatial force-force correlation function $\mathcal{F}(r)$ measures spatial correlations between forces separated by a distance r. We use the same definition as in Refs. (Mueth et al., 1998; Silbert et al., 2002b):

$$\mathcal{F}(r) \equiv \frac{\sum_i \sum_{j>i} \delta(r_{ij} - r) f_i f_j}{\sum_i \sum_{j>i} \delta(r_{ij} - r)}, \tag{6.12}$$

where r_{ij} is the distance between particle contacts i and j, and f_i is the normalized contact force acting at contact i. Note that this isotropic expression for the radial spatial force correlation formulation is not strictly applicable to the anisotropic system of finite size that is considered in this paper. However, the result for r smaller than the radius of the granular column still gives some insight to the force correlations. The result at $T = 10$ for $\mu_{\text{wall}} = 0.5$ produces peaks around $r = d_0$ and dies out after 3 d_0 as shown in Fig. 6.12(b), indicating a diffusive nature of the force transmission network. This behavior is again similar to the force correlation in a granular packing (Silbert et al., 2002b). It is interesting to note that the force correlation length scale is much smaller than the geometric contact length scale of $52.2\,d_0$.

6.3.3 Minimum spanning tree

As shown in section 6.3.2, there are force networks and structures existing in this Brazil nut problem. It is difficult to directly represent this structural information in a continuum model for the stress tensor. We explore the possibility of using a numerical algorithm based on particle position information to capture the microstructures and provide structural information in a statistical sense, i.e., we seek to determine if a representative sub-ensemble of the particles can capture the important statistics of the force network and if there is a convergent procedure to determine this representative sub-ensemble. We show that a modified minimum spanning tree (MST) approach is indeed capable of achieving this goal.

Constructing an Euclidean MST (EMST) on N particles requires connecting every particle with at least one neighbor particle through an edge (an unordered pair of particles). Since every particle is connected in the EMST it possesses the spanning property. A tree is a set of edges that contains no closed loops or cycles; i.e., starting from a particle and tracing an alternating sequence of edges between particles does not lead back to the initial particle. Finally, since it is a Euclidean minimum spanning tree, the sum of the Euclidean lengths of these edges is a minimum. A formal graph-theoretic definition of a minimum spanning tree (MST) and algorithms for constructing an MST can be found in the literature (Aho et al., 1983; Preparata and Shamos, 1985). The minimum spanning tree has been previously employed in a mixing model for turbulent reactive flows, where it was constructed on an ensemble of particles in composition space to provide a definition of localness (Subramaniam and Pope, 1998).

An example of constructing the MST based on particle positions is illustrated in Fig. 6.13, where particle 1, particle 2 and particle 3 are all in contact with each other, while particle 4 and particle 5 are in contact with each other but not with the others. Let the length of the edges be the distance between the centers of two particles in Euclidean space. If the length E(1, 3) of the edge between particle 1 and particle 3 is greater than E(1, 2) or E(2, 3) due to difference in normal compression at contact, then the resulting MST is shown in Fig. 6.13(a) by the lines connecting the centers of particles. If the lengths of E(1, 2), E(1, 3) and E(2, 3) equal each other, then any two of the these three edges can be selected in the MST, which in

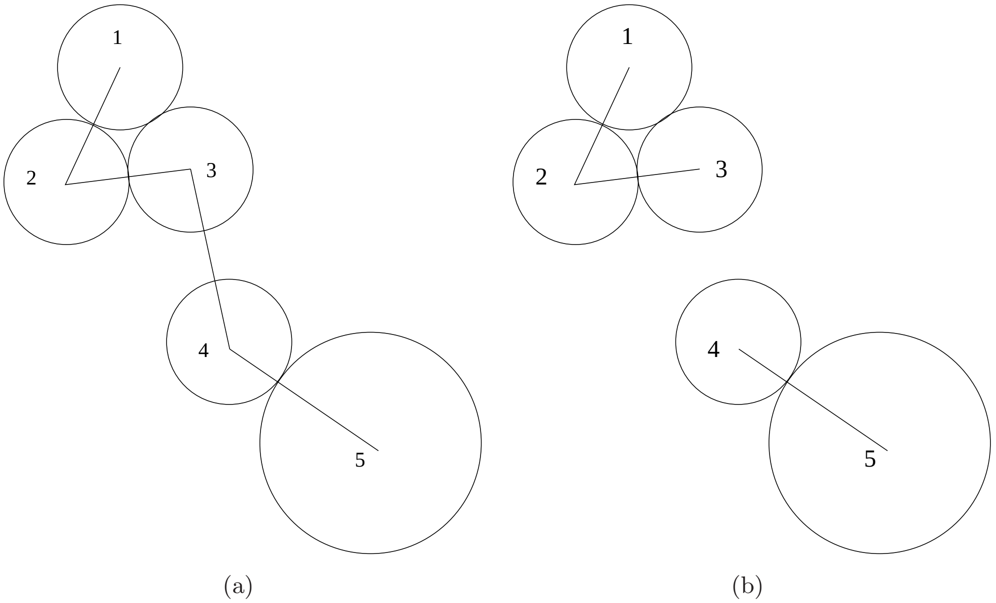

Figure 6.13 Schematics of the MST constructed based on (a) particle positions and (b) the sub-trees after deleting edges between non–contacting particles. The particles are represented by circles and the edges are shown by the lines connecting centers of particles.

this case is non–unique.

Not all the edges in the MST correspond to the force network. Since particle 3 and particle 4 are not in contact, E(3, 4) does not contribute to the normal contact force statistics, and is deleted when studying the force statistics produced from the MST. As shown in Fig. 6.13(b), deleting E(3, 4) from the MST results in two sub-trees of contacting particles. A tree of contacting particles (TCP) is defined by the number of contacting particles N_P and the set of N_E edges that define the contacts between the particles. Therefore, the TCPs contain important particle configuration information: how many particles N_P are in a force network, and which particles are connected (from the set of edges). From the MST we recover information relevant to the force networks by deleting non–contacting edges and identifying the resulting TCPs as the force networks.

As the first step toward applying the MST, we will show that the MST constructed on the particle positions can capture the majority of structural information pertaining to force networks within granular media. Then using a multi-pass MST technique, we show that almost all the contacts can be recovered from MST in just a few passes, and so can the force statistics.

Due to the minimum spanning property of a MST, at least one contact for a particle can be captured in the MST if there exist contacts for that particle in monodispersed particle configurations. If the MST is formed on all the particles and the non-contacting edges are deleted to form the TCP's, it is shown in the row corresponding to the first pass of Table 6.2 that the number of particles, N_{P} in the largest TCP and number of other TCPs, N_{T}, are exactly the same as those from the MD force network. The distribution of TCPs with respect to the number of particles in a TCP can also be shown to be exactly the same as that obtained from the MD force networks. The MST can thus predict the geometric length scale present in a force network, such as the maximum distance between two particles in a TCP or a force network. This length scale is 52.2 d_0 for the largest TCP or the largest force network. However, the MST does not capture all the particle contacts in the TCPs. Since there is no closed loop in a MST, some edges forming a closed loop in a force network are neglected. Since the MST cannot capture multiple contacts in a single pass (cf. Fig. 6.13(b) where only two of the three contacting edges for particle 1, 2 and 3 are selected by the MST algorithm), the number of edges N_E in the first pass of the MST [6] is only 5795, as compared to the 11533 edges in the MD force network (see Table 6.2).

To capture all the edges in a force network, a multi-pass MST technique is proposed. A second pass of MST is constructed by preferentially weighting edges that have already been selected in previous passes of MST. The lengths of the edges selected in previous passes are elongated by a specified factor in this case. Referring to the example shown in Fig. 6.13, the edge E(1, 3) is not selected in the first pass. A second pass of MST is constructed on the same particles after elongating the lengths of previously selected edges E(1, 2), E(2, 3) and E(4, 5) by a factor of 1.2. In this way, the edge E(1, 3) will be selected in the second pass of the MST. As shown in Table 6.2, the one-pass MST captured 5795 edges for the largest MST and 106 edges for the other TCPs, although there are a total of 11533 edges in the largest force network. The two-pass MST captured more than 90% of total edges (repeated edges are

---

[6] An MST on N_P particles will always have $N_P - 1$ edges.

Table 6.2 Number of edges and TCPs captured by MST and comparison with all force networks from MD.

Passes	The largest TCP		The rest of TCPs	
	N_P	N_E	N_T	N_E
1	5796	5795	79	106
2	5796	10505	79	106
3	5796	11508	79	106
4	5796	11515	79	106
5	5796	11516	79	106
Force networks	5796	11533	79	106

not counted). The number of edges, N_E, in the largest TCP captured by the multi-pass MST increases with increasing number of passes, as shown in Table 6.2, and rapidly converges to the total number of edges in the MD force network. In fact, all the edges have been recovered by a four-pass MST except 18 edges connecting the large particle, which are much longer than other edges and difficult to capture using the current multi-pass MST algorithm. Note that the number of particles in the largest TCP stays the same since this information is faithfully captured by the one-pass MST as discussed before.

Assigning the forces from the force networks to the corresponding edges in the MST, we can determine how well the MST captures force statistics. The force PDF obtained from the MST is compared with that obtained from the force networks in Fig. 6.14. It can be seen that most of the forces in the one-pass MST are larger than the mean force due to the minimum spanning property. This is indicated by higher probabilities for the larger force and lower probabilities for the smaller-than-mean forces. The one-pass MST also preserves the exponential decay for larger force values.

The force distributions generated by various passes of MST are also fitted to quantitatively demonstrate these statistical characteristics. We find that the PDF can be fitted with a functional form

$$P(f) = a(1 - be^{-(f-\alpha)^2})e^{-\beta(f-\gamma)}. \tag{6.13}$$

We fit the forces captured by the one-pass MST using $\alpha = \gamma = 0.45$ and the same values of a, b and β as those used for fitting the forces in the force networks. This fitting indicates that the force PDF for MST is shifted toward larger forces by the magnitudes of α and γ. It is

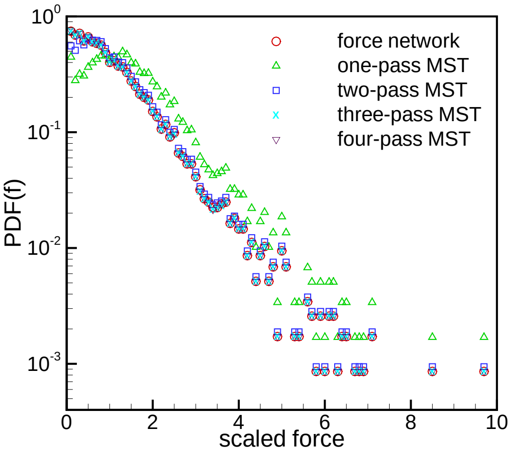

Figure 6.14 (Color online) Probability densities for normal contact forces based on all contacts (force networks) and constructed from multi-pass MST. The PDF of all contact forces is overlapped by the multi-pass MST results; however, it can also be seen in Fig. 6.12(a) for clarity.

shown in Fig. 6.15(a) that the exponential decay for the larger forces is fitted well while the smaller forces have smaller probabilities compared with the fitting. This result means that the one-pass MST over-sampled larger forces, but with the same decay rate compared to the force distribution in the force networks. Furthermore, we find that Eq. 6.13 fits the whole range of forces well with $a = 2.2$, $b = 0.9$, $\beta = 1.35$, $\alpha = 0.25$, and $\gamma = 0.5$, which is demonstrated in the inset of Fig. 6.15(a). The two-pass, three-pass and four-pass MST quickly converge to the PDF from the force networks, with almost no distinction between them after three passes. The fit to the two-pass MST force PDF is done using $\alpha = \gamma = 0.1$ to shift the fitted force networks PDF and shows good agreement for the larger forces in Fig. 6.15(b). Similarly, Eq. 6.13 with $a = 3.1$, $b = 0.8$, $\beta = 1.35$, $\alpha = -0.1$, and $\gamma = -0.1$ fits the whole range of forces well as shown in the inset of Fig. 6.15(b). For the three-pass and four-pass MST PDF, the fitted force networks PDF also fits well, i.e., $\alpha = \gamma = 0$. Overall, α and γ decrease to zero with the increasing of number of MST passes and thus Eq. 6.13 recovers to Eq. 6.11, which shows the multi-pass MST is a convergent procedure to capture forces in the force networks. The same convergence was found for the force correlation functions as shown in Fig. 6.16. Thus

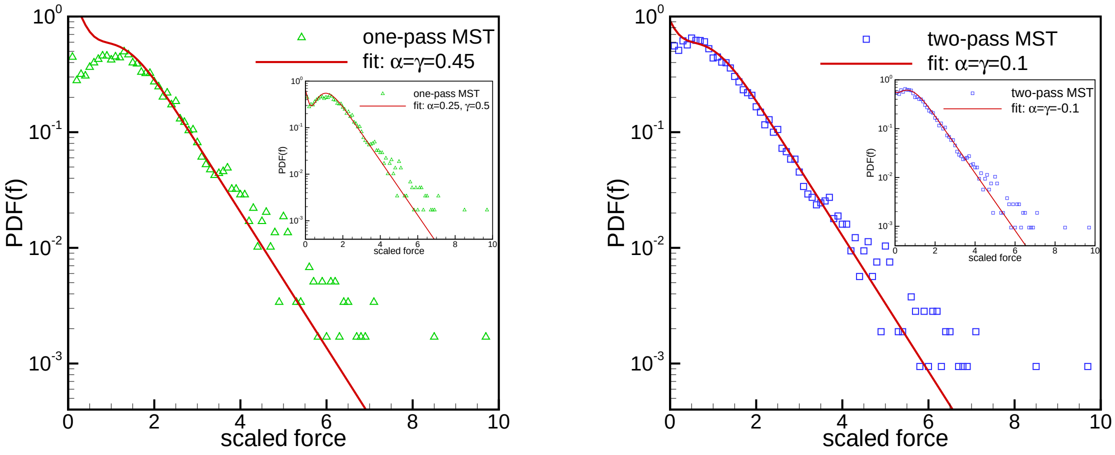

(a)

(b)

Figure 6.15 (Color online) (a) Probability densities for normal contact force based on the contacts from the one-pass MST(open triangles) and fitted with Eq. 6.13 (solid line) using $a = 2.46$, $b = 0.83$, $\beta = 1.35$, $\alpha = 0.45$, and $\gamma = 0.45$. Inset: the one-pass MST data is fitted with Eq. 6.13 (solid line) using $a = 2.2$, $b = 0.9$, $\beta = 1.35$, $\alpha = 0.25$, and $\gamma = 0.5$. (b) Probability densities for normal contact force based on the contacts from the two-pass MST(open squires) and fitted with Eq. 6.13 (solid line) using $a = 2.46$, $b = 0.83$, $\beta = 1.35$, $\alpha = 0.1$, and $\gamma = 0.1$. Inset: the two-pass MST data is fitted with Eq. 6.13 (solid line) using $a = 3.1$, $b = 0.8$, $\beta = 1.35$, $\alpha = -0.1$, and $\gamma = -0.1$.

the modified MST algorithm is able to recover particle configuration information as well as statistics and spatial correlation of the normal contact forces.

6.4 Conclusions

We have performed MD simulations of the BNP at low vibration frequency in order to understand the underlying physical mechanisms of segregation dynamics. Systematic variation of the particle properties and external wall friction reveals that the large particle rising is not sensitive to particle stiffness, interaction force models, interstitial air effects, slight polydispersity in small particles, or particle friction. However, the rise time is very sensitive to external wall friction. We conclude that wall friction is the most important physical parameter in deter-

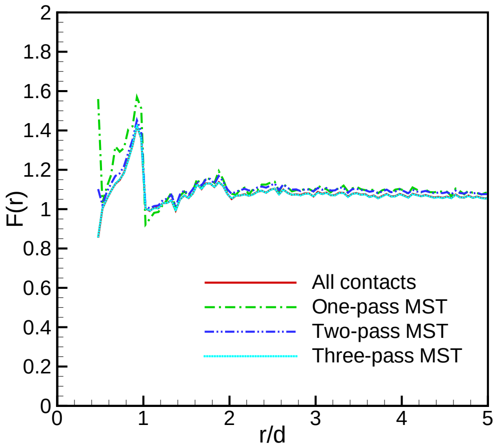

Figure 6.16 (Color online) Force correlation function constructed from all contact forces and constructed from multi-pass MST. The force correlation function of all contact forces is overlapped by the multi-pass MST results; however, it can also be seen in Fig. 6.12(b) for clarity.

mining the segregation behavior in this BNP. We also show the one-cycle dynamical response of the granular bed with wall friction ($\mu_{\text{wall}} = 0.5$), within which there is an expansion stage and a compression stage. The granular bed exhibits irregular oscillation without wall friction ($\mu_{\text{wall}} = 0.0$).

We found the presence of large-scale force networks bearing larger-than-average forces in the compression stage with wall friction, while there are much fewer contacts in the expansion stage. However, without wall friction such large strong force networks do not exist. We analyzed the force network by comparing the PDF of normal contact forces and found exponential tails similar to those found in packing experiments. We further analyzed the two-point force correlation of the force network and found force correlations decay quickly. The fact that the length scale over which the normal force is correlated is only two to three particle diameters, whereas the geometric contacts extend over 50 d_0 (the size of the system), indicates that a local interaction model for the force on a particle is adequate. However, the large length scale of geometric contact appears to be essential for transmission of the effect of wall friction. Therefore, one can conclude that the geometric length scale indicates the nature of the material response: if it is small, the particle behaves like an isolated free body, if it is large, the granular material behaves like a continuum composed of grain skeletons. Yet, even this continuum can admit a local force or stress model because of the short-range nature of the contact force.

Finally, we applied the Euclidean minimum spanning tree to analyze the force network, and explored the possibility of using MST based on particle position information to capture the microstructures and provide structural information in a statistical sense. We showed that the MST is able to capture the complete structural information. We developed a multi-pass MST algorithm, which was able to recover all the contacts within the force network and thus was able to recover the force distribution and force correlation for the force network. Therefore, the MST provides a possible route to constructing a continuum model with microstructural information supplied from this algorithm.

CHAPTER 7. HYBRID TWO-FLUID DEM SIMULATION OF GAS-SOLID FLUIDIZED BEDS

A paper submitted to *Journal of Fluids Engineering*[1]

Jin Sun, Francine Battaglia and Shankar Subramaniam

Abstract

Simulations of gas-solid fluidized beds have been carried out using a hybrid simulation method, which couples the discrete element method (DEM) for particle dynamics with the averaged two-fluid (TF) equations for the gas phase. The coupling between the two phases is modeled using an interphase momentum transfer term. The results of the hybrid TF-DEM simulations are compared to experimental data and two-fluid model simulations. It is found that the TF-DEM simulation is capable of predicting general fluidized bed dynamics, i.e., pressure drop across the bed and bed expansion, which are in agreement with experimental measurements and two-fluid model predictions. Multi-particle contacts and large contact forces are found in the defluidized regions away from bubbles as demonstrated from the TF-DEM simulation results. The TF-DEM model demonstrates the capability to capture more heterogeneous structural information of the fluidized beds than the TF model alone. The implications to the solid phase constitutive closures for TF models are discussed. However, the TF-DEM simulations depend on the form of the interphase momentum transfer model, which can be computed in terms of averaged or instantaneous particle quantities. Various forms of the interphase momentum transfer model are examined, and simulation results from these models are compared.

---

[1] Under the second review.

Nomenclature

$\mathbf{C}$	Fluctuation in particle translational velocity	(cm/s)
d	Particle diameter	(cm)
e	Coefficient of normal restitution	
$\mathbf{g}$	Acceleration of gravity	(cm/s^2)
I	Moment of inertia of a particle	(g $\cdot$ cm^2)
$\mathbf{I}$	Interphase momentum transfer	(dyne/cm^3)
J_{coll}	Rate of dissipation of translational fluctuation kinetic energy due to particle collisions	(g/cm $\cdot$ s^3)
J_{vis}	Rate of dissipation of translational fluctuation kinetic energy due to interstitial gas viscous damping	(g/cm $\cdot$ s^3)
k	Stiffness coefficient of a particle	(dyne/cm)
m	Mass of a particle	(g)
$\mathbf{n}$	Unit normal vector from a boundary to particles	
N	Particle number	
N_{c}	Coordination number	
N_{g}	Total number of gas phase chemical species	
N_{sm}	Total number of solid phase (m) chemical species	
P	Pressure	(dyne/cm^2)
$\mathbf{r}$	Position vector	(cm)
R	Rate of formation	(g/cm^3 $\cdot$ s)
Re	Reynolds number	
$\overline{\overline{S}}$	Stress tensor	(dyne/cm^2)
t	Time	(s)
U	Fluidization velocity	(cm/s)
$\mathbf{u}$	Tangential displacement	(cm)
$\mathbf{v}$	Velocity for gas and solids	(cm/s)

Greek letters

β	Coefficient for drag forces	$(\mathrm{g/cm^3 \cdot s})$
δ	Normal compression in particle collision	(cm)
ε	Volume fraction	
γ	Viscous damping coefficient	(1/s)
Γ	Rate of dissipation of rotational fluctuation kinetic energy	$(\mathrm{g/cm \cdot s^3})$
Γ_{slip}	Production of translational fluctuation kinetic energy due to gas-particle slip	$(\mathrm{g/cm \cdot s^3})$
μ	Coefficient of friction in DEM	
μ_{g}	Gas shear viscosity	$(\mathrm{dyne \cdot s/cm^2})$
μ_{sm}	Solid shear viscosity	$(\mathrm{dyne \cdot s/cm^2})$
λ_{g}	Gas second coefficient of viscosity	$(\mathrm{dyne \cdot s/cm^2})$
λ_{sm}	Solid second coefficient viscosity	$(\mathrm{dyne \cdot s/cm^2})$
ω	Angular velocity	(rad/s)
ρ	Density	$(\mathrm{g/cm^3})$
θ	Translational granular temperature	$(\mathrm{cm^2/s^2})$

Superscripts

p	Plastic regime in granular flows
v	Viscous regime in granular flows

Subscripts

cell	Computational cell
coll	Collision
g	Gas phase
i	Index of a particle
l	l^{th}solid phase

m	m^{th}solid phase
n	Normal direction in the particle contact frame
t	Tangential direction in the particle contact frame
M	Number of phases
mf	Minimum fluidization
max	Maximum value
p	Particle
s	Solid phase
w	Wall boundary

7.1 Introduction

Gas-solid fluidized beds are widely used in many industrial applications, e.g., fluid catalytic cracking, due to its good contacting between gas and solid phases, which prompts rapid heat and mass transfer and fast chemical reactions. However, the dynamics of gas-solid fluidized beds need to be better understood in order to improve existing processes and scale up new processes. Reliable simulation tools can provide valuable insights into gas-solid flow processes and, as a result, accelerate the achievement of substantial process improvements (Curtis and van Wachem, 2004).

The dynamics of fluidized beds can be described at different levels of details (Jackson, 2000). At the most fundamental level (atomic or molecular scale is not considered), the motion of the whole system is determined by the Newtonian equations of motion for the translation and rotation of each particle, and the fluid Navier-Stokes and continuity equations. The fluid motion and particle motion are linked by the no-slip condition on each particle boundary. At a second level, the fluid velocity at each point is replaced by its average, taken over a spatial domain large enough to contain many particles but still small compared to the whole region occupied by the flowing mixture. The Newtonian equations of motion are solved for each particle. The coupling force between fluid and particles is then related to the particle's velocity relative to the locally averaged fluid velocity, and to the local concentration of the particle assembly. At a third level, both the fluid velocity and the particle velocity are averaged over the local spatial domains. A description at this level of detail is often referred as the two fluid model (TFM).

The kinetic theory of granular flows (KTGF) has been successful applied to the TFM for fluidization in the last decade (Gidaspow et al., 2004). The KTGF has a basic assumption that particle collisions are instantaneous and binary. However, questions about the validity and capability of KTGF arise because of the microstructures formed in the fluidized beds, e.g., clusters in a riser (Agrawal et al., 2001) and "defluidized" zones in a bubbling fluidized bed (Rahman and Campbell, 2002). In a dense bubbling fluidized bed, the particle pressure around a bubble was experimentally measured and shown to be large in the region far below the bubble where there is no agitation (Rahman and Campbell, 2002). These facts lead to the hypothesis that lasting multiple contacts in dense fluidized beds limit the application of KTGF. Previous experiments (Choi et al., 2004) and models (Bazant, 2003, 2006) also showed that diffusion and mixing are dominated by geometry, consistent with long-lasting contacts (but not thermal collisions) in dense granular flows.

However, there has not yet been quantitative analysis to assess multi-particle microstructures under certain fluidization conditions, and how the microstructures affect the constitutive behavior of a dense fluidized bed. A good understanding of the spatial distribution and temporal evolution of multi-particle contacts and corresponding particle contact forces is a necessary step toward developing constitutive models that can accurately predict fluidized bed dynamics. In this paper, a hybrid model at the second level will be employed to improve the understanding. The hybrid model couples a two fluid model solving fluid equations with the discrete element method (DEM) solving particle motion equations. Therefore, the hybrid model can simulate a fluidized bed at particle scales and produce useful information to analyze the microstructures as well as particle dynamics. The computational results from the hybrid model will be compared with experimental and TFM results for the validation purpose.

A key consideration in the hybrid model is the coupling between the phases, i.e., the fluid-particle interaction force. Different formulations have been used to calculate and transfer the force between phases (Tsuji et al., 1993; Hoomans et al., 1996; Xu and Yu, 1997; Kafui et al., 2002). However, formulations have not been thoroughly analyzed for different flow conditions. In this paper, two different ways to transfer the effective drag force, an important coupling term between gas and particles, will be discussed and simulation results from these two methods will be compared.

7.2 Methodology

7.2.1 Multi-fluid Model

The multi-fluid Eulerian model describes the gas phase and solid phases as interpenetrating continua. The particle mixture is divided into a discrete number of phases, each of which can have different physical properties, e.g., particle diameter. It should be noted that the two fluid model for a gas phase and single solid phase is a special case, $m = 1$, for the general formula presented next. The governing equations for the multi-fluid model are (Syamlal et al., 1993):

Continuity equation for gas phase:

$$\frac{\partial}{\partial t}(\varepsilon_{\mathrm{g}}\rho_{\mathrm{g}}) + \boldsymbol{\nabla}\cdot(\varepsilon_{\mathrm{g}}\rho_{\mathrm{g}}\mathbf{v}_{\mathrm{g}}) = \sum_{n=1}^{N_{\mathrm{g}}} R_{\mathrm{g}n}. \tag{7.1}$$

Continuity equation for m^{th} solid phase:

$$\frac{\partial}{\partial t}(\varepsilon_{\mathrm{s}m}\rho_{\mathrm{s}m}) + \boldsymbol{\nabla}\cdot(\varepsilon_{\mathrm{s}m}\rho_{\mathrm{s}m}\mathbf{v}_{\mathrm{s}m}) = \sum_{n=1}^{N_{\mathrm{s}m}} R_{\mathrm{s}mn}. \tag{7.2}$$

Momentum equation for gas-phase:

$$\frac{\partial}{\partial t}(\varepsilon_{\mathrm{g}}\rho_{\mathrm{g}}\mathbf{v}_{\mathrm{g}}) + \boldsymbol{\nabla}\cdot(\varepsilon_{\mathrm{g}}\rho_{\mathrm{g}}\mathbf{v}_{\mathrm{g}}\mathbf{v}_{\mathrm{g}}) = \boldsymbol{\nabla}\cdot\overline{\overline{S}}_{\mathrm{g}} + \varepsilon_{\mathrm{g}}\rho_{\mathrm{g}}\mathbf{g} - \sum_{m=1}^{M}\mathbf{I}_{\mathrm{g}m}. \tag{7.3}$$

Momentum equation for m^{th} solid-phase:

$$\begin{aligned}&\frac{\partial}{\partial t}(\varepsilon_{\mathrm{s}m}\rho_{\mathrm{s}m}\mathbf{v}_{\mathrm{s}m}) + \boldsymbol{\nabla}\cdot(\varepsilon_{\mathrm{s}m}\rho_{\mathrm{s}m}\mathbf{v}_{\mathrm{s}m}\mathbf{v}_{\mathrm{s}m}) = \\ &\boldsymbol{\nabla}\cdot\overline{\overline{S}}_{\mathrm{s}m} + \varepsilon_{\mathrm{s}m}\rho_{\mathrm{s}m}\mathbf{g} + \mathbf{I}_{\mathrm{g}m} - \sum_{\substack{l=1\\ l\neq m}}^{M}\mathbf{I}_{ml}.\end{aligned} \tag{7.4}$$

Translational granular temperature equation (Agrawal et al., 2001):

$$\frac{3}{2}\left[\frac{\partial}{\partial t}(\varepsilon_{sm}\rho_{sm}\theta_{sm,\mathrm{t}}) + \boldsymbol{\nabla}\cdot(\varepsilon_{sm}\rho_{sm}\theta_{sm,\mathrm{t}}\mathbf{v}_{sm})\right] =$$
$$-\boldsymbol{\nabla}\cdot\mathbf{q}_{sm} - \overline{\overline{S}}_{sm}\colon \boldsymbol{\nabla}\mathbf{v}_{sm} + \gamma_{sm,\mathrm{slip}} - J_{sm,\mathrm{coll}} - J_{sm,\mathrm{vis}}, \tag{7.5}$$

where the translational granular temperature is defined as:

$$\theta_{sm,\mathrm{t}} = \frac{1}{3} < C_{\mathrm{p}i}^2 > . \tag{7.6}$$

The fluctuation in the particle translational velocity shown in Eq. (7.6) is defined as $\mathbf{C}_{\mathrm{p}i} = \mathbf{v}_{\mathrm{p}i} - \mathbf{v}_{sm}$, where $\mathbf{v}_{\mathrm{p}i}$ is the instantaneous translational particle velocity and the symbol <> designates the operation of taking average.

The constitutive equations for solid phases were derived for granular flows (Syamlal, 1987a). There are two distinct flow regimes in granular flows: a viscous or rapidly shearing regime in which stresses arise due to collisional or translational momentum transfer, and a plastic or slowly shearing regime in which stresses arise due to Coulomb friction between grains in close contact. Two different approaches are used for these regimes

$$\overline{\overline{S}}_{sm} = \begin{cases} -P_{sm}^{\mathrm{p}}\overline{\overline{I}} + \overline{\overline{\tau}}_{sm}^{\mathrm{p}} & \text{if } \varepsilon_{\mathrm{s}} \geq \varepsilon_{\mathrm{s}}^* \\ -P_{sm}^{\mathrm{v}}\overline{\overline{I}} + \overline{\overline{\tau}}_{sm}^{\mathrm{v}} & \text{if } \varepsilon_{\mathrm{s}} < \varepsilon_{\mathrm{s}}^* \end{cases} \tag{7.7}$$

where P_{sm}^{p} and $\overline{\overline{\tau}}_{sm}^{\mathrm{p}}$ are the pressure and the viscous stress in the m^{th} solids phase for the plastic regime, P_{sm}^{v} and $\overline{\overline{\tau}}_{sm}^{\mathrm{v}}$ are the pressure and the viscous stress for the viscous regime, and $\varepsilon_{\mathrm{g}}^*$ is a critical packing solid volume fraction, set to 0.58 for the simulations in this paper.

The granular stress equation based on KTGF (Syamlal, 1987b) is applied to the viscous regime. The granular pressure and stresses are given by

$$P_{sm}^{\mathrm{v}} = K_{1m}\varepsilon_{sm}^2\theta_{sm,\mathrm{t}}, \tag{7.8}$$

$$\overline{\overline{\tau}}_{sm}^{\mathrm{v}} = 2\mu_{sm}^{\mathrm{v}}\overline{\overline{D}}_{sm} + \lambda_{sm}^{\mathrm{v}}\mathrm{tr}(\overline{\overline{D}}_{sm})\overline{\overline{I}}, \tag{7.9}$$

where $\lambda_{sm}^{\mathrm{v}}$ is the second coefficient of viscosity,

$$\lambda_{sm}^{\mathrm{v}} = K_{2m}\varepsilon_{sm}\sqrt{\theta_{sm,\mathrm{t}}} . \tag{7.10}$$

The shear viscosity factor μ_{sm}^{v} is

$$\mu_{sm}^{\mathrm{v}} = K_{3m}\varepsilon_{sm}\sqrt{\theta_{sm,\mathrm{t}}}\ . \tag{7.11}$$

The strain rate tensor, $\overline{\overline{D}}_{sm}$, is given by

$$\overline{\overline{D}}_{sm} = \frac{1}{2}\left[\nabla\mathbf{v}_{sm} + (\nabla\mathbf{v}_{sm})^{\mathrm{T}}\right]. \tag{7.12}$$

The coefficients, K_{1m}, K_{2m} and K_{3m} are functions of particle density, diameter, restitution coefficient, radial distribution function and local volume fractions. The solid stress tensor in the viscous regime only takes account of contributions from particle translational momentum flux and binary collisions.

In the plastic flow regime, the solid stress tensor was derived based on plastic flow theory (Jenike, 1987) and critical state theory (Schaeffer, 1987).

The constitutive equation for the gas phase stress tensor is:

$$\overline{\overline{S}}_{\mathrm{g}} = -P_{\mathrm{g}}\overline{\overline{I}} + \overline{\overline{\tau}}_{\mathrm{g}}, \tag{7.13}$$

where P_{g} is the gas pressure and $\overline{\overline{I}}$ is the identity tensor. The viscous stress tensor $\overline{\overline{\tau}}_{\mathrm{g}}$ is assumed to be of the Newtonian form:

$$\overline{\overline{\tau}}_{\mathrm{g}} = 2\mu_{\mathrm{g}}\overline{\overline{D}}_{\mathrm{g}} + \lambda_{\mathrm{g}}\boldsymbol{\nabla}\cdot\mathbf{v}_{\mathrm{g}}, \tag{7.14}$$

where $\overline{\overline{D}}_{\mathrm{g}}$ is the strain rate tensor for the gas phase. The gas-solid momentum transfer ($\mathbf{I}_{\mathrm{g}m}$) will be discussed in the subsection on coupling TFM and DEM.

7.2.2 Discrete Element Method

Individual particle motion in a fluidized bed can be described by Newtonian equations of motion. The discrete element method employs numerical integration of the motion equations to resolve particle trajectories (Cundall and Strack, 1979). The translational and rotational motions of a particle are governed by:

$$m_i\frac{\mathrm{d}\mathbf{v}_{\mathrm{p}i}}{\mathrm{d}t} = \mathbf{f}_{\mathrm{c}i} + \mathbf{f}_{\mathrm{gp}i} + m_i\mathbf{g}, \tag{7.15}$$

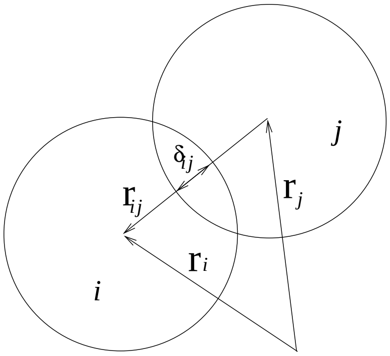

Figure 7.1 Schematic of two particles i and j in contact and position vectors $\mathbf{r}_i$, $\mathbf{r}_j$, respectively, with overlap δ_{ij}

$$I_i \frac{\mathrm{d}\boldsymbol{\omega}_i}{\mathrm{d}t} = \mathbf{T}_i, \tag{7.16}$$

where $\mathbf{f}_{ci}$ is the particle-particle contact force, $\mathbf{f}_{\mathrm{gp}i}$ is the fluid-particle interaction force, $m_i\mathbf{g}$ is the gravitational force, $\mathbf{T}_i$ is the torque arising from the tangential components of the contact force, and I_i, $\mathbf{v}_{\mathrm{p}i}$, $\boldsymbol{\omega}_i$ are the moment of inertia, linear velocity and angular velocity, respectively. The net contact force, $\mathbf{f}_{ci}$, and torque, $\mathbf{T}_i$, acting on each particle result from a vector summation of the force and torque at each particle-particle contact. A linear spring-dashpot model is employed for the contact force model due to its simplicity and reasonable accuracy (Cundall and Strack, 1979). The basic principles of the linear spring-dashpot model are briefly described in the following.

For two contacting particles $\{i,\, j\}$, with radii $\{a_i,\, a_j\}$, at positions $\{\mathbf{r}_i,\, \mathbf{r}_j\}$, with velocities $\{\mathbf{v}_i,\, \mathbf{v}_j\}$ and angular velocities $\{\boldsymbol{\omega}_i,\, \boldsymbol{\omega}_j\}$ (see Fig. 7.1), the normal compression δ_{ij}, relative normal velocity $\mathbf{v}_{\mathrm{n}_{ij}}$, and relative tangential velocity $\mathbf{v}_{\mathrm{t}_{ij}}$ are (Silbert et al., 2001):

$$\delta_{ij} = d - r_{ij}, \tag{7.17}$$

$$\mathbf{v}_{\mathrm{n}_{ij}} = (\mathbf{v}_{ij} \cdot \mathbf{n}_{ij})\mathbf{n}_{ij}, \tag{7.18}$$

$$\mathbf{v}_{\mathrm{t}_{ij}} = \mathbf{v}_{ij} - \mathbf{v}_{n_{ij}} - (a_i\boldsymbol{\omega}_i + a_j\boldsymbol{\omega}_j) \times \mathbf{n}_{ij}, \tag{7.19}$$

where $d = a_i + a_j$, $\mathbf{r}_{ij} = \mathbf{r}_i - \mathbf{r}_j$, $\mathbf{n}_{ij} = \mathbf{r}_{ij}/r_{ij}$, with $r_{ij} = |\mathbf{r}_{ij}|$ and $\mathbf{v}_{ij} = \mathbf{v}_i - \mathbf{v}_j$. The rate of change of the elastic tangential displacement $\mathbf{u}_{\mathrm{t}_{ij}}$, set to zero at the initiation of a contact is:

$$\frac{\mathrm{d}\mathbf{u}_{\mathrm{t}_{ij}}}{\mathrm{d}t} = \mathbf{v}_{\mathrm{t}_{ij}} - \frac{(\mathbf{u}_{\mathrm{t}_{ij}} \cdot \mathbf{v}_{ij})\mathbf{r}_{ij}}{r_{ij}^2}. \tag{7.20}$$

The last term in Eq. (7.20) arises from the rigid body rotation around the contact point and ensures that $\mathbf{u}_{\mathrm{t}_{ij}}$ always lies in the local tangent plane of contact. Normal and tangential forces acting on particle i are:

$$\mathbf{F}_{\mathrm{n}_{ij}} = f(\delta_{ij}/d)(k_{\mathrm{n}}\delta_{ij}\mathbf{n}_{ij} - \gamma_{\mathrm{n}} m_{\mathrm{eff}} \mathbf{v}_{\mathrm{n}_{ij}}), \tag{7.21}$$

$$\mathbf{F}_{\mathrm{t}_{ij}} = f(\delta_{ij}/d)(-k_{\mathrm{t}}\mathbf{u}_{\mathrm{t}_{ij}} - \gamma_{\mathrm{t}} m_{\mathrm{eff}} \mathbf{v}_{\mathrm{t}_{ij}}), \tag{7.22}$$

where $k_{\mathrm{n,t}}$ and $\gamma_{\mathrm{n,t}}$ are the spring stiffness and viscoelastic constants, respectively, and $m_{\mathrm{eff}} = m_i m_j/(m_i + m_j)$ is the effective mass of spheres with masses m_i and m_j. The corresponding contact force on particle j is simply given by Newton's third law, i.e., $\mathbf{F}_{ji} = -\mathbf{F}_{ij}$. The function $f(\delta_{ij}/d) = 1$ is for the linear spring-dashpot model, and $f(\delta_{ij}/d) = \sqrt{\delta_{ij}/d}$ is for Hertzian contacts with viscoelastic damping between spheres.

Static friction is implemented by keeping track of the elastic shear displacement throughout the lifetime of a contact. The static yield criterion, characterized by a local particle friction coefficient μ, is modeled by truncating the magnitude of $\mathbf{u}_{\mathrm{t}_{ij}}$ as necessary to satisfy $|\mathbf{F}_{\mathrm{t}_{ij}}| < |\mu \mathbf{F}_{\mathrm{n}_{ij}}|$. Thus the contact surfaces are treated as "sticking" when $|\mathbf{F}_{\mathrm{t}_{ij}}| < |\mu \mathbf{F}_{\mathrm{n}_{ij}}|$, and as "slipping" when the yield criterion is satisfied.

The total contact force and torque acting on particle i are then given by

$$\mathbf{f}_{\mathrm{c}i} = \sum_j (\mathbf{F}_{\mathrm{n}ij} + \mathbf{F}_{\mathrm{t}ij}), \tag{7.23}$$

$$\mathbf{T}_i = -\frac{1}{2}\sum_j \mathbf{r}_{ij} \times \mathbf{F}_{\mathrm{t}ij}. \tag{7.24}$$

The amount of energy lost in collisions, characterized by the inelasticity through the value of the coefficient of restitution e, which is defined as the negative ratio of the particle velocity after collision to the velocity before collision. For the linear spring-dashpot model, the coefficient of normal restitution and contact time can be analytically obtained:

$$e_{\mathrm{n}} = \exp(-\gamma_{\mathrm{n}} t_{\mathrm{c}}/2), \tag{7.25}$$

where the contact time t_c is given by:

$$t_\mathrm{c} = \pi(k_\mathrm{n}/m_\mathrm{eff} - \gamma_\mathrm{n}^2/4)^{-1/2}. \tag{7.26}$$

The value of the spring constant should be large enough to avoid particle interpenetration, yet not so large as to require an unreasonably small simulation time step δt, since an accurate simulation typically requires $\delta t \sim t_\mathrm{c}/50$. After the contact force is calculated, the equations of motion, which are ordinary differential equations, can be numerically integrated to get the particle trajectories.

7.2.3 Coupling of TFM and DEM

A hybrid model at the second level is constructed by coupling the TFM for gas phase with DEM for particle motion (Boyalakuntla, 2003). The coupling term between the equations for gas and particle motion is the gas-particle interaction $\mathbf{I}_{gm}$ in the gas momentum equation and $\mathbf{f}_{\mathrm{gp}i}$ in the particle equation of motion. Due to the averaging process in the derivation of momentum equations for the TFM, the fluid-particle interaction force may be written as the sum of a component due to macroscopic variations in the fluid stress tensor and a component representing the effect of detailed variation of the point stress stress tensor as the gas flows around the particle (Anderson and Jackson, 1967). For the gas force on a particle

$$\mathbf{f}_{\mathrm{gp}i} = V_{\mathrm{p}i} \boldsymbol{\nabla} \cdot \overline{\overline{S}}_\mathrm{g} + \mathbf{f}'_{\mathrm{gp}i}, \tag{7.27}$$

where $V_{\mathrm{p}i}$ is the volume of particle i. The first term on the right in Eq. (7.27) accounts for the macroscopic variation in the fluid stress tensor. The second term on the right in Eq. (7.27) includes skin friction and drag contributions accounting for the detailed variation in the stress tensor. In general, the term comprises an effective drag force in the direction of the relative velocity between the fluid and particle, and a virtual or added mass force accounting for the resistance of the fluid mass that is moving at the same acceleration as the particle. For gas solid flows, the virtual mass force may be neglected and $\mathbf{f}'_{\mathrm{gp}i}$ reduces to an effective drag force, which should be the product of the local void fraction, ε_g, and the drag force, $\mathbf{f}_{\mathrm{d}i}$, obtained from experimentally based correlations. Also substituting Eq. (7.13) to Eq. (7.27),

$$\mathbf{f}_{\mathrm{gp}i} = -V_{\mathrm{p}i}\boldsymbol{\nabla} P_{\mathrm{g}} + V_{\mathrm{p}i}\boldsymbol{\nabla}\cdot\overline{\overline{\tau}}_{\mathrm{g}} + \varepsilon_{\mathrm{g}}\mathbf{f}_{\mathrm{d}i}. \tag{7.28}$$

The drag force on a single particle of diameter $d_{\mathrm{p}i}$ in a multi-particle system can be calculated from the correlation:

$$\begin{aligned}\mathbf{f}_{\mathrm{d}i} =& \frac{1}{2}C_{\mathrm{D}i}\rho_{\mathrm{g}}\frac{\pi d_{\mathrm{p}i}^2}{4}\varepsilon_{\mathrm{g}}^2|\mathbf{v}_{\mathrm{g}}^i - \mathbf{v}_{\mathrm{p}i}|(\mathbf{v}_{\mathrm{g}}^i - \mathbf{v}_{\mathrm{p}i})f(\varepsilon_{\mathrm{g}}) \\ =& \frac{\pi d_{\mathrm{p}i}^3}{6\varepsilon_{\mathrm{g}}\varepsilon_{sm}}\beta(\mathbf{v}_{\mathrm{g}}^i - \mathbf{v}_{\mathrm{p}i})\end{aligned} \tag{7.29}$$

where $\mathbf{v}_{\mathrm{g}}^i$ means the gas velocity at the location of particle i, and $f(\varepsilon_{\mathrm{g}})$ is a function of local void fraction. The single particle velocity $\mathbf{v}_{\mathrm{p}i}$ is used since the correlations relate the effective drag force to that of a single particle in the absence of other particles. The expressions of β are extended form the work of Ergun (Ergun, 1952), and Wen and Yu (Wen and Yu, 1966) and were used by Tsuji (Tsuji et al., 1993):

$$\beta = \begin{cases} 150\frac{\varepsilon_{sm}^2}{\varepsilon_{\mathrm{g}} d_{\mathrm{p}i}^2}\mu_{\mathrm{g}} + 1.75\varepsilon_{sm}\frac{\rho_{\mathrm{g}}}{d_{\mathrm{p}i}}|\mathbf{v}_{\mathrm{g}}^i - \mathbf{v}_{\mathrm{p}i}| & \text{for } \varepsilon_{\mathrm{g}} \le 0.8 \\ \frac{3}{4}C_{\mathrm{D}}\frac{\varepsilon_{\mathrm{g}}\varepsilon_{sm}}{d_{\mathrm{p}i}}\rho_{\mathrm{g}}|\mathbf{v}_{\mathrm{g}}^i - \mathbf{v}_{\mathrm{p}i}|\varepsilon_{\mathrm{g}}^{-2.7} & \text{for } \varepsilon_{\mathrm{g}} > 0.8. \end{cases} \tag{7.30}$$

The drag coefficient, $C_{\mathrm{D}i}$, depends on the particle Reynolds number, $\mathrm{Re}_{\mathrm{p}i} = \frac{d_{\mathrm{p}i}\varepsilon_{\mathrm{g}}|\mathbf{v}_{\mathrm{g}}^i - \mathbf{v}_{\mathrm{p}i}|\rho_{\mathrm{g}}}{\mu_{\mathrm{g}}}$, and is given by

$$C_{\mathrm{D}i} = \begin{cases} 24(1 + 0.15\mathrm{Re}_{\mathrm{p}i}^{0.687})/\mathrm{Re}_{\mathrm{p}i} & \text{for } \mathrm{Re}_{\mathrm{p}i} < 1000 \\ 0.43 & \text{for } \mathrm{Re}_{\mathrm{p}i} \ge 1000 \end{cases} \tag{7.31}$$

The fluid-particle interaction force per unit volume of bed, $\mathbf{I}_{\mathrm{g}m}$, in the gas momentum equation is obtained by summing the gas forces, $\mathbf{f}_{\mathrm{gp}i}$, over all the particles in a fluid cell and dividing by the volume of the fluid cell, V_{cell}. Thus

$$\begin{aligned}\mathbf{I}_{\mathrm{g}m} =& \frac{\sum_i^{N_{\mathrm{m}}}\mathbf{f}_{\mathrm{gp}i}}{V_{\mathrm{cell}}} \\ =& -\varepsilon_{sm}\boldsymbol{\nabla} P_{\mathrm{g}} + \varepsilon_{sm}\boldsymbol{\nabla}\cdot\overline{\overline{\tau}}_{\mathrm{g}} + \sum_i^{N_{\mathrm{m}}}\varepsilon_{\mathrm{g}}\mathbf{f}_{\mathrm{d}i}/V_{\mathrm{cell}},\end{aligned} \tag{7.32}$$

where N_{m} is the number of particles of m^{th} phase in a fluid cell. The last term in Eq. (7.32) may also be calculated approximately using local mean gas and particle velocities:

$$\sum_{i}^{N_{\mathrm{m}}} \varepsilon_{\mathrm{g}} \mathbf{f}_{\mathrm{d}i} / V_{\mathrm{cell}} = \beta(\mathbf{v}_{\mathrm{g}} - \mathbf{v}_{sm}), \tag{7.33}$$

where β use the same form as in Eq. (7.30), except that the velocities are replaced by the local mean values in a fluid cell, i.e.,

$$\beta = \begin{cases} 150 \frac{\varepsilon_{sm}^2}{\varepsilon_{\mathrm{g}} d_{\mathrm{p}m}^2} \mu_{\mathrm{g}} + 1.75 \varepsilon_{sm} \frac{\rho_{\mathrm{g}}}{d_{\mathrm{p}m}} |\mathbf{v}_{\mathrm{g}} - \mathbf{v}_{sm}| & \text{for } \varepsilon_{\mathrm{g}} \leq 0.8 \\ \frac{3}{4} C_{\mathrm{D}} \frac{\varepsilon_{\mathrm{g}} \varepsilon_{sm}}{d_{\mathrm{p}m}} \rho_{\mathrm{g}} |\mathbf{v}_{\mathrm{g}} - \mathbf{v}_{sm}| \varepsilon_{\mathrm{g}}^{-2.7} & \text{for } \varepsilon_{\mathrm{g}} > 0.8. \end{cases} \tag{7.34}$$

The solid volume fraction and local mean solid velocities are evaluated in a fluid computational cell:

$$\varepsilon_{sm} = \frac{\sum_i^{N_{\mathrm{m}}} V_{\mathrm{p}i}}{V_{\mathrm{cell}}}, \tag{7.35}$$

$$\mathbf{v}_{sm} = \frac{\sum_i^{N_{\mathrm{m}}} \mathbf{v}_{\mathrm{p}i} V_{\mathrm{p}i}}{\sum_i^{N_{\mathrm{m}}} V_{\mathrm{p}i}}. \tag{7.36}$$

The volume of a computational cell, V_{cell}, in two-dimensional (2D) simulations is calculated using the cell thickness in the third dimension as the diameter of a spherical particle.

Based on the previous discussion above, it can be seen that the fluid-particle effective drag force can be calculated in two ways to transfer between gas and particle motion equations. The first method is to calculate the drag force using Eq. (7.33) in a fluid cell and then assign this mean drag force back to each particle in the cell. This method, with the assumption that particles in a cell with the same diameter have the same drag force, is used for most of the simulations in this paper. The second method is to calculate the drag force on each particle using Eq. (7.29) and then sum up the particle drag forces in a fluid cell as the total drag force on the fluid according to Newton's third law. This method is employed for one case as a comparison to the results from the first method. However, it should be noted that further assumptions are made in this paper. One assumption is that the total drag force on the gas is calculated using Eq. (7.33) and is approximately equal in magnitude to that obtained from the summation of each particle's drag force. For the second method, Eq. (7.33) is also used for calculating the drag force on gas phase and the only difference between these method is the way to obtain the drag force on the particles. Finally, viscous stress gradient in Eq. (7.28) is neglected.

7.2.4 Numerical Formulation

A Fortran code, Multiphase Flow with Interphase eXchanges (MFIX), is used for all simulations in this work. MFIX uses a finite volume approach with a staggered grid for the discretization of the TFM governing equations to reduce numerical instabilities (Syamlal, 1998). Scalars such as pressure and volume fraction are stored at the cell centers and the velocity components are stored at cell surfaces. A second-order discretization is used for spatial derivatives and first-order discretization for temporal derivatives. A modified SIMPLE algorithm is employed to solve the discretized equations (Syamlal, 1998). The explicit time integration method is used to solve the translational and rotational motion equations used in the DEM (Cundall and Strack, 1979; Hoomans et al., 1996).

7.3 Simulation Conditions

Gas-solid fluidized beds were simulated using the hybrid TF-DEM model presented in the methodology subsection (for $m = 1$). The fluidized beds simulated have very small depths compared to the other two dimensions. Therefore, two dimensional simulations were performed, which also reduce the computational requirements needed for three dimensional (3D) simulations. The first computational case simulates a fluidized bed experiment with a central air jet flow, presented by Tsuji et al. (Tsuji et al., 1993). This case will be referred to as the central jet case, hereafter. The computational domain is shown in Fig. 7.2 (a) and the simulation parameters are listed in Tab. 7.1. Most particle parameters are set to be the same as what were used in the experiment. One important difference between the computational setup and experimental setup is that there is only one layer of particles in the thin depth direction for computations while there were about five particle layers in the experiment.

A second simulation for a bubbling fluidized bed with uniform inflow was performed to analyze a different flow situation, where the bed is fluidized by a uniform air inflow. The simulations were based on the experiment of the bubbling fluidized bed by Goldschmidt et al. (Goldschmidt et al., 2003). This case will be referred to as the uniform inflow case, hereafter. The 2D simulation was set up using the same experiment conditions except there is only one

Table 7.1 Computational parameters and general initial and boundary conditions for the central jet case and the uniform inflow case.

	Central jet case	Uniform inflow case
Geometry:		
Height of domain (cm)	90	45
Width of domain (cm)	15	15
Horizontal grid size, Δx (cm)	1	1
vertical grid size, Δy (cm)	2	1
Particle properties:		
Particle diameter (cm)	0.4	0.25
Particle density (g/cm^3)	2.7	2.526
Particle stiffness coefficient (dyne/cm)	8×10^5	8×10^5
Particle damping coefficient (dyne $\cdot$ s/cm)	18	1.77
Particle friction coefficient	0.2	0.1
Particle number	2400	4000
Initial conditions:		
ε_{g}	1.0	1.0
$v_{\mathrm{g}}(= U_{\mathrm{mf}})$ (cm/s)	180	128
Initial bed height (cm)	22	15
Boundary conditions:		
Central air jet inflow (cm/s)	3900	$1.5U_{\mathrm{mf}}$
Specified pressure at outlet (Pa)	101325.0	101325.0
Wall boundary for gas phase	No slip	No slip
Wall stiffness coefficient (dyne/cm)	1.2×10^6	1.2×10^6
Wall damping coefficient (dyne $\cdot$ s/cm)	22	3.93

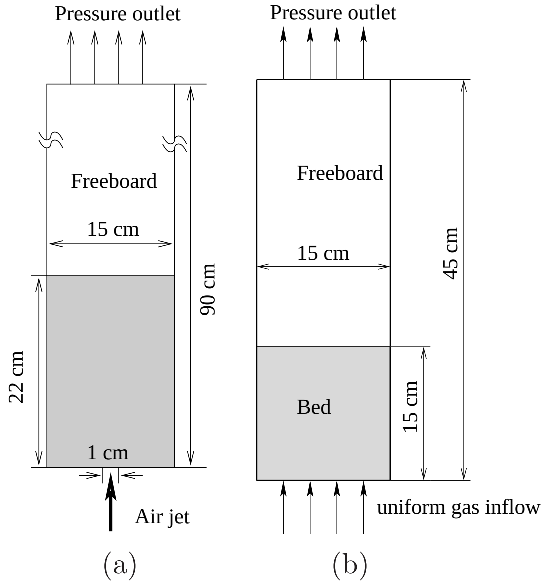

Figure 7.2 Schematic showing computational domains for (a) Tsuji et al. (1993) (b) Goldschmidt et al. (2003) experiments.

layer of particles in the third dimension. The computational domain is shown in Fig. 7.2 (b). and parameters are shown in Tab. 7.1.

The particle responses to the flow fields in these simulations can be analyzed as follows to further elucidate and justify the hybrid method used. Define the particle Stokes number as

$$St = \frac{\tau_p}{\tau_g}, \tag{7.37}$$

where $\tau_p = \frac{\rho_p d^2}{18\mu}$ is particle Stokesian relaxation time, and $\tau_g = \frac{d}{\mathbf{v}_g}$ can be deemed as a characteristic time scale for gas momentum convection over one particle diameter. Taking the uniform inflow case as an example, the Stokes number $St \approx 37000$. The particle volume fractions are typically greater than 0.1 in bed. In such a dense particle flow with very high Stokes number, gas turbulence is damped and small scale gas velocity fluctuations do not affect the particle dynamics significantly. Therefore, directly modeling the sub-grid gas velocities is not considered in this paper.

Simulations using the TFM for both cases were also carried out using the same grids corresponding to those listed in Tab. 7.1. However, the particle motion is modeled by the solid phase equations in the TFM instead of using DEM directly. All the cases were simulated for 20 seconds simulation time. The computational time used by the TFM and the hybrid method

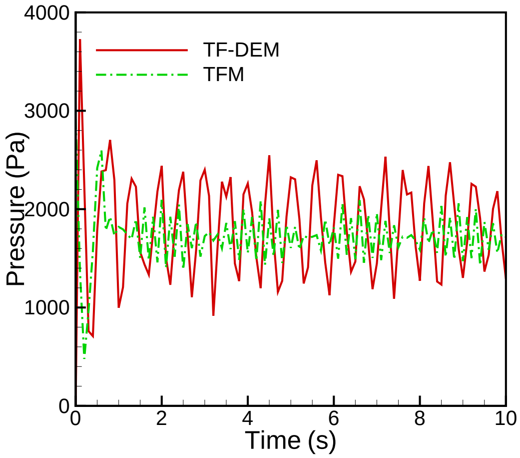

Figure 7.3 Pressure drop at 20 cm above the inlet boundary fluctuates with time for the central jet fluidized bed.

for the central jet case was 5350 and 6780 seconds, respectively, on one Opteron 270 (2.0 GHz) processor. Only results for the first 10 seconds will be presented in the next subsection, since it was found that the fluidized beds reached a quasi-steady state after approximately 5 seconds.

7.4 Results and Discussion

Computational results obtained from the simulation of the central jet case are first presented. The pressure drop at 20 cm above the inlet boundary obtained from the TF-DEM simulation, as shown in Fig. 7.3 is similar to Tsuji et al.'s computational findings, i.e., frequency and magnitude of fluctuation are in good agreement with experiments but with a higher mean pressure (Tsuji et al., 1993). The TFM predicts that the pressure drop fluctuates around a similar mean pressure, but with a smaller fluctuating amplitude. This is probably because averaged equations are solved in TFM. A refined grid with $\Delta x = 1\,\mathrm{cm}$ and $\Delta y = 1\,\mathrm{cm}$ is used to determine the grid dependence of this hybrid method. Statistical error in the particle field estimation becomes larger as the grid is refined due to the grid-cell based averaging technique used in this paper. The comparison between the temporally averaged solid volume fraction distributions calculated from the coarse and the fine grids is shown in Fig. 7.4. It can be seen that the result from the fine grid shows slightly higher bed expansion and a more asymmetric

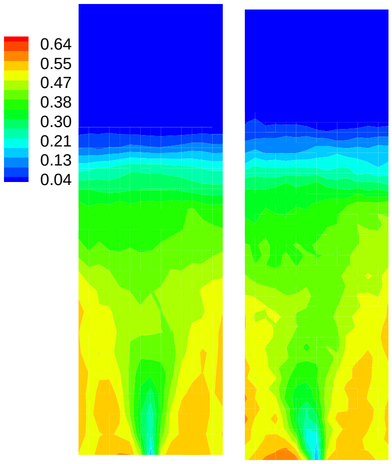

(a) (b)

Figure 7.4 The averaged (5-10 s) particle volume fractions for the central jet fluidized bed for (a) the coarse grid with $\Delta x = 1\,\text{cm}$ AND $\Delta y = 2\,\text{cm}$, and (b) the fine grid with $\Delta x = 1\,\text{cm}$ AND $\Delta y = 1\,\text{cm}$. The domain in the figure only shows 45 cm above the inlet with width of 15 cm.

solid distribution with respect to the central jet. A method to address the particle field estimation problem will be discussed in the conclusion subsection. The difference caused by the grid refinement, however, does not alter the comparison between the hybrid method and TFM made in this paper. The coarse grid was also used in previous computational studies (Tsuji et al., 1993; Xu and Yu, 1997). The coarse grid results are thus shown in the following. The choice of the grid for the uniform inflow case is based on our grid refinement study for the TFM simulations of the same systems (Sun and Battaglia, 2006). The logic is that this grid should capture enough details of the gas field and particle field as shown in the TFM simulations. It has been shown that the grid of cell size $\Delta x = 1$ cm, $\Delta y = 1$ cm produced an average error of 1.4% and a maximum error of 3.7% in time-averaged volume fraction, compared to the Richardson extrapolation results and that further grid refinement had little influence on the results.

The bulk coordination number is defined as the averaged number of contacting neighbors of a particle. The time evolution of bulk coordination number can be used to characterize dynamic responses of granular systems (Sun et al., 2006). The bulk coordination number corresponds to the first peak in the isotropic radial distribution function $g(r)$ and is a measure of order in

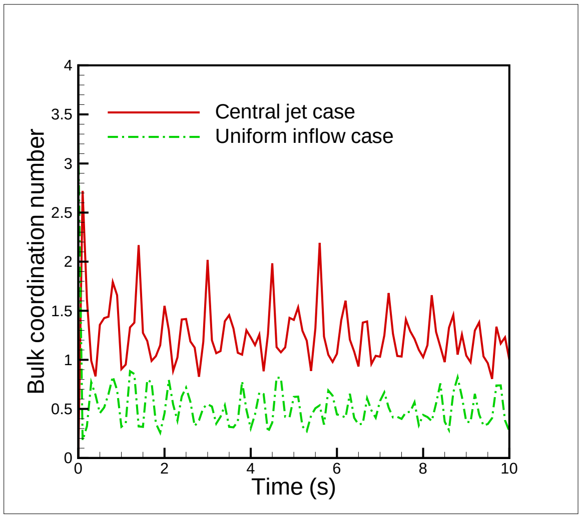

Figure 7.5 The bulk coordination numbers as a function of time

the particle pattern. Thus, it can indirectly give a sense of whether the particle phase is more "gas-like" or "liquid-like". The isotropic radial distribution function $g(r)$ cannot be rigorously defined in the anisotropic configurations used in the simulations and is not presented in the paper. The bulk coordination numbers varying with time for the two simulations are shown in Fig. 7.5. The bulk coordination number for the central jet case varies around 1.2, which indicates pair structures or other multi-contact structures exist in the system. In contrast, the bulk coordination number for the uniform inflow case varies around 0.5, which indicates structures with contacting particles do not prevail. To further elucidate the spatial variation of the particle contacts, we look at local quantities for each particle.

The particle instantaneous positions and velocities are shown in Fig. 7.6 for the TF-DEM simulation of the central jet case. The particle movements and bed expansion behaviors are also in qualitative agreement with the experimental observation. These agreements serve to initially substantiate the practicality of the hybrid TF-DEM model presented in the paper. The number of contacting particles for each particle, N_c, is defined as the number of contacting neighbors of one particle. A direct indication of N_c of each particle is to determine if a particle is in a binary collision, i.e., $N_c = 1$, or is in a multi-contact, i.e., $N_c > 1$. The contour of N_c for each particle is also presented in Fig. 7.6. From the result, it is clear that N_c is not distributed homogeneously in space. The N_c is low (1-2) in bubble regions but high in other parts (> 2),

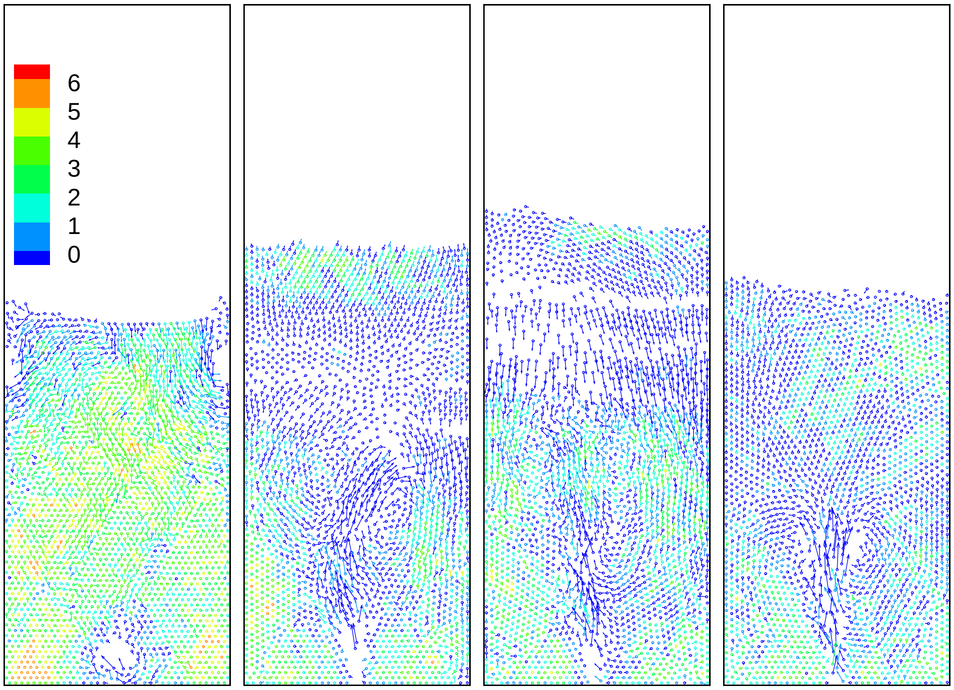

(a) 0.1 s (b) 2 s (c) 5 s (d) 10 s

Figure 7.6 Instantaneous particle positions and velocities for the central jet fluidized bed, denoted by points and vectors. The contour levels show the magnitudes of N_c. The domain in the figure only shows 45 cm above the inlet with width of 15 cm.

which are mainly on the bottom shoulders of the bed beside the jet after the jet penetrates the bed (see Fig. 7.6 (b)-(d)). The high N_c shows that multi-contacts are prevailing in those regions away from bubbles,

The spatial distributions of particle contact forces, drag forces and the ratios of these forces are shown in Fig. 7.7. The magnitudes of total forces in every computational cell are shown, i.e., the total contact force at a cell center, $\mathbf{f}_{\mathrm{c}j} = \sum_i^{N_m} \mathbf{f}_{\mathrm{c}i}$, and the total drag force at a cell center, $\mathbf{f}'_{\mathrm{gp}j} = \sum_i^{N_m} \mathbf{f}'_{\mathrm{gp}i}$, where i and j are indices of particles and grid nodes, respectively. The force is also scaled by the magnitude of the gravitational force of a particle. It can be seen from the instantaneous distributions (Fig. 7.7(a)) that the contact forces are large in the regions away from bubbles, which is consistent with the experimental observation that higher particle pressure is generated under bubbles (Rahman and Campbell, 2002). The drag forces are large in the jet region. The ratios of contact forces to drag forces vary between 2–10 in most of the bed region. However, contact forces may be as high as 100 times that of the drag forces (higher than the contour level shown in Fig. 7.7) in the bottom shoulder regions beside the jet. The high contact force regions could also correspond to the high solid stress regions. The locations of large contact forces and force ratios are correlated with the locations of higher N_c as compared to the corresponding snapshot at 5 s in Fig. 7.6. Solid volume fractions in most of these regions are less than the critical solid volume fraction, ε_s^* (see the left panels in Fig. 7.8). The solid stress would be calculated using the KTGF. Since the solid stress calculated using the KTGF does not take the contribution from the collisions with $N_\mathrm{c} > 1$ into account, the solid stresses in these regions are also expected to deviate from the stresses predicted using the KTGF. These observations emphasize the importance of studying particle contacts in the regions away from bubbles in order to understand the constitutive behavior of a fluidized bed. The time averaged distributions (Fig. 7.7(b)) show similar trends although the forces are distributed more homogeneously.

A comparison between the solid volume fractions predicted by the TF-DEM model and those predicted by TFM is also performed. The instantaneous and time averaged (5-10 s) solid volume fraction distributions for the central jet case are shown in Fig. 7.8 (a) and (b),

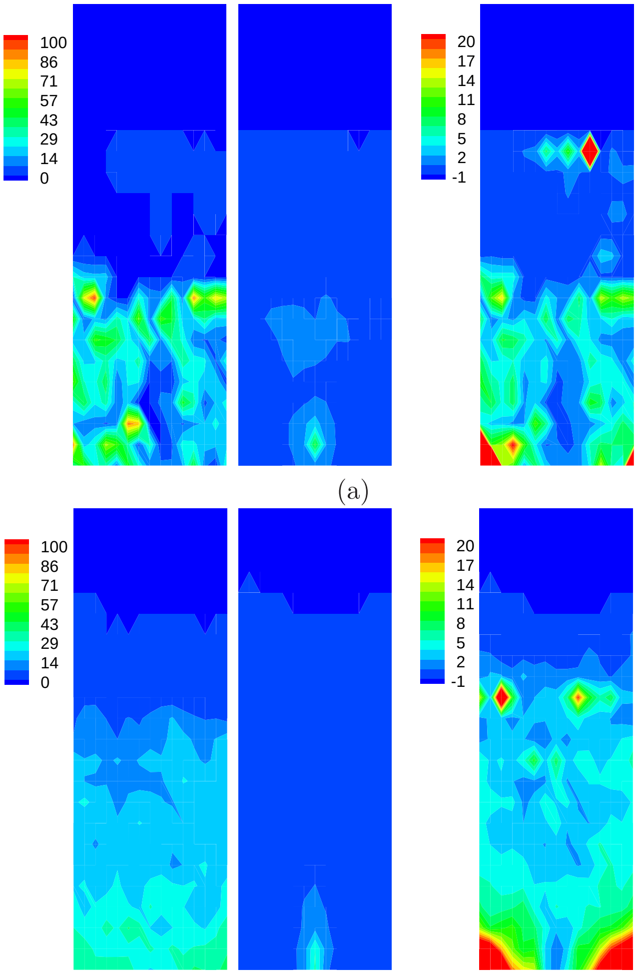

(a)

(b)

Figure 7.7 Distribution of particle contact forces and drag forces and their ratios for the central jet fluidized bed for (a) the instantaneous snapshots at 5 s, and (b) the time averaged snapshots (5-10 s). The left panel shows contact forces, the middle panel shows drag forces and the right panel shows the ratios of contact forces to drag forces. The fist legend levels indicate the magnitudes of forces scaled by gravitational force of a particle. The second legend levels indicate the ratios, where -1 indicates that the drag force is zero at that position. The second legend levels do not show the highest ratio of around 100 in order to distinguish the majority of ratios below 20. The domain in the figure only shows 45 cm above the inlet with width of 15 cm.

respectively. The distributions demonstrate that the TF-DEM model and TFM model predict similar jet penetration behavior. However, the TFM predicts a more homogeneous and symmetric distribution of solids. The TF-DEM model can capture the concentration difference in the shoulder regions even in the time averaged results as seen in Fig. 7.8 (b). The difference reflects the inability of the TFM to capture the structural information although the TFM predicts a similar mean pressure drop as the TF-DEM model does. The inability may also be ascribed to the solid constitutive closures used in the TFM. The closures do not adequately model the stress and energy dissipation caused by multi-contacts, which reduces the preferential change in solid volume fractions. A quantitative account of the differences between the stresses and dissipation calculated using the TF-DEM and using the TFM is the subject of a future study (Sun and Battaglia, 2007).

For the uniform inflow case, bed dynamics were first analyzed by the time evolution of the mean particle height. The mean particle height is defined as the arithmetic mean of the heights of all particles in the bed. It is straight forward to calculate in the TF-DEM model and can also be estimated by a method defined in (Sun and Battaglia, 2006) for the TFM. The mean particle height as a function of time is shown in Fig. 7.9. It is found that mean particle heights predicted by both models fluctuate at a similar level. The 5–10 s time averaged values are 8.9 cm and 9.16 cm for TF-DEM model and TFM, respectively. Both are lower than the experimental value of 11.4 cm (Goldschmidt, 2001).

The particles instantaneous positions, velocities and N_{c} are presented in Fig. 7.10. It can be seen that the bed is uniformly fluidized at the start-up stage (Fig. 7.10 (a)) with no bubble and zero N_{c} over almost the whole bed. After bubbles develop, higher N_{c} appear in the region away from the bubble, However, the ratio of number of multi-contacts over the total number of collisions is small, fluctuating around 0.3 as shown in Fig. 7.11. This small ratio indicates that the binary collision assumption in the KTGF may still be reasonable under this flow condition. In contrast, the ratio for the central jet case is higher than 0.6 most of the time, which indicates the binary collision assumption may deviate from the real particle collision scenario to a large degree. The spatial distributions of particle contact forces, drag forces and the ratios of these

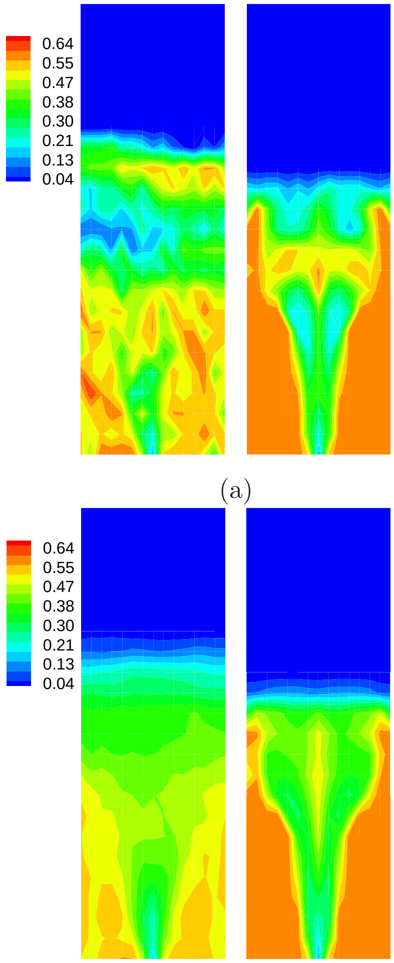

Figure 7.8 Particle volume fractions for the central jet fluidized bed for (a) instantaneous snapshot at 5 s, and (b) time averaged snapshot (5-10 s). The left panel shows the TF-DEM simulation and the right panel shows the TFM simulation. The domain in the figure only shows 45 cm above the inlet with width of 15 cm.

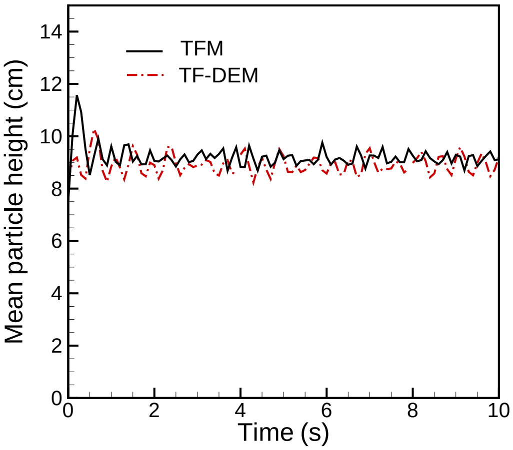

Figure 7.9 The mean particle height as a function of time for the uniform inflow fluidized bed calculated from TF-DEM model and TFM

forces for the uniform inflow case are also shown in Fig. 7.12. Similar observations can be drawn as for the central jet case. However, there is no region where the contact forces are more than 15 times higher than the drag forces as observed in the shoulder region for the central jet case.

The two different formulae for computing the effective drag force based on averaged or instantaneous particle velocities were applied to simulate the uniform inflow case. Since the method using the averaged particle velocities produces the same forces on each particle in a fluid cell, it tends to smear the difference between particle movement and results in less vigorous bed dynamics. It is expected that the method using instantaneous particle velocity will predict higher bed expansion. This effect is actually shown by the time averaged solid volume fraction in Fig. 7.13, where the result produced by the second method shows slightly higher bed expansion. The time average mean particle height predicted by the second method is 9.1 cm, and also higher than that predicted by the first method. However, it should be noted that the difference between the mean quantities predicted by the two formulae is not large. Local quantities such as granular temperature will be further studied to investigate the effect of the formulae.

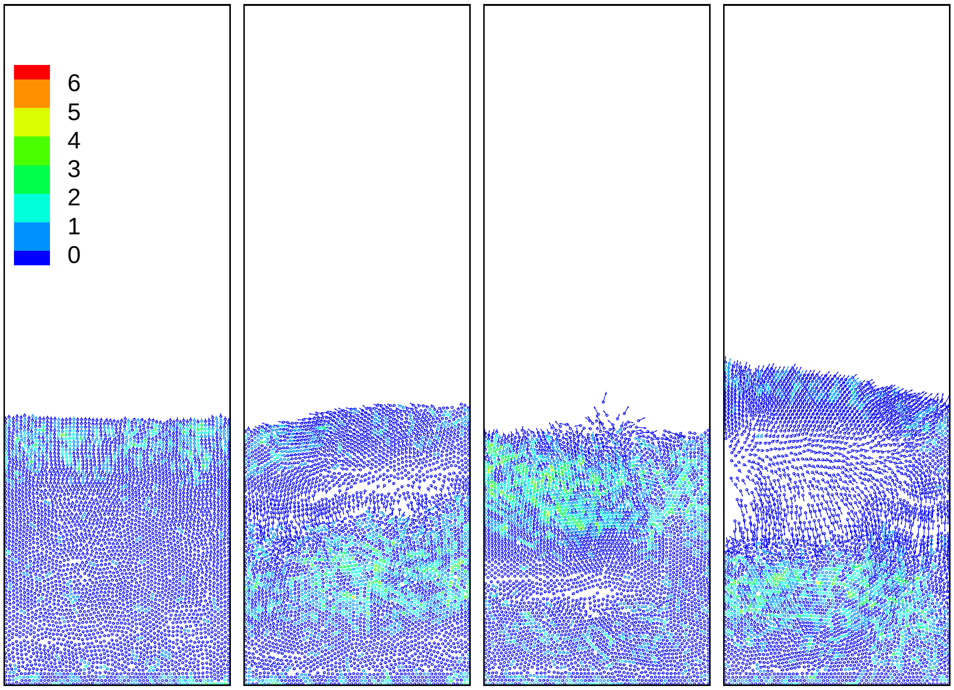

(a) 0.1 s (b) 2 s (c) 5 s (d) 10 s

Figure 7.10 Instantaneous particle positions and velocities for the uniform inflow fluidized bed denoted by points and vectors. The contour level shows the magnitude of N_c.The domain is 15 cm in width and 45 cm in height (refer to Fig. 7.2).

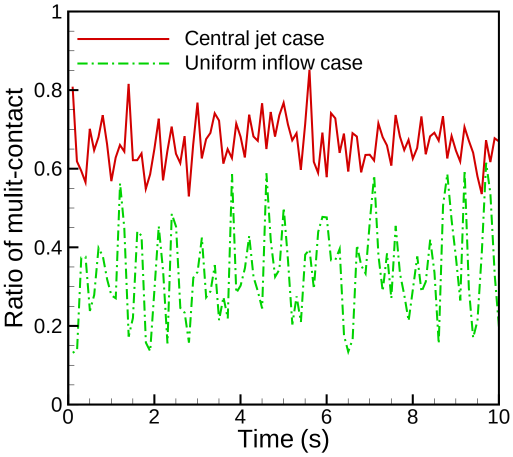

Figure 7.11 The ratio of particles in multi-contacts to the total number of particles in contact as a function of time

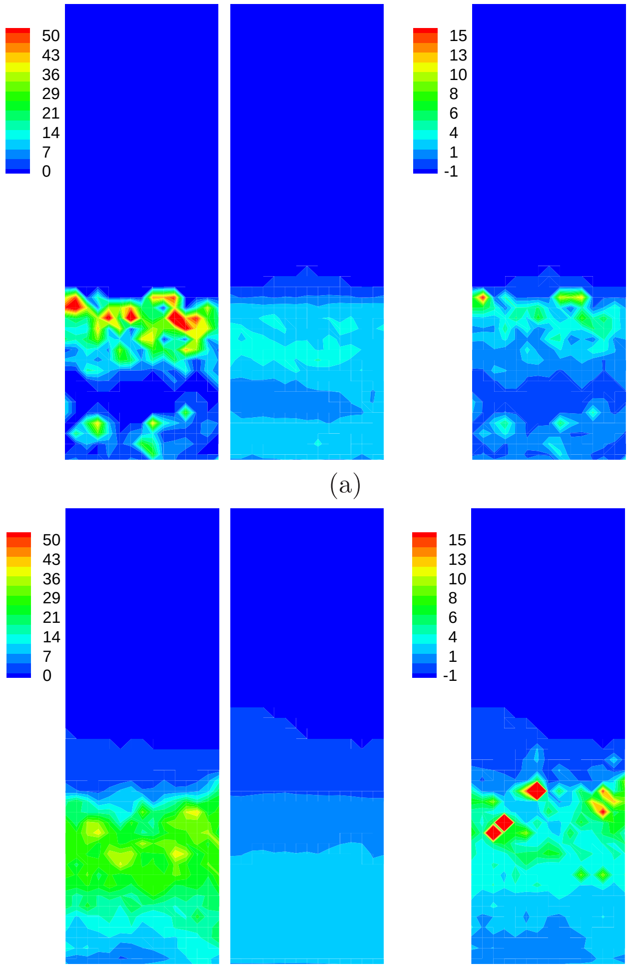

(a)

(b)

Figure 7.12 Distribution of particle contact forces and drag forces and their ratios for the uniform inflow fluidized bed for (a) the instantaneous snapshots at 5 s, and (b) the time averaged snapshots (5-10 s). The left panel shows contact forces, the middle panel shows drag forces and the right panel shows the ratios of contact forces to drag forces. The fist legend levels indicate the magnitudes of forces scaled by gravitational force of a particle. The second legend levels indicate the ratios, where -1 indicates that the drag force is zero at that position. The domain is 15 cm in width and 45 cm in height (refer to Fig. 7.2).

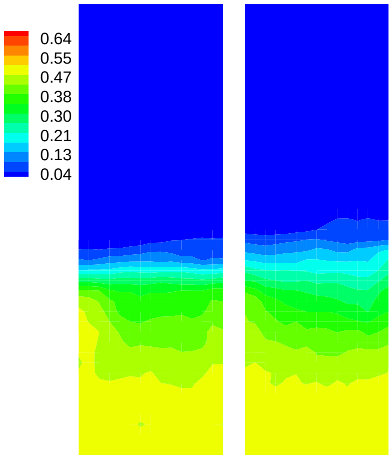

(a) (b)

Figure 7.13 Time average from 5-10 s of the particle volume fractions, for the uniform inflow fluidized bed predicted by the method using (a) averaged particle velocities and (b) instantaneous particle velocities. The domain is 15 cm in width and 45 cm in height (refer to Fig. 7.2).

7.5 Conclusions

A methodology of a hybrid TF-DEM model for gas-solid fluidized beds has been presented. The model couples the discrete element method for particle dynamics with the two-fluid equations for the gas phase. The coupling between the two phases is modeled by the gas-particle interaction force. Simulations of two types of gas-solid fluidized beds have been carried out using the hybrid simulation method. The results of the hybrid TF-DEM simulations are compared to experimental data and TFM simulations. It is found that the TF-DEM simulation is capable of predicting general fluidized bed dynamics, i.e., pressure drop across the bed and bed expansion, which are in agreement with experimental measurements and TFM predictions. Number of contacting particles, N_{c}, are found to be greater than 1 in the regions away from bubble. The contact forces are much larger than the effective drag forces in the same regions. It is also demonstrated that the multi-contacts prevail in the central-jet fluidized bed, implying that the binary instantaneous collision assumption in the KTGF may not be applicable in this flow condition. For the uniform inflow fluidized bed, the number of contacting particles are around one to two so that the binary collision assumption is reasonable in this flow condition.

With further research, the particle contact information will hopefully provide guidelines for constitutive model development and may contribute to the sub-grid modeling method proposed by Sundaresan (Sundaresan, 2000). The relations between the flow conditions and fluidized bed constitutive behaviors and how the multi-interactions should be incorporated into the constitutive modeling clearly need further investigation. It would be instructive to first compare the stresses computed using particle information from the TF-DEM simulations with the stresses computed using the KTGF or using the friction-kinetic model (Srivastava and Sundaresan, 2003). The stress analysis will be given in a following paper (Sun and Battaglia, 2007).

The effect of computing an effective drag force on a particle in terms of averaged or instantaneous particle velocities were demonstrated. It was shown that the formulation using instantaneous particle velocities better captures the force difference at particle scale and predicts a higher bed expansion, which is closer to the corresponding experimental results. Furthermore, the statistical error in estimation of the interphase momentum transfer term becomes high as the grid is refined. This motivates using more sophisticated kernel estimation methods to achieve optimal error control in both statistical error and discretization error (Dreeben and Pope, 1992; Garg and Subramaniam, 2006).

CHAPTER 8. CONCLUSIONS AND FUTURE WORK

8.1 Conclusions

In this dissertation, research efforts have been devoted to simulating and understanding segregation phenomena in gas-solid flows and dry granular flows.

In chapter 4, CFD simulations using the multi-fluid model have been conducted to study grain fluidization and grain-chaff segregation. It has been demonstrated that the pressure drop curve across the grain bed can be predicted by the CFD simulations. Modeling grain and chaff as spherical particles with the same diameter but different densities, the segregation of grain from chaff in a combine has also been captured by CFD simulations. However, it was found that it was difficult to simulate fluidization of a pre-mixed grain and chaff mixture. This motivated the studies of particle scale physics in order to understand the segregation mechanism and to derive models that can accurately predict the segregation phenomena.

In chapter 5, the multi-fluid model has been improved by incorporating particle rotation using a simplified kinetic theory for rapid granular flow of slightly frictional spheres. Simulations without and with particle rotation were performed to study bubble dynamics in a monodispersed gas-solid fluidized bed and segregation phenomena in a dense gas-solid fluidized bed of a binary solid mixture. Results were compared between simulations with and without the particle rotation model and with corresponding experimental results. In the monodispersed system, bubble intensity and bed expansion increased as a result of more energy dissipation with the particle rotation model, which better agrees with experimental results. In the binary systems studied in this paper, better agreement was achieved by using the model with particle rotation in the regime where kinetic theory is applicable and the particle-particle interactions have a noticeable effect on segregation. These preliminary results indicate that particle rotation is an important microscopic physics to be incorporated into the fundamental hydrodynamic model. However, the particle rotation model does not have the same kind of improvement for segregation cases where the gas inlet velocity is between the minimum fluidization velocities of the small and large particles. The reason is thought to be due to the fact that the large particles are not very well fluidized in this condition and the long-lasting microstructures formed by the large particles hinder the segregation.

Segregation and the microstructures for a Brazil nut problem in a dense dry granular system have been studied in chapter 6. MD simulations have been performed for the BNP at low vibration frequency in order to understand the underlying physical mechanisms of segregation dynamics. It is concluded that wall friction is the most important physical parameter in determining the segregation behavior in this BNP. The presence of large-scale force networks bearing larger-than-average forces has been shown in the compression stage with wall friction, while there are much fewer contacts in the expansion stage. The PDF of normal contact forces in the force network bears exponential tails similar to those found in packing experiments. The two-point force correlation of the force network decays quickly. A modified minimum spanning tree algorithm has been developed. It was shown to be able to capture all the contacts within the force network and thus was able to recover the force distribution and force correlation for the force network.

In chapter 7, hydrodynamics and microstructures in gas-solid fluidized beds have been investigated. A methodology of a hybrid TF-DEM model was used. Simulations of two types of gas-solid fluidized beds have been carried out using the hybrid simulation method. Multi-particle contacts and large contact force was found in the regions away from bubble. Therefore, the assumption of binary collisions for KTGF is expected to be violated in these regions.

In summary, the multi-fluid model presented in chapter 3 was found to be able to capture some basic features of fluidization and segregation in granular systems. The investigations on microscale physics showed that the particle properties and microstructures affect the dynamic behavior and the segregation rate of granular flows. The microscale physics should be incorporated to continuum models for better predictions of granular flows. This may be feasible even in the dense flow regime as indicated by the short force correlation length.

The research approaches, including the multi-fluid model, discrete element method and the hybrid method, compose a hierarchical multiscale modeling framework with information flowing from the microcale to the macroscale. The methodologies in this framework have been demonstrated to be complimentary to each other. The microscale and hybrid methods are able to capture useful microscale information to provide physical insights and relative modeling information to the continuum models.

The full potential of this framework, however, has not been exploited yet. Some promising continuing research, which could lead to better understanding and modeling of granular flows, will be discussed in the future work section.

8.2 Future work

8.2.1 Probe microscale physics of granular flows

Systematic simulations of granular flows using microscale and hybrid methods can be performed for all flow regimes ranging from the rapid flow regime to the quasi-static regime in order to better understand the flow characteristics. The following information is of particular interest for continuum model development.

8.2.1.1 Particle velocity distributions and correlations

The single particle velocity distribution is usually assumed to be Maxwellian in KTGF. It will be interesting to see how the single particle velocity distribution extracted from the simulations deviate from the Maxwellian form as the particle elasticity, roughness, size distribution and flow regimes change. The spatial correlation of particle velocities should also be calculated to investigate the correlation length variation with respect to all flow parameters.

8.2.1.2 Force distributions and correlations

Force heterogeneities can be investigated by extracting contact force probability distribution from the simulations. The force spatial correlations can be calculated to get the force correlation length.

8.2.1.3 Solid stresses

Macroscale stress field can be obtained using a coarse-graining function with width w. The relation between the stresses and the width w can be explored to examine if there is a scale independence in solid stress filed. The consistency of the computed stresses with those predicted by other constitutive equations can also be examined. Fluctuations of the stresses and strain rate can be calculated.

The information obtained from probing the microsale physics can provide insights for constructing constitutive relations and the correlation length scales may directly be used by such relations.

8.2.2 Develop continuum models

8.2.2.1 Continuum models for rapid flow regime

A multi-fluid model can be derived from Boltzmann-like kinetic equations. While the formal procedure is not novel, a new method, direct quadrature method of moments (DQMOM) (Fox, 2003), can be exploited to close the model. Using the DQMOM for the multi-fluid model has the advantages that far-from-equilibrium flow conditions and particle size distributions can be considered.

8.2.2.2 Constitutive models for dense flow regime

The hypoplastic constitutive model (Wu et al., 1996) may be employed and improved by incorporating the dependence on particle properties and strain rate fluctuations, which can be obtained from the microscale simulations.

As a last but not least note, validating the models against experimental data is a crucial step underlying all the developments. Microscale models can serve as fruitful and powerful tools to provide microscale information only after they have been validated against accurate measurement data. Therefore, accurate numerical methods and accurate experimental techniques are necessary for the model developments.

BIBLIOGRAPHY

Agrawal, K., Loezos, P. N., Syamlal, M., and Sundaresan, S. (2001). The role of meso-scale structures in rapid gas-solid flows. *Journal of Fluid Mechanics*, 445:151–185.

Aho, A. V., Hopcroft, J. E., and Ullman, J. D. (1983). *Data Structures and Algorithms*. Addison-Wesley, Reading, MA.

Alam, M., Willits, J. T., Arnarson, B. O., and Luding, S. (2002). Kinetic theory of a binary mixture of nearly elastic disks with size and mass-disparity. *Physics of Fluids*, 14(11):4085–4087.

Allen, M. P. and Tildesley, D. J. (1987). *Computer Simulation of Liquids*. Clarendon Press, Oxford.

Anderson, T. B. and Jackson, R. (1967). A fluid mechanical description of fluidised beds. *Industrial and Engineering Chemistry Fundamental*, 6:527–539.

Aranson, I. S. and Tsimring, L. S. (2001). Continuum description of avalanches in granular media. *Physical Review E*, 64:020301.

Aranson, I. S. and Tsimring, L. S. (2002). Continuum theory of partially fluidized granular flows. *Physical Review E*, 65:061303.

Arnarson, B. and Willits, J. (1998). Thermal diffusion in binary mixture of smooth, nearly elastic spheres with and without gravity. *Physics of Fluids*, 10:1324–1328.

Arnarson, B. O. and Jenkins, J. T. (2002). Kinetic theory for identical, frictional, nearly elastic spheres. *Physics of Fluids*, 14(3):1228–1235.

Bazant, M. Z. (2003). A theory of cooperative diffusion in dense granular flows. *Condensed Matter*, page 0307379. e-prints.

Bazant, M. Z. (2006). The spot model for random-packing dynamics. *Mechanics of Materials*, 38(8-10):717–731.

Beetstra, R., van der Hoef, M. A., and Kuipers, J. A. M. (2007). Numerical study of segregation using a new drag force correlation for polydisperse systems derived from lattice-Boltzmann simulations. *Chemical Engineering Science*, 62(1-2):246–255.

Beris, A. N. and Edwards, B. J. (1994). *Thermodynamics of Flowing Systems: with Internal Microstructure*, volume 36 of *Oxford engineering science series*. Oxford University Press, Oxford, United Kingdom.

Bird, R. B., Stewart, W. E., and Lightfoot, E. N. (1960). *Transport Phenomena*. John Wiley & Sons, Inc., New York, NY, first edition.

Biswas, P., Sanchez, P., Swift, M. R., and King, P. J. (2003). Numerical simulations of air-driven granular separation. *Physical Review E*, 68:050301(R).

Bokkers, G. A., van Sint Annaland, M., and Kuipers, J. A. M. (2004). Mixing and segregation in a bidisperse gas-solid fluidised bed: a numerical and experimental study. *Powder Technology*, 140:176–186.

Boyalakuntla, D. (2003). *Simulation of Granular and Gas-Solid Flows Using Discrete Element Method*. PhD dissertation, Carnegie Mellon University, Pittsburgh, Pennsylvania.

Breu, A. P. J., Ensner, H. M., Kruelle, C. A., and Rehberg, I. (2003). Reversing the Brazil nut effect: competition between percolation and condensation. *Physical Review Letters*, 90(1):014302.

Brey, J., Dufty, J. W., and Kim, C. S. a. A. (1998). Hydrodynamics for granular flow at low density. *Physical Review E*, 58(4):4638–4653.

Burtally, N., King, P. J., and Swift, M. R. (2002). Spontaneous air-driven separation in vertically vibrated fine granular mixtures. *Science*, 295(5561):1877–1879.

Campbell, C. S. (1990). Rapid granular flows. *Annual Review of Fluid Mechanics*, 22:57–92.

Campbell, C. S. (2002). Granular shear flows at the elastic limit. *Journal of Fluid Mechanics*, 465:261–291.

Carnahan, N. F. and Starling, K. E. (1969). Equation of state for nonattracting rigid spheres. *Journal of Chemical Physics*, 51(2):635–636.

Chapman, S. and Cowling, T. G. (1970). *The Mathematical Theory of Non-uniform Gases*. Cambridge University Press, third edition.

Chevron (2005). Refinery overview.
http://www.chevron.com/products/about/pascagoula/refineryprofile/.

Choi, J., Kudrolli, A., Rosales, R. R., and Bazant, M. Z. (2004). Diffusion and mixing in gravity-driven dense granular flows. *Physical Review Letters*, 92(17):174301–4.

CIGR (1999). *CIGR Handbook of Agriculture Engineering*. American Society of Agricultural Engineers. Volume 3.

Cundall, P. A. and Strack, D. L. (1979). A discrete numerical model for granular assemblies. *Gèotechnique*, 29:47–65.

Curtis, J. S. and van Wachem, B. (2004). Modeling particle-laden flows: A research outlook. *AIChE Journal*, 50(11):2638–2645.

Dalla Valla, J. M. (1948). *Micromeritics*. Pitman, Inc.

Ding, J. and Gidaspow, D. (1990). A bubbling fluidization model using kinetic theory of granular flow. *AIChE Journal*, 36(4):523–538.

Dreeben, T. D. and Pope, S. B. (1992). Nonparametric estimation of mean fields with application to particle methods for turbulent flows. Technical report FDA 92-13, Sibley School of Mechanical and Aerospace Engineering, Cornell University.

Duran, J., Mazozi, T., Clément, E., and Rajchenbach, J. (1995). Direct observation of size segregation: convection and arching effect. In Family, F., editor, *Fractal Aspects of Materials*, volume 367, pages 491 – 494, Boston, MA, USA.

Duran, J., Rajchenbach, J., and Clément, E. (1993). Arching effect model for particle size segregation. *Physical Review Letters*, 70(16):2431–2434.

Emeriault, F. and Cambou, B. (1996). Micromechanical modelling of anisotropic non-linear elasticity of granular medium. *International Journal of Solids and Structures*, 33(18):2591–2607.

Enstad, G. (2001). Segregation of powders - mechanisms, processes and counteraction. In Levy, A. and Kalman, H., editors, *Handbook of conveying and handling of particulate solids*, pages 589–602. Elsevier.

Enwald, H., Peirano, E., and Almstedt, A. E. (1996). Eulerian two-phase flow theory applied to fluidization. *International Journal of Multiphase Flow*, 22 Suppl.:21–66.

Ergun, S. (1952). Fluid flow through packed columns. *Chemical Engineering Progress*, 48:89–94.

Evans, D. J. and Morriss, G. P. (1990). *Statistical Mechanics of Nonequilibrium Liquids.* Theoretical chemistry. Academic Press.

Feitosa, K. and Menon, N. (2002). Breakdown of energy equipartition in a 2D binary vibrated granular gas. *Physical Review Letters*, 88(19):198301–1.

Feng, Y. Q. and Yu, A. B. (2007). Microdynamic modelling and analysis of the mixing and segregation of binary mixtures of particles in gas fluidization. *Chemical Engineering Science*, 62(1-2):256–268.

Fox, R. O. (2003). *Computational Models for Turbulent Reacting Flows.* Cambridge University Press, Cambridge, United Kingdom, first edition.

Gao, D., Subramaniam, S., Fox, R. O., and Hoffman, D. K. (2005). Objective decomposition of the stress tensor in granular flows. *Physical Review E*, 71:021302.

Garg, R. and Subramaniam, S. (2006). Accurate numerical estimation of interphase momentum transfer in Lagrangian-Eulerian simulations of dispersed two-phase flows. *International Journal of Multiphase Flow*. Under review.

Garzó, V. and Dufty, J. (1999a). Homogeneous cooling state for a granular mixture. *Physical Review E*, 60(5):5706–5713.

Garzó, V. and Dufty, J. (2002). Hydrodynamics for a granular mixture at low density. *Physics of Fluids*, 14:1476–1490.

Garzó, V. and Dufty, J. W. (1999b). Dense fluid transport for inelastic hard spheres. *Physical Review E*, 59(5):5895–5911.

Garzó, V. and Montanero, J. M. (2003). Shear viscosity for a moderately dense granular binary mixture. *Physical Review E*, 68:041302.

Garzó, V., Montanero, J. M., and Dufty, J. W. (2006). Mass and heat fluxes for a binary granular mixture at low density. *Physics of Fluids*, 18(8):083305–14.

Gera, D., Syamlal, M., and O'Brien, T. (2004). Hydrodynamics of particle segregation in fluidized beds. *International Journal of Multiphase Flow*, 30:419–428.

Gidaspow, D. (1994). *Multiphase Flow and Fluidization: Continuum and Kinetic Theory Descriptions*. Academic Press, Boston, USA.

Gidaspow, D., Jung, J., and K., S. R. (2004). Hydrodynamics of fluidization using kinetic theory: an emerging paradigm 2002 Flour-Daniel lecture. *Powder Technology*, 148:123–141.

Goldschmidt, M. (2001). *Hydrodynamic Modelling of Fluidised Bed Spray Granulation*. Ph.D. Thesis, Twente University, Netherlands.

Goldschmidt, M., Beetstra, R., and Kuipers, J. (2002). Hydrodynamic modelling of dense gas-fluidised beds: Comparison of the kinetic theory of granular flow with 3d hard-sphere discrete particle simulations. *Chemical Engineering Science*, 57:2059–2075.

Goldschmidt, M., Kuipers, J., and Van Swaaij, W. (2001a). Hydrodynamic modelling of dense gas-fluidised beds using the kinetic theory of granular flow: Effect of coefficient of restitution on bed dynamics. *Chemical Engineering Science*, 56:571–578.

Goldschmidt, M., Kuipers, J., and van Swaaij, W. (2001b). Segregation in dense gas-fluidized beds: Validation of a multi-fluid continuum model with non-intrusive digital image analysis measurements. In *Fluidization X*, Engineering Foundation Conference on Fluidization, pages 795–802, Beijing, People Republic of China.

Goldschmidt, M. J., Link, J. M., Mellema, S., and Kuipers, J. A. (2003). Digital image analysis measurements of bed expansion and segregation dynamics in dense gas-fluidised beds. *Powder Technology*, 138:135–159.

Grad, H. (1949). On the kinetic theory of rarefied gases. *Communications on Pure and Applied Mathematics*, 2:331.

Hinch, E. J. (1995). Introduction to mobile particulate systems. In Guazzelli, E. and Oger, L., editors, *Mobile Particulate Systems*. Kluwer Academic Publishers.

Hoffmann, A. C., Janssen, L. P. M., and Prins, J. (1993). Particle segregation in fluidised binary mixtures. *Chemical Engineering Science*, 48(9):1583–1592.

Hong, D. C., V., Q. P., and Luding, S. (2001). Reverse Brazil nut problem: Competition between percolation and condensation. *Physical Review Letters*, 86(15):3423–3426.

Hoomans, B. P., Kuipers, J. A., Briels, W. J., and van Swaaij, W. P. (1996). Discrete particle simulation of bubble and slug formation in a two-dimensional gas-fluidised bed: A hard-sphere approach. *Chemical Engineering Science*, 51(1):99–118.

Hoomans, B. P., Kuipers, J. A., and van Swaaij, W. P. (2000). Granular dynamics simulation of segregation phenomena in bubbling gas-fluidised beds. *Powder Technology*, 109:41–48.

Hsiau, S. S. and Hunt, M. L. (1996). Granular thermal diffusion in flows of binary-sized mixtures. *Acta Mechanica*, 114:121.

Huerta, D. A. and Ruiz-Suárez, J. C. (2004a). Erratum: Vibration-induced granular segregation: A phenomenon driven by three mechanisms [phys. rev. lett. [92], 114301 (2004)]. *Physical Review Letters*, 93(6):069901(E).

Huerta, D. A. and Ruiz-Suárez, J. C. (2004b). Vibration-induced granular segregation: a phenomenon driven by three mechanisms. *Physical Review Letters*, 92(11):114301.

Iddir, H. and Arastoopour, H. (2005). Modeling of multitype particle flow using the kinetic theory approach. *AIChE Journal*, 51(6):1620–1632.

Jackson, R. (2000). *The Dynamics of Fluidized Particles*. Cambridge University Press, Cambridge, United Kingdom, 1 edition.

Jaeger, H. M., Nagel, S. R., and Behringer, R. P. (1996). Granular solids, liquids, and gases. *Reviews of Modern Physics*, 68(4).

Jenike, A. W. (1987). A theory of flow of particulate solids in converging and diverging channels based on a conical yield function. *Powder Technology*, 50:229.

Jenkins, J. and Mancini, F. (1987). Balance laws and constitutive relations for plane flows of a dense, binary mixture of smooth, nearly elastic, circular disks. *Journal of Applied Mechanics*, 54:27–34.

Jenkins, J. and Mancini, F. (1989). Kinetic theory for binary mixtures of smooth, nearly elastic spheres. *Physics of Fluids*, A1(12):2050–2057.

Jenkins, J. and Savage, S. (1983). A theory for the rapid flow of identical, smooth, nearly elastic, spherical particles. *Journal of Fluid Mechanics*, 130:187–202.

Jenkins, J. T. and Richman, M. W. (1985). Kinetic theory for plane flows of a dense gas of identical, rough, inelastic, circular disks. *Physics of Fluids*, 28(12):3485–3494.

Jenkins, J. T. and Yoon, D. K. (2002). Segregation in binary mixtures under gravity. *Physical Review Letters*, 88(19).

Jenkins, J. T. and Zhang, C. (2002). Kinetic theory for identical, frictional, nearly elastic spheres. *Physics of Fluids*, 14(3):1228–1235.

Johnson, P. and Jackson, R. (1987). Frictional-collisional constitutive relations for granular materials, with application to plane shearing. *Journal of Fluid Mechanics*, 176:67–93.

Kafui, K. D., Thornton, C., and Adams, M. J. (2002). Discrete particle-continuum fluid modelling of gas-solid fluidised beds. *Chemical Engineering Science*, 57:2395–2410.

Khakhar, D. V., McCarthy, J. J., and Ottino, J. M. (1999). Mixing and segregation of granular materials in chute flows. *Chaos*, 9(3):594–610.

Kirkwood, J. G., Buff, F. P., and Green, M. S. (1949). The statistical mechanical theory of transport processes. *Journal of Chemical Physics*, 17(10):988.

Knight, J. B., Jaeger, H. M., and Nagel, S. R. (1993). Vibration-induced sized separation in granular media: The convection connection. *Physical Review Letters*, 70(24):3728.

Kruyt, N. P. and Rothenburg, L. (1996). Micromechanical definition of strain tensor for granular materials. *Journal of Applied Mechanics*, 118:706.

Landry, J. W., Grest, G. S., Silbert, L. E., and Plimpton, S. J. (2003). Confined granular packings: Structure, stress, and forces. *Physical Review E*, 67(4):041303.

Lätzel, M., Luding, s., and Herrmann, H. J. (2000). Macroscopic material properties from quasi-static, microscopic simulations of a two-dimensional shear-cell. *Granular Matter*, 2(3).

Leonard, B. P. (1991). The ultimate conservative difference scheme applied to unsteady one-dimensional advection. *Computer Methods in Applied Mechanics and Engineering*, 88:17.

Lu, H., Gidaspow, D., and Manger, E. (2001). Kinetic theory of fluidized binary granular mixture. *Physical Review E*, 64:061301.

Lubachevsky, B. (1991). How to simulate billiards and similar systems. *Journal of Computational Physics*, 94(2):255.

Luding, S. (2004). Molecular dynamics simulations of granular materials. In Hinrichsen, H. and Wolf, D. E., editors, *The Physics of Granular Media*, page 299. WILEY-VCH Verlag GmbH & Co.KGaA, New York.

Luding, S., Clément, E., Blumen, A., Rajchenbach, J., and Duran, J. (1994). Anomalous energy dissipation in molecular-dynamics simulations of grains: the 'detachment' effect. *Physical Review E*, 50(5):4113.

Luding, S. and Herrmann, H. J. (1999). Cluster growth in freely cooling granular media. *Chaos*, 9(3):673–681.

Luding, S., Lätzel, M., Volk, W., Diebels, S., and Herrmann, H. J. (2001). From discrete element simulations to a continuum model. *Computer Methods in Applied Mechanics and Engineering*, 191:21–28.

Luding, S. and McNamara, S. (1998). How to handle the inelastic collapse of a dissipative hard-sphere gas with the TC model. *Granular Matter*, 1(3):113–128. cond-mat/9810009.

Luding, S. and Pöschel, T., editors (2001). *Granular gases*, volume 564 of *Lecture Notes in Physics*. Springer, Berlin.

Lun, C. and Savage, S. B. (1987). A simple kinetic theory for granular flow of rough, inelastic, spherical particles. *Journal of Applied Mechanics*, 54:47–53.

Lun, C. K. (1991). Kinetic theory for granular flow of dense, slightly inelastic, slightly rough, spheres. *Journal of Fluid Mechanics*, 233:539–559.

Lun, C. K., Savage, S. B., Jeffrey, D. J., and Chepurniy, N. (1984). Kinetic theories for granular flow: Inelastic particles in Couette flow and slightly inelastic particles in a general flow field. *Journal of Fluid Mechanics*, 140:223–256.

Ma, D. and Ahmadi, G. (1988). A kinetic model for rapid granular flows of nearly elastic particles including interstitial fluid effects. *Powder Technology*, 56:191–207.

Massoudi, M. (2004). Constitutive modeling of flowing granular materials: A continuum approach. In Antony, J., Hoyle, W., and Ding, Y., editors, *Granular Materials: Fundamentals and Applications*, page 63. Royal Society of Chemistry.

Möbius, M. E., Cheng, X., Karczmar, G. S., Nagel, S. R., and Jaeger, H. M. (2004). Intruder in the dust: air-driven granular size separation. *Physical Review Letters*, 93(9):198001–1–198001–4.

Möbius, M. E., Lauderdale, B. E., Nagel, S. R., and Jaeger, H. M. (2001). Size separation of granular particles. *Nature*, 414:270.

Montanero, J. M. and Garzó, V. (2003). Shear viscosity for a heated granular binary mixture at low density. *Physical Review E*, 67(2):021308.

Mueth, D. M., Jaeger, H. M., and Nagel, S. R. (1998). Force distribution in a granular medium. *Physical Review E*, 57(3):3164–3169.

Nahmad-Molinari, Y., Canul-Chay, G., and Ruiz-Suárez, J. C. (2003). Inertia in the Brazil nut problem. *Physical Review E*, 68(4):041301–1–6.

Nienow, A. W. and Naimer, N. S. (1980). Continuous mixing of two particulate species of different density in a gas fluidised bed. *Transactions of the Institute of Chemical Engineers*, 58:181–186.

Öttinger, H. C. (2005). *Beyond Equilibrium Thermodynamics*. John Wiley & Sons, Inc, Hoboken, New Jersey.

Ottino, J. and Khakhar, D. (2000). Mixing and segregation of granular materials. *Annual Review of Fluid Mechanics*, 32:55–91.

Patankar, S. V. (1980). *Numerical Heat Transfer and Fluid Flow.* Hemisphere, Inc., Washington.

Plasynski, S., Peters, W., and Passman, S., editors (1992). *Proceedings of the NSF-DOE joint workshop on flow of particulates and fluids*, Gaithersburg. The Department of Energy Solids Transport, Multiphase Flow Program.

Preparata, F. P. and Shamos, M. I. (1985). *Computational Geometry: An Introduction.* Springer-Verlag, New York.

Rahaman, M. F., Naser, J., and Witt, P. J. (2003). An unequal temperature kinetic theory: description of granular flow with multiple particle classes. *Powder Technology*, 138:82–92.

Rahman, K. and Campbell, C. S. (2002). Particle pressures generated around bubbles in gas-fluidized beds. *Journal of Fluid Mechanics*, 455:102–127.

Rapaport, D. C. (2004). *The Art of Molecular Dynamics Simulation.* Cambridge University Press, Cambridge, United Kingdom, second edition.

Rosato, A., Lan, Y., and Wang, D. (1991). Vibratory particle size sorting in multi-component systems. *Powder Technology*, 66:149–160.

Rosato, A., Strandburg, K. J., Prinz, F., and Swendsen, R. H. (1987). Why the Brazil nuts are on top: size segregation of particulate matter by shaking. *Physical Review Letters*, 58(10):1038–1040.

Rosato, A. D., Blackmore, D. L., Zhang, N., and Lan, Y. (2002). A perspective on vibration-induced size segregation of granular materials. *Chemical Engineering Science*, 57:265–275.

Savage, S. B. (1998). Analyses of slow high-concentration flows of granular flows. *Journal of Fluid Mechanics*, 377:1–26.

Savage, S. B. and Jeffrey, D. J. (1981). The stress tensor in a granular flow at high shear rates. *Journal of Fluid Mechanics*, 110:255–272.

Schaeffer, D. G. (1987). Instability in the evolution equations describing incompressible granular flow. *Journal of Differential Equations*, 66:19.

Shen, H. H. and Babic, M. (1999). Rapid flow of granular materials. In Oda, M. and Iwashita, K., editors, *Mechanics of Granular Materials*, volume 1, Chapter 5, pages 319–377. A. A. Balkema.

Shishodia, N. and Wassgren, C. R. (2001). Particle segregation in vibrofluidized beds due to buoyant forces. *Physical Review Letters*, 87(8):084302.

Silbert, L. E., Ertas, D., Grest, G. S., Halsey, T. C., and Levine, D. (2002a). Geometry of frictionless and frictional sphere packings. *Physical Review E*, 65(3):031304.

Silbert, L. E., Ertas, D., Grest, G. S., Halsey, T. C., Levine, D., and Plimpton, S. J. (2001). Granular flow down an inclined plane: Bagnold scaling and rheology. *Physical Review E*, 64(5):051302.

Silbert, L. E., Grest, G. S., and Landry, J. W. (2002b). Statistics of the contact network in frictional and frictionless granular packings. *Physical Review E*, 66(6):061303.

Srivastava, A. and Sundaresan, S. (2003). Analysis of a frictional-kinetic model for gas-particle flow. *Powder Technology*, 129:72–85.

Subramaniam, S. and Pope, S. B. (1998). A mixing model for turbulent reactive flows based on Euclidean minimum spanning trees. *Combustion and Flame*, 115(4):487–514.

Sun, J. and Battaglia, F. (2006). Hydrodynamic modeling of particle rotation for segregation in bubbling gas-fluidized beds. *Chemical Engineering Science*, 61(5):1470–1479.

Sun, J. and Battaglia, F. (2007). Analysis of solid structures and stresses in a gas fluidized bed. In *American Society of Mechanical Engineers, Fluids Engineering Division (Publication) FED*. FEDSM2007-37189. In preparation.

Sun, J., Battaglia, F., and Subramaniam, S. (2006). Dynamics and structures of segregation in a dense, vibrating granular bed. *Physical Review E*, 74(6):061307–13.

Sundaresan, S. (2000). Modeling the hydrodynamics of multiphase flow reactors: Current status and challenges. *AIChE Journal*, 46(6):1102–1105.

Syamlal, M. (1987a). The particle-particle drag term in a multiparticle model of fluidization. Topical report DOE/MC/21353–2373, NTIS/DE87006500, National Energy Technology Laboratory, Department of Energy.

Syamlal, M. (1987b). A review of granular stress constitutive relations. Technical Note DOE/MC21353-2372, NTIS/DE87006499, National Energy Technology Laboratory, Department of Energy.

Syamlal, M. (1994). MFIX documentation: User's manual. Technical Note DOE/METC-95/1013, National Energy Technology Laboratory, Department of Energy. See also URL `http://www.mfix.org`.

Syamlal, M. (1998). MFIX documentation: Numerical technique. Technical Note DOE/MC31346-5824, NTIS/DE98002029, National Energy Technology Laboratory, Department of Energy. See also URL `http://www.mfix.org`.

Syamlal, M. and Gidaspow, D. (1985). Hydrodynamics of fluidization: Prediction of wall to bed heat transfer coefficients. *AIChE Journal*, 31:127.

Syamlal, M. and O'Brien, T. J. (1988). Simulation of granular layer inversion in liquid fluidized bed. *International Journal of Multiphase Flow*, 14:473.

Syamlal, M., Rogers, W., and O'Brien, T. (1993). MFIX documentation: Theory guide. Technical Note DOE/METC-95/1013, NTIS/DE95000031, National Energy Technology Laboratory, Department of Energy. See also URL `http://www.mfix.org`.

Tannehill, J. C., Anderson, D. A., and Pletcher, R. H. (1997). *Computational Fluid Mechanics and Heat Transfer*. Taylor & Francis, Inc., second edition.

Theodosopulu, M. and Dahler, J. S. (1974). The kinetic theory of polyatomic liquids. ii. the rough sphere, rigid ellipsoid, and square-well ellipsoid models. *Journal of Chemical Physics*, 60(10):4048–4057.

Thornton, C. (1999). Discrete element approaches. In Oda, M. and Iwashita, K., editors, *Mechanics of Granular Materials*, volume 1, Chapter 3, page 187. A.A.Balkema.

Truesdell, C. (1984). *Rational Thermodynamics*. Springer-Verlag, New York, second edition.

Trujillo, L., Alam, M., and Herrmann, H. (2003). Segregation in a fluidized binary granular mixture: Competition between buoyancy and geometric forces. *Europhysics Letters*, 64(2):190–196.

Tsuji, Y., Kawaguchi, T., and Tanaka (1993). Discrete particle simulation of two-dimensional fluidized bed. *Powder Technology*, 77:79–87.

Vanel, L. and Clément, E. (1999). Pressure screening and fluctuations at the bottom of a granular column. *The European Physical Journal B*, 11(3):525–533.

Volfson, D., Tsimring, L. S., and Aranson, I. S. (2003a). Order parameter description of stationary partially fluidized shear granular flows. *Physical Review Letters*, 90:254301.

Volfson, D., Tsimring, L. S., and Aranson, I. S. (2003b). Partially fluidized shear granular flows: Continuum theory and molecular dynamics simulations. *Physical Review E*, 68:021301.

Volfson, D., Tsimring, L. S., and Aranson, I. S. (2004). Stick-slip dynamics of a granular layer under shear. *Physical Review E*, 69:031302.

Walton, K. (1987). The effective moduli of a random packing of spheres. *Journal of the Mechanics and Physics of Solids*, 35(3):213–226.

Walton, O. (1992). Numerical simulation of inelastic, frictional particle-particle interactions. In Roco, M., editor, *Particulate Two-phase Flow*, Chapter 25, pages 1249–1253. Butterworth-Heinemann, London.

Wen, C. Y. and Yu, Y. H. (1966). Mechanics of fluidization. In *Fluid particle technology*, volume 62 of *Chemical Engineering Progress Symposium Series*, pages 100–111. American institute of chemical engineers.

Wildman, R. D. and Parkar, D. J. (2002). Coexistence of two granular temperatures in binary vibrofluidized beds. *Physical Review Letters*, 88(19):064301.

Willits, J. and Arnarson, B. (1999). Kinetic theory of a binary mixture of nearly elastic disks. *Physics of Fluids*, 11:3116–3122.

Wu, S. and Baeyens, J. (1998). Segregation by size difference in gas fluidized bed. *Powder Technology*, 98:139–150.

Wu, W., Bauer, E., and Kolymbas, D. (1996). Hypoplastic constitutive model with critical state for granular materials. *Mechanics of Materials*, 23(1):45–69.

Xu, B. H. and Yu, A. B. (1997). Numerical simulation of the gas-solid flow in a fluidized bed by combining discrete particle method with computational fluid dynamics. *Chemical Engineering Science*, 52(16):2785–2809.

Yu, A. B. and Xu, B. H. (2003). Particle-scale modelling of gas-solid flow in fluidisation. *Journal of Chemical Technology & Biotechnology*, 78(2-3):111–121.

Zamankhan, P. (1995). Kinetic theory of multicomponent dense mixtures of slightly inelastic spherical particles. *Physical Review E*, 52(5):4877–4891.

Zhang, D. Z. and Rauenzahn, R. M. (1997). A viscoelastic model for dense granular flows. *Journal of Rheology*, 41(6):1275–1298.

Zhang, D. Z. and Rauenzahn, R. M. (2000). Stress relaxation in dense and slow granular flows. *Journal of Rheology*, 44(5):1019–1041.